SISSA  **ISAS**

SCUOLA INTERNAZIONALE SUPERIORE DI STUDI AVANZATI
INTERNATIONAL SCHOOL FOR ADVANCED STUDIES

I-34014 Trieste ITALY - Via Beirut 4

The effect of dust on the appearance of the spectral energy distribution of galaxies

Thesis submitted for the degree of
Doctor Philosophiæ

CANDIDATE:
Andrew Schurer

SUPERVISOR:
Prof. Gian Luigi Granato
CO-SUPERVISOR:
Dr. Laura Silva
INTERNAL SUPERVISOR:
Prof. Paolo Salucci

October 2009

Dust has become quite trendy ...
everything comes from dust
and everything goes back to dust.
Brian May

Abstract

This thesis will concentrate on the effect that dust grains, within the interstellar medium of galaxies, have, on how we perceive the light emitted from these galaxies and how this effect can be modelled. In particular improvements and extensions made to, and applications made with, a popular spectrophotometric galaxy model, GRASIL, which includes the effects of dust, will be presented. We have interfaced the GRASIL model (Silva et al. 1998) with a detailed chemical evolution model, which also incorporates the evolution of the dust component (Calura et al. 2008), in order to investigate in detail how an evolving dust component affects the spectral energy distribution of different types of galaxies. Usually the chemical composition of dust within the GRASIL code, as well as in other spectrophotometric codes, is fixed to that observed in the Milky Way and the mass of dust calculated using a simple assumption. Consequently by studying the two approaches, we have assessed the importance of accurately following the evolution of dust and the possible errors if this is not done. In a related effort, we have also integrated an artificial neural network into the GRASIL model in order to reduce the computational time required for the code. The model has already been used extensively to calculate the spectral energy distributions of semi-analytical galaxy formation codes, however, the computational time required for GRASIL to calculate the spectral energy distribution, is quite often the bottleneck of the whole operation, limiting the number of mock galaxies that can be processed in realistic applications to $\sim 10^4$. We present first results from this integration of the artificial neural network which should allow, in the near future, an efficient comparison of the spectral energy distribution of semi analytic models, which include a proper dust treatment, to large observational galaxy surveys. Finally we introduce an entirely new photometric galaxy dust model, GRASIL-3D. This model builds on the strengths of the GRASIL model, but allows for any arbitrary geometry for the stars and gas which make up the galaxy. This will allow our new model to be applied to galactic hydrodynamic simulations, which calculate spatially resolved structural and dynamic properties of galaxies, without substantial loss of information. Our code has been integrated with a smooth particle hydrodynamics code, P-DEVA and the method and results are discussed and necessary future improvements are highlighted.

Overview

Within the last decade the effect that dust grains have on stellar light has been receiving increasing interest as telescopes operating in the infrared have proved indisputably the dramatic importance of dust reprocessing, particularly at high redshift. As a result the modelling of this effect has been recognized as an increasingly vital part of astrophysics, both for disentangling information from the spectral energy distribution of galaxies and for the comparison of the prediction of theoretical galaxy formation to observations. This thesis will concentrate on the modelling of this effect, in particular improvements and extensions made to a popular spectrophotometric galaxy model, GRASIL (Silva et al. 1998), which is still widely considered the state of the art in the field.

Chapter 1

In this review chapter the topic of interstellar dust grains will be discussed, and the fundamental theory on which the rest of the thesis is based, will be introduced. Our present knowledge as to the composition of dust grains is presented, in addition to the observational evidence which underpins this. Details are given about the evolution of the dust and the processes which create and destroy the grains, several models which have been constructed to follow these processes in a galactic context are introduced. The effect of this dust grain population on galaxies is briefly discussed as well as several of the codes written to model this process. Finally one particular model, GRASIL, is described in more detail.

Chapter 2

In this chapter a common limitation for all existing dust models, including GRASIL and our new dust model GRASIL-3D, is investigated in detail and overcome. This is the usually overlooked fact that the dust component of the ISM will be constantly evolving and is likely to have different properties at different stages of a galaxies life and will change from galaxy to galaxy. The approach adopted is based on a chemical evolution model of galaxies of three different morphological type which also include the effects of dust evolution (Calura et al. 2008). Hence, the first part of this chapter will describe the details of this chemical-dust evolution model. The next section deals with the integration of this model with the GRASIL code. The results are then presented followed by a discussion of the implication of these results on SED modelling. This chapter is mainly based on a refereed paper Schurer et al. (2009) as well as a conference proceeding: Schurer et al (2008).

Chapter 3

In this chapter, the integration of an artificial neural network into the GRASIL code is described. The motivations for this implementation are discussed as is the method used. The input neurons are of particular importance, and our choices are presented. The

neural network needs to be properly trained in order that it can produce reliable outputs and this process is described. The chapter concludes by presenting some results of this project. The work presented in this chapter allows a good estimate of the dust reprocessed SED of galaxies in CPU times shorter by more than 2 orders of magnitude with respect to a full GRASIL computation. It will provide the basis of a paper, Silva, Schurer et al. (2009), to be submitted soon.

Chapter 4

In this chapter our new SED model, which includes a treatment of radiative transfer through the dusty ISM, GRASIL-3D is introduced. GRASIL-3D has been designed to fully exploit the spatial information hydrodynamical simulations can provide. Our model has been tested by the combination with a particular SPH simulation, consequently the first section of this chapter will introduce this simulation and will discuss how the outputs from the simulation are converted into the necessary inputs for our code. The GRASIL-3D MODEL will then be described in detail, including the technique adopted for the radiative transfer computations. The specific properties of the galaxy used as a test object will be given and the values of the free parameters chosen to model this galaxy and the reason for these choices will be discussed. The results given for this object by our model are then presented. The chapter concludes with a discussion of the results and further improvements needed for the model. Additional computational details for the model are given in Appendix A. This chapter will form the basis for a paper, Schurer et al (2009), in prep.

Table of Contents

Title Page i
Abstract iii
Overview iv
Table of Contents vi

1 The dusty interstellar medium **1**
1.1 Composition of Dust 3
1.1.1 Dust grains in meteorites 3
1.1.2 Extinction Curve 4
1.1.3 Emission spectrum 7
1.1.4 Interstellar gas depletions 9
1.1.5 Dust grain models 9
1.2 The dust cycle 12
1.3 Effects of dust on the observed spectral energy distribution of galaxies and its implications 15
1.4 Modelling the effect of dust on the SED of galaxies 17
1.5 An existing dust model - GRASIL 21
1.5.1 Stellar Population Model 22
1.5.2 Dust Model 22

2 Modelling the effects of dust evolution on the SEDs of galaxies **26**
2.1 Introduction 27
2.2 Chemical evolution models 29
2.2.1 Gas Evolution 29
2.2.2 Dust Evolution 34
2.3 Interfacing with the GRASIL dust model 37
2.3.1 Choice of parameters 37
2.3.2 Generating SEDs 41
2.3.3 Treatment of PAH molecules 42
2.3.4 Comparison to Observations 44
2.4 Results 45
2.4.1 Properties of Spiral Galaxies 45
2.4.2 Properties of Irregular Galaxies 52
2.4.3 Properties of Elliptical Galaxies 60
2.5 Implications of this Work 77

2.6 Summary 81

3 Modelling SEDs with Artificial Neural Networks 84
3.1 Introduction 84
3.2 Artificial Neural Networks 87
3.2.1 Basic concepts 87
3.2.2 Feed-forward multi-layer back-propagation ANN 89
3.3 Implementing ANN in GRASIL 93
3.3.1 Input and output neurons 94
3.4 Applications 97
3.4.1 Trained net 97
3.4.2 Examples with single SEDs 100
3.4.3 Statical samples 103
3.4.4 Computing performance 105
3.5 Summary 106

4 A galaxy dust model for hydrodynamical galaxy simulations 107
4.1 Introduction 107
4.2 The SPH galaxy formation code 109
4.3 Implementation of dust effects 110
4.3.1 Charging the grid 111
4.3.2 Dust Composition and properties 114
4.3.3 Radiation transfer in molecular clouds and emerging spectrum . . . 118
4.3.4 Radiation transfer through the diffuse cirrus 119
4.3.5 Free parameters of the model 120
4.4 Testing the models with a galaxy generated by P-DEVA 122
4.4.1 Object Properties 122
4.4.2 Choice for free parameters 123
4.4.3 Results 126
4.5 Discussion and future work 132
4.5.1 Improvements needed for the model 132
4.5.2 Testing 136
4.5.3 Properties of the model 138
4.6 Summary 140

5 Concluding Remarks 142
5.1 Summary of Results 142
5.2 Future Work 144

Bibliography 148

A Computation Details for GRASIL-3D 158
A.1 The SPH grid charging technique 158
A.2 Calculating f_{mc} 159
A.3 Calculating $P(T)$ the temperature distribution for small grains 161

A.4 Calculating $r(i,k)$ for nearest neighbours 163
A.5 Details of optimisations and computing time 166

Chapter 1

The dusty interstellar medium

The presence of an interstellar medium (ISM) absorbing and scattering the light from stellar objects has been known for many years, the discovery of which is widely attributed to Trumpler (1930). In this remarkable paper Trumpler, through a study of open clusters in the Galaxy, found that photometric distances were systematically larger than would be expected if the light was only dimmed by an inverse square law (see fig. 1.1). This suggested that there was some form of medium between the observed stars and the observers. Colour excesses observed in local clusters also suggested that the amount of absorption could be dependent on wavelength, leading to the conclusion that "fine cosmic dust particles of various size" were present "producing the observed selective absorption". The author then goes on to make tentative predictions about the composition of this dust. Nearly eighty years later, and after much study, plenty has been learned about Trumpler's mystery dust particles, although many things, including even their composition, remains highly uncertain.

Since their discovery, it has become increasingly clear that dust is abundant in the ISM of the majority of galaxies and plays a very important role in astrophysics. Firstly, dust changes the way we view stars and galaxies, absorbing light in the ultra violet (UV) and optical and then emitting the light in the infra-red (IR). Historically the attenuation of the light has received the most attention but with the development of sensitive telescopes operating in the IR and sub-mm, including the recently launched Herschel Space Observa-

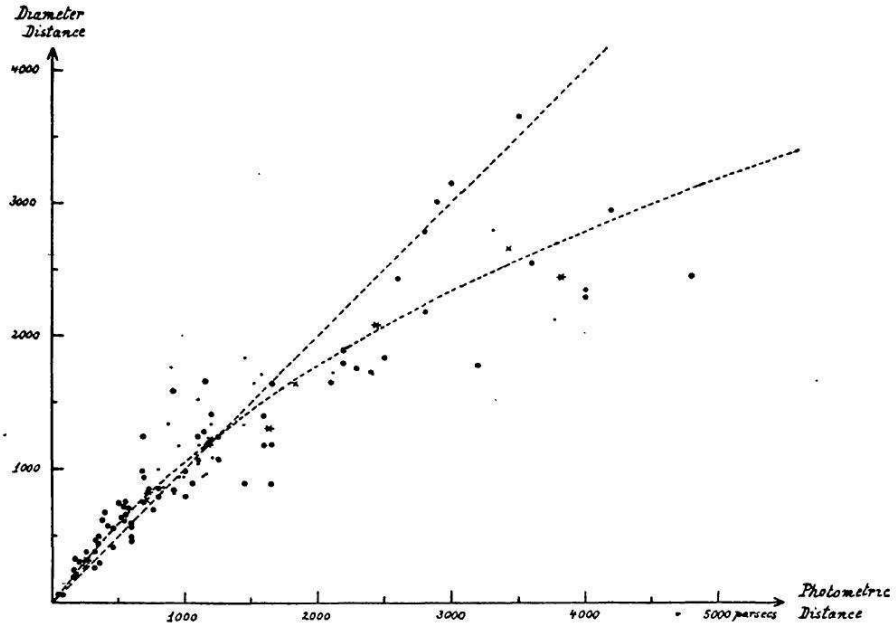

Figure 1.1: Comparison of the distances of 100 open star clusters determined from apparent magnitudes and spectral types with those determined from angular diameters. The large dots refer to clusters with well-determined photometric distances, the small dots to clusters with less certain data. The asterisks and crosses represent group means. If no general space absorption were present, the clusters should fall along the dotted line; the dotted curve gives the relation between the two distances measures for a general absorption of 0.7m per 1000 parsecs. Taken from Trumpler (1930).

tory, the study of the emission spectrum is becoming increasingly important, both as an indicator of the physical conditions of star formation and as a window to previously unobserved heavily obscured star populations. Indeed it has been found that approximately 30 per cent of all light radiated by stars in the local universe has been dust reprocessed (Soifer & Neugebauer 1991) and measurements of the far infra-red (FIR) /sub-mm background estimate a potentially larger percentage $\sim$ 50 per cent reprocessed over the entire history of the universe (see e.g. Hauser & Dwek 2001 for a review). Additionally dust is now understood to have a fundamental role in galaxy evolution, strongly influencing the physical and chemical conditions of the interstellar medium: determining the way in which stars form and providing the basis for planet formation. Its overwhelming importance in both these areas has been proved beyond doubt, although the contents of this particular thesis

will be limited only to the former of these two topics, the effect on the multi-wavelength appearance of galaxies.

This section of the thesis will aim to introduce some of the fundamental theory about dust grains and how they affect how we observe galaxies, particularly concentrating on concepts which are important to the work discussed in the later chapters. § 1.1 will briefly describe our current view of what dust grains are composed of and what their size distribution is. § 1.2 explains the various processes in which dust grains are produced and the competing processes which lead to the destruction of dust grains as well as introducing several important studies into modelling this evolution . The effect of these dust grains, particularly on galaxies, and the wider implications of these effects on astrophysics is discussed in § 1.3. How these effects have been modelled is explained in § 1.4 and several different models are introduced. One of these models, which will have special relevance for this thesis is described in more detail in § 1.5.

1.1 Composition of Dust

1.1.1 Dust grains in meteorites

Perhaps the most obvious method for the determination of the composition of dust grains is by directly capturing them from within the solar system. This has been possible, thanks to the presence of genuine interstellar grains within meteorites (see Clayton & Nittler 2004 for a review). Dust grains can be identified in meteorites by isotropic anomalies and then their chemistry can be studied in laboratories here on earth. Unfortunately not all possible dust grains can be identified using this technique, since only certain dust grains display these anomalies, (those formed in stellar outflows and in supernovae ejecta). As a result dust grains identified in meteorites are unrepresentative of the overall composition and therefore only limited conclusions can be made as to the overall composition of dust grains from laboratory studies. Instead, we are forced to also rely on remote sensing, with the majority of our knowledge of interstellar dust largely derived from the interaction of dust particles with electromagnetic radiation.

1.1.2 Extinction Curve

The extinction of light refers to the combined effect of the scattering and absorption of light by dust grains, located between the observer and an object. It is also often referred to as "reddening", since the extinction of the light is wavelength dependent, with the strongest effect at smallest wavelengths. A related term which is also used, is the "attenuation" of light. This term is often used, incorrectly, to mean the same thing as extinction. This confusion is because *attenuation* also refers to the reddening of interstellar light. Attenuation should however be used when referring to the observed reddening in complex systems, for example whole galaxies, where the relative geometry of the dust and stars, as well as the composition of the dust grains, governs the observed reddening. An example to illustrate the difference between the two terms is to consider any normal star-forming galaxy. If you could resolve the galaxy into individual stars the reddening observed in the spectra of any single star can be termed *extinction*, where the difference in the intrinsic spectra of the star and the observed spectra, its extinction curve, can be modelled by a slab of dust of appropriate composition and density placed between the star and the observer. When the galaxy as a whole is observed, however, the term *attenuation* should be used. This is because the stars will be located in different environments, so the light from some stars will undergo more extinction than the light from others. As a result the difference between the intrinsic light of the whole galaxy and the observed light will be much more complex than the simpler case of extinction. Modelling the reddening, in this case as a simple slab, is no longer adequate.

By studying the wavelength dependence of interstellar extinction much can be learnt about both the size and composition of dust grains. Extinction curves are most commonly determined by use of the "pair method" - a comparison of the fluxes from two stars with nearly-identical spectroscopic features but with one of the stars nearly unaffected by dust. By assuming that the extinction goes to zero at large wavelengths it is possible to normalise the flux from the two stars with each other and to determine how the extinction A_λ varies with wavelength (the extinction curve).

The *amount* of extinction is clearly proportional to the mass and density of dust

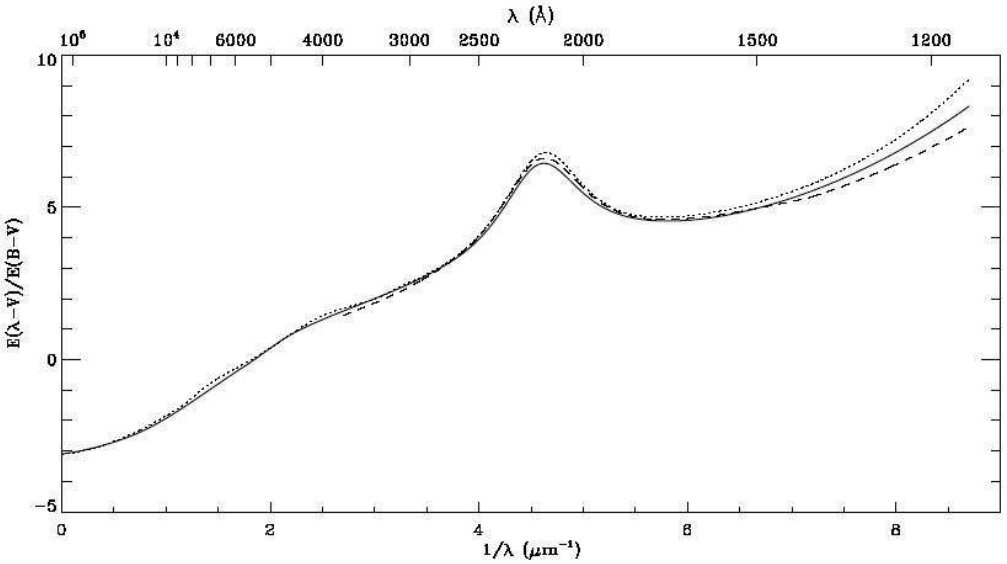

Figure 1.2: Normalized interstellar extinction curves from the far-IR through the UV. The solid and dotted curves are estimates for the case R = A(V)/E(B-V) = 3.1 by Fitzpatrick 1999 and by Cardelli, Clayton, & Mathis 1989, respectively. The dashed curve shows the average Galactic UV extinction curve from Seaton 1979. Taken from Fitzpatrick (1999).

between the star and the observer. The *shape* of the extinction curve however is dependent on the size and composition of the dust grains and can therefore be used to study the properties of the interstellar dust. A typical extinction curve is shown in figure 1.2. Observed extinction curves have been found to vary from one sightline to another so it is clear that the properties of dust must be different at different locations. The curves do however appear to approximately form an one-parameter family (Cardelli et al. 1989) and all share common characteristics.

The most obvious feature of the extinction curve is the slope itself. The extinction is clearly wavelength dependent with the extinction increasing as the wavelength decreases. This shows that many of the dust grains must be small, since if the grains were large compared to the wavelength, we would be in the "geometric optics" limit, where the extinction cross-section would be independent of the wavelength.

From figure 1.2 it is clear that there is at least one prominent extinction feature, which can used to help determine the composition of the dust, the large feature at λ^{-1}

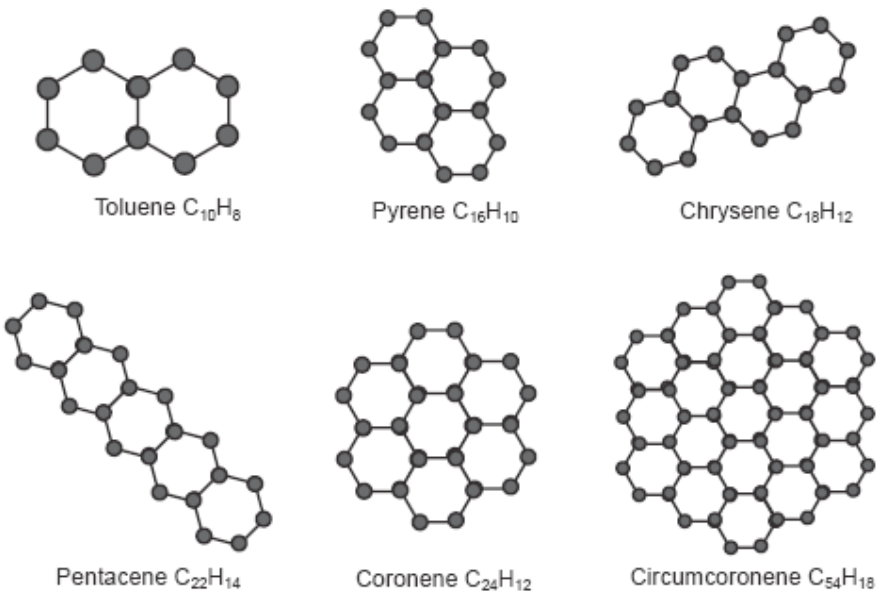

Figure 1.3: Shows the molecular layout of several common PAH molecules.

$= 4.6\mu m^{-1}$, or $\lambda = 2175\mathring{A}$. Since small graphite grains have a strong absorption at this frequency, due to $\pi \rightarrow \pi^*$ electronic excitations in the sp^2-bonded carbon sheets, this feature is used as evidence for either a large proportion of small graphite grains or poly aromatic hydrocarbon (PAH) molecules which have a similar atomic structure (see figure 1.3).

Smaller extinction features, not shown in figure 1.2 also exist at 9.7 μm and 18 μm. Which have been attributed to a stretching mode of Si-O and a bending mode of Si-O-Si, leading to the conclusion that at least some of the interstellar dust will be in the form of amorphous silicates. A broad absorption feature is also observed at 3.4 μm which has been attributed to a stretching mode of C-H. There are also many additional weaker features known as the diffuse interstellar bands. Although they were discovered over 80 years ago (Heger 1922 and Merrill 1934), the responsible molecules have not been identified.

The polarization of starlight was first discovered in 1949 (Hall 1949; Hiltner 1949). The polarization was found to be larger for stars with greater reddening and that light from similar regions of the sky had similar polarization directions. This strongly suggested that the polarization was due to the ISM. This has been explained by preferential extinction by

dust grains of one polarization mode relative to another, suggesting that there must be non-spherical and magnetically aligned dust component in the ISM. The degree of polarization observed at different wavelengths can be used to infer properties of the dust grains and should be reproduced by any dust model.

1.1.3 Emission spectrum

The energy which is absorbed by the interstellar dust is then reradiated at longer wavelengths, in the infrared. The emission spectrum of the Galaxy can be estimated from all-sky surveys by the IRAS and COBE satellites. From a correlation between infrared surface brightness and the hydrogen 21cm emission line it is possible to extract the infrared emission per H atom (see figure 1.4). Any proposed dust model has to be able to recreate this observed emission.

Also clearly evident in the emission spectra shown in figure 1.4 are several emission features in the mid-infrared with wavelengths between 3 and 13μm. These features are fairly ubiquitous throughout our Galaxy and have been observed in planetary nebulae, HII regions, photo-dissociation fronts and reflection nebulae. Our knowledge of the observed mid-infrared spectra of interstellar objects has been greatly increased during recent times, first due to the spectroscopic observations with the *Infrared Space Observatory* (*ISO*) and, within the last few years, due to the unprecedented sensitivity by the *Spitzer Space Telescope*. The energy re-reradiated just into these bands is quite strong, with the fraction often as large as 20 per cent. The particles responsible for this emission are therefore likely to be quite abundant.

It is now widely acknowledged that these particles are PAHs. These molecules can be thought of as sheets of graphite (see figure 1.3). The various bands are attributed to various bending and stretching modes within the PAH molecules. Although the precise position and the relative strength of the bands vary from one individual PAH to another, and vary also upon the state of ionization, it has been shown that mixtures of PAHs both neutral and ionized can produce combined spectra in good agreement with recent observations (e.g. Draine & Li 2007).

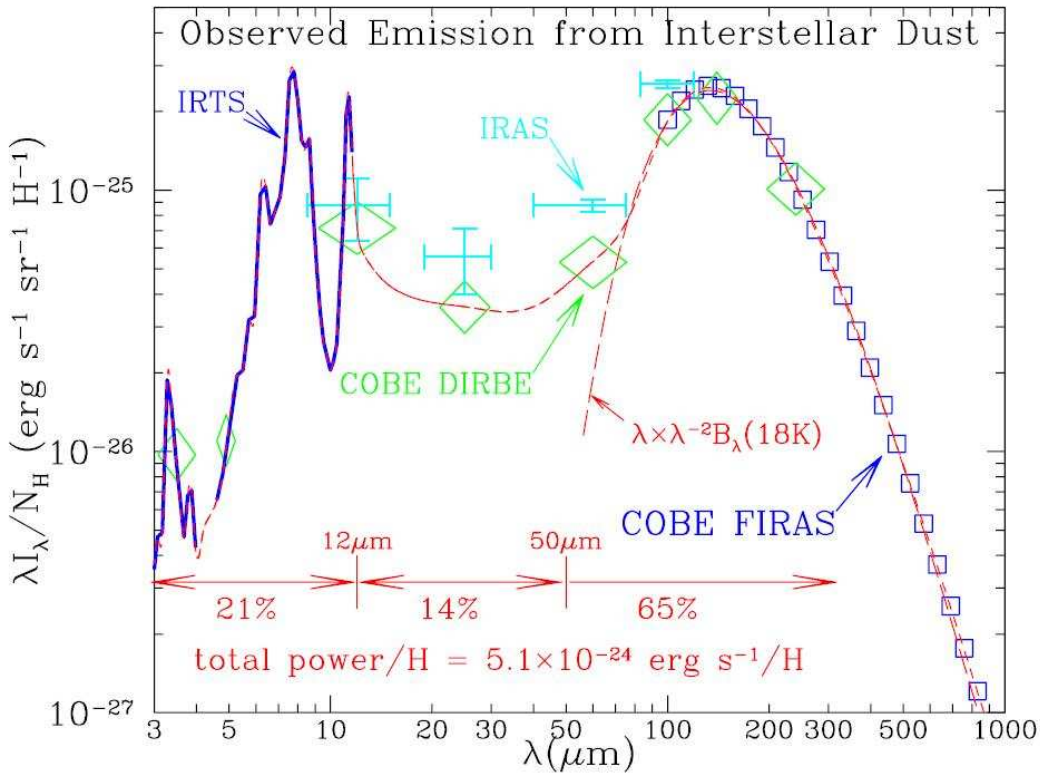

Figure 1.4: Shows the emission spectrum of diffuse interstellar dust in the Milky Way. Crosses: IRAS (Boulanger & Perault 1988); squares: COBE-FIRAS (Finkbeiner et al. 1999); diamonds: COBE-DIRBE (Arendt et al. 1998); heavy curve for 3-4.5 μ m and 5 - 11.5 μ m: IRTS (Onaka et al. 1996, Tanaka et al. 1996). The total power $\sim 5.110^{-24}$ $ergss^{-1}/H$ is estimated from the interpolated broken line. Taken from Draine (2004)

1.1.4 Interstellar gas depletions

The final major piece of evidence which can be used to determine the composition of the dust, is the chemistry of the gas within the ISM. By analysing narrow absorption lines in the optical and UV regions of the stellar spectra the interstellar gas phase abundance of many elements can be calculated. One could assume that the interstellar gas abundances should be approximately equal to solar abundances, and this is indeed the case for several elements, such as N and S. However for others the abundances observed in the gas are significantly lower than solar, with the obvious explanation that the missing elements are locked up in dust grains. The difference between the abundances observed in the interstellar gas and the solar abundance should therefore give a strong clue of the chemical composition of the dust (see figure 1.5). Due to uncertainties in the choice of a representative set of ISM abundances, this is still only a weak constraint.

1.1.5 Dust grain models

To construct a viable dust model, which specifies the chemical composition and size distribution of the dust grains, it is necessary to satisfy all the observational constraints, the most important of which have already been mentioned in this section, namely the extinction curve, the emission spectra and the interstellar depletion abundances. Several models have been proposed by a variety of different authors. These fall broadly in to three different groups:

- the bare silicate-graphite model (Mathis et al. 1977; Draine & Lee 1984; Kim et al. 1994) and its natural extension: the silicate graphite PAH model (Siebenmorgen & Krugel 1992; Silva et al 1998, Li & Draine 2001, Weingartner & Draine 2001a, Draine & Li 2007).

- the silicate core carbonaceous mantle model (Desert et al. 1990; Jones et al. 1990; Li & Greenberg 1997)

- the composite model, which assumes the dust to be low-density aggregates of small silicate and carbonaceous particles (Mathis & Whiffen 1989; Mathis 1996; Zubko et

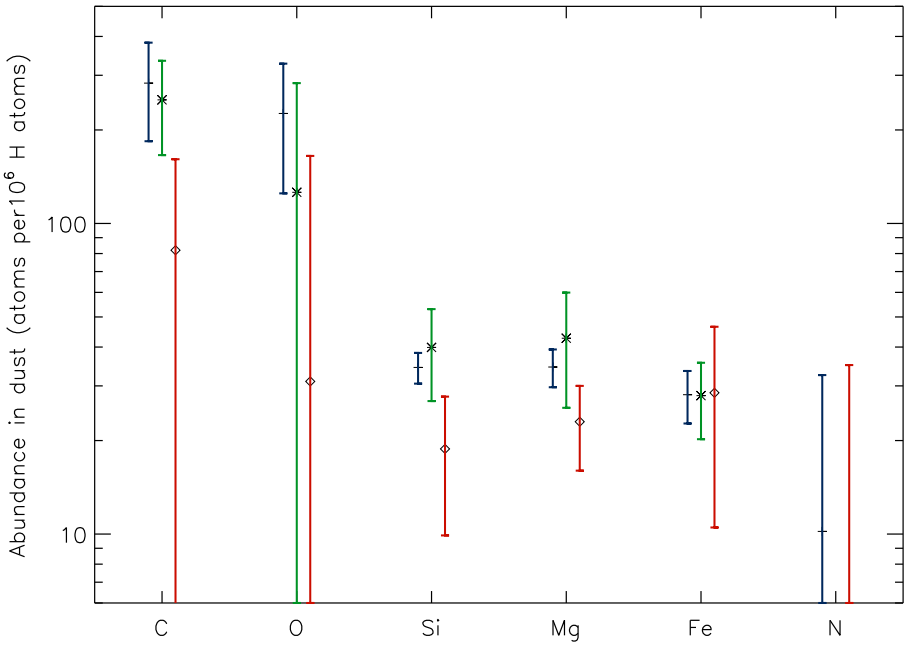

Figure 1.5: Shows the elemental abundances for dust derived by Zubko et al (2004) using three different measurements for the total interstellar abundances based on: blue - solar abundance (Holweger 2001); green - F and G star abundances ((Snow & Witt 1996; Sofia & Meyer 2001); red - B star abundances (Sofia & Meyer 2001).

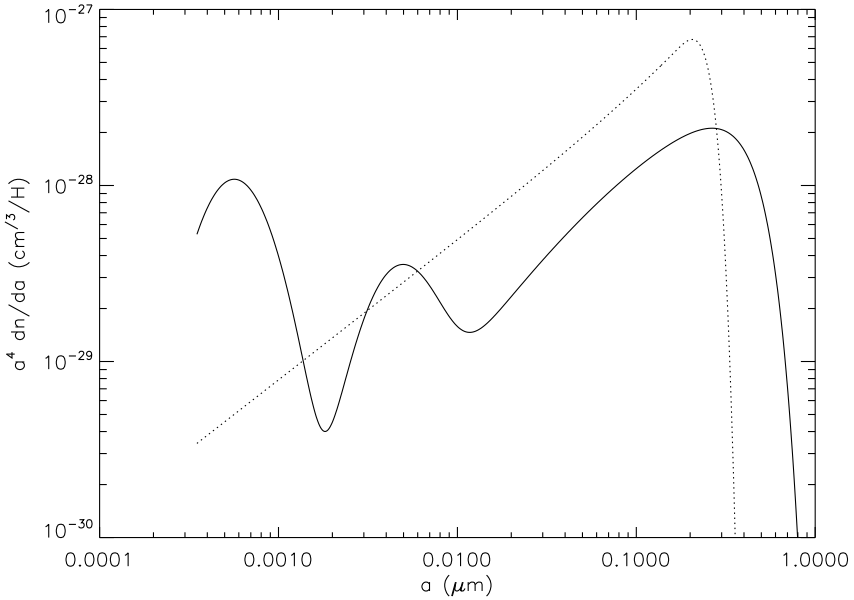

Figure 1.6: Size distribution proposed by Weingartner & Draine (2001)a for dust consistent with an $R_v = 3.1$ extinction curve for the Milky Way. Solid line - the size distribution of carbon grains. Dotted line - the size distribution of silicate grains.

al. 2004).

Of these models the core-mantle model has been recently challenged by the non detection of polarization in the 3.4μ m C-H aliphatic hydrocarbon feature on sight lines where the 9.7 Si-O-Si band is observed to be polarized (Chiar et al. 2006; Mason et al. 2007; see also Adamson et al. 1999; Li & Greenberg 2002).

The latest versions of dust models belonging to the other two groups all remain viable. The Draine & Li (2007) model, which is a continuation of early models (Li & Draine 2001b, Weingartner & Draine 2001a,) has been highly successful at explaining a large quantity of separate pieces of evidence, and includes a recent update to the optical properties of the PAH molecules, in order to agree with the latest spitzer space telescope observations. The size distribution proposed by this model is shown in figure 1.6. The latest version of the composite model put forward by Zubko et al. (2004) also successfully reproduces the observed interstellar extinction and IR emission. The models proposed

in this paper, including bare silicate-carbonaceous models, are also specifically tuned to agree with the interstellar gas depletion abundances and it is argued that these models are therefore more consistent with observations than the "Draine" models, which they claimed require too much Mg, Si and Fe. This comment has been refuted by Li (2005) based on the Kramers-Kronig relation who argued that Photospheric stellar abundances could not be used as a reliable indicator of interstellar abundances for the elements that form refractory grains, such as Mg, Si, and Fe, since partial separation of dust and gas by processes such as radiation pressure, ambipolar diffusion, and gravitational sedimentation in the process of star formation could result in the observed stellar abundances differing from the actual interstellar abundances.

1.2 The dust cycle

The interstellar dust grain population is formed due to a complicated mix of processes leading to both the creation and growth of dust grains as well as competing destruction processes. It is hoped that, by studying the various processes involved, it should be possible to build up a detailed picture of the rates of the different processes and how and where they contribute to the evolution of the size-distribution and composition of the dust grain population. In such a way it should be possible to predict how the dust population of a galaxy evolves and how it varies from region to region. Unfortunately we are still some distance from such a comprehensive model, due to the complexity of the situation.

Dust production by stars

There is abundant observational evidence that dust grains form in stellar outflows, particularly from AGB and Wolf-Rayet stars and in the explosively expelled ejecta of SNe and novae, mainly in the form of observed infrared and sub-mm emission from dust around these objects.

For AGB stars, the yield and composition of the dust is believed to be dependent on the atmosphere of the stars during this stage in the stars life, particular the C/O ratio. For oxygen rich stars, the $9.7\mu m$ absorption feature has been detected (e.g. Demyk et al

2000), which indicates the presence of silicate dust (as well as other silicate absorption and emission features). Whereas around carbon rich stars a similar $9.7\mu m$ feature has not been observed (e.g. Blanco et al. 1998), suggesting an absence of silicate dust grains. Theoretical models have been used to calculate the dust yield of AGB stars, with the composition usually dependent on the C/O ratio (e.g. Ferrarotti & Gail 2006).

Recent FIR to sub-mm observations of quasars have revealed large masses of dust at high redshift (Bertoldi et al. 2003; Robson et al. 2004; Beelen et al. 2006). The presence of such quantities of dust when the universe was less than 1 Gyr old, before significant dust production from giant stars was possible, suggests an important role should be played by the enrichment due to supernovae (SNe) (Morgan & Edmunds 2003; Maiolino et al. 2004, Dwek et al. 2007). Theoretical models support this, predicting that each Type II SNe should produce ~ 0.1 - 1 $M_{\odot}$ of dust (Todini & Ferrara 2001; Nozawa et al. 2003; Bianchi & Schneider 2007). Observation of dust in the remnants of SNe remain controversial, with many observations in the infrared (e.g. Sugerman et al. 2006 and Rho et al. 2008) finding masses of dust orders of magnitude less than that predicted by theory. However competing observations in the sub-mm have detected considerable dust (Dunne et al., 2003, 2008, Morgan et al. 2003 but see also Krase et al 2004, Wilson & Batrla 2005).

ISM processes affecting the grains

Once injected into the ISM the grains are subjected to a variety of interstellar processes, including thermal sputtering in high velocity shocks and evaporation and shattering by grain-grain collisions in lower velocity shocks. The dominant processes are thought to be those induced by SNe. Detailed descriptions of all the destruction effects are given in Jones et al (1996).

By analysing the timescales of the competing processes it is possible to estimate the lifetimes of the typical dust grain. Jones et al (1996) found that the timescales for the destruction processes were far shorter than the timescales for replenishment by stars (~ 0.5 $Gyrs$ and 2 $Gyrs$ respectively). Since there is an observably large dust population in many galaxies this implied that there must be another process responsible for the build up of the dust grains; accretion in dense molecular clouds. Direct evidence for dust accretion is

provided by the observed large variations of the depletion levels as a function of the density (Savage & Sembach 1996) and from the observed infrared emission of cold molecular clouds (Flagey et al. 2006), which is characterised by the absence of small-grain emission. Using the timescale arguments, it can be inferred that the dust growth by accretion in molecular clouds is likely to be an important process. It has also been suggested that rapid growth in molecular clouds could explain the majority of the mass of dust at high redshift (see e.g. Draine 2009) as an alternative explanation to the production of large masses of dust by SNe.

Dust Evolution Models

The challenge facing a dust evolution model is therefore to combine all of these processes in one model and use it to recreate several observations, particularly the dust depletion levels observed in the local universe (see figure § 1.5). In order to model the various competing processes, it is necessary to incorporate them into existing chemical evolution codes, which follow both the chemistry of the stars and the gas. This is because the processes governing the dust population are heavily interlinked with the chemistry of the galaxy as a whole.

The first full galaxy model of a sufficient complexity to model the composition and evolution of the interstellar dust mixture was the model of Dwek (1998). This model incorporated simple treatments of all the processes described above into a chemical evolution model of the galactic disc. The results obtained by this model were sufficiently good to show that such an approach can be used to successfully model the evolution of the cosmic dust. Several authors, starting from the framework first proposed by Dwek, have constructed dust evolution models of their own, with improved treatments for the dust processes following recent observations. Examples include: Calura et al. (2008) (hereafter CPM08), who have updated the dust production and destruction efficiencies and have also extended the treatment to different environments (an irregular and elliptical galaxy), more details of this model are given in § 3.1.2; and Zhukovska, Gail & Trieloff (2007) who have implemented an improved treatment of accretion in molecular clouds and have used their model to study the differential evolution between dust grown in molecular clouds and dust from stellar sources.

1.3 Effects of dust on the observed spectral energy distribution of galaxies and its implications

Figure 1.7 shows the spectral energy distributions (SEDs) of four normal galaxies of different types, found in the local universe: a spiral, an irregular, an elliptical and a starburst galaxy. The SED of a galaxy contains a wealth of information about its stellar and gas content; the ages and chemistry of the stellar populations, the star formation rate and history, in addition to information about the physical state of the ISM. As such, it is probably the most direct and important probe of a galaxy's properties. Extracting such information is however far from straightforward.

One of the greatest challenges to disentangling the information available in the SED is dust-reprocessing. As previously mentioned this is the process whereby the stellar emission is absorbed in the UV-optical and re-emitted in the IR. This process is clearly illustrated in figure 1.7, which shows both the SED of the bare-starlight if dust-reprocessing was ignored and the SED of the actual galaxy after the starlight has traveled through the dusty ISM. It can be seen that the effect of the dust is more important in some galaxies than in others. Of the galaxies shown in figure 1.7 for example the percentage of the total light reprocessed by dust is approximately 27 per cent in the spiral galaxy, 12 per cent in the irregular galaxy, 1 per cent in the elliptical galaxy and 80 per cent in the starburst galaxy. This percentage of dust reprocessing is dependent on not only the mass of dust present but also the star formation rate, since stars are born inside dense clouds of gas and dust where the extinction is likely to be high. Just from these graphs it is possible to appreciate the dangers of ignoring dust, especially in surveys just in the UV and optical bands. While such an assumption may lead to acceptable properties being derived for galaxy c, the vast majority of the galaxy's mass and star-formation would be missed if dust was ignored in galaxy d.

A very important historical example of this effect occurred around 15 year ago. At that time studies of high redshift galaxies relied on optical surveys. Consequently, it was not possible to properly estimate the effects of dust. Since the mass of gas and dust was believed to lower in the high redshift universe, it was common to ignore its effect in

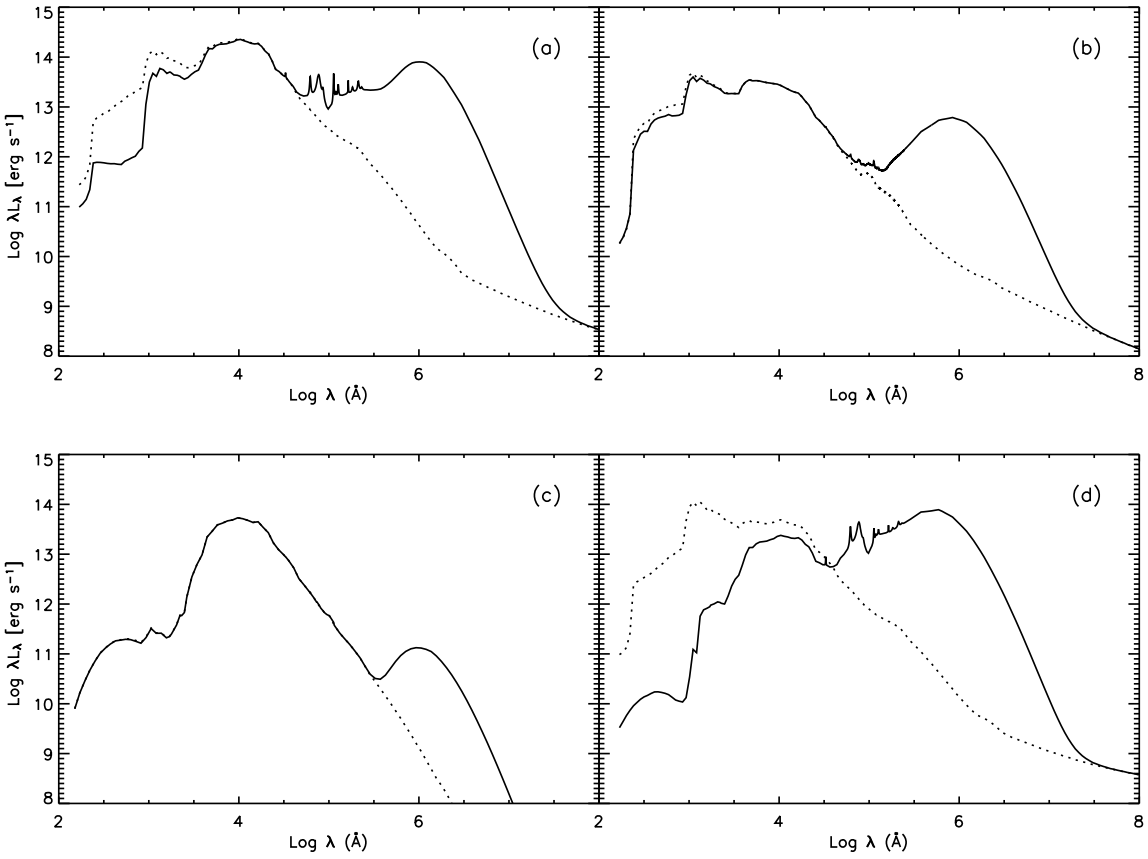

Figure 1.7: Graph showing the effect of dust on the SED of local galaxies. The plots show the SED after dust reprocessing (the solid line) and the intrinsic SED (the dashed line) for (a) a spiral galaxy (M100 from Silva et al 98) (b) a standard irregular galaxy (from Schurer et al 08), (c) a standard elliptical galaxy (from Silva et al 98), and (d) a starburst galaxy (M81 from Silva et al 98)).

studies of the cosmic star formation history (e.g. Madau et al. 1996 see figure 1.8a), and the commonly held view was that the co-moving star-formation rate peaked at $z \sim 1$ and then declined. Subsequent observation of many highly extincted objects (e.g. SCUBA sources, lyman-alpha detected sources, Extremely Red Objects (EROs), Lyman-break galaxies) at high redshift, which all show large levels of dust reprocessing (see e.g. a review by Meurer (2004) and references there-in) in addition to the detection of a large cosmic FIR-sub-mm background by COBE (see e.g. Hauser & Dwek 2001 for a review), indicated the important role that dust reprocessing has at higher redshifts. This discovery had a profound effect on theories of galaxy formation since the newly calculated cosmic star formation history changed to the one displayed in figure 1.8b, taken from Hopkins et al (2004), which shows that the star formation rate is in fact flat for $z > 1$. This presented a serious challenge to the prevailing galaxy formation theories which predominantly conformed to the star formation history of the universe shown in figure 1.8a (see Granato et al 2000), forcing them to adopt several new concepts. It has also led to the idea of "cosmic downsizing", for a comprehensive review see Renzini (2006). The difference between the two graphs clearly illustrates the perils of ignoring dust when analysing observations. Likewise, it is also of vital importance when trying to recreate these observations using theoretical galaxy formation models, to correctly model the dust emission.

Hence, it is now widely accepted that a proper treatment of the dust reprocessing in galaxies is essential, both to derive physical quantities such as star-formation rates and star-formation histories from observations, and also when testing theoretical galaxy formation models against observations.

1.4 Modelling the effect of dust on the SED of galaxies

We have seen from the previous section the importance of a proper treatment for the dust component when dealing with the optical appearance of galaxies. Several different approaches have been used to handle the complexities of the problem, and many different galactic dust models have been proposed to follow the propagation of photons through the ISM (see reviews by Dopita 2005 for starbursts, Popescu & Tuffs 2005 for normal galaxies

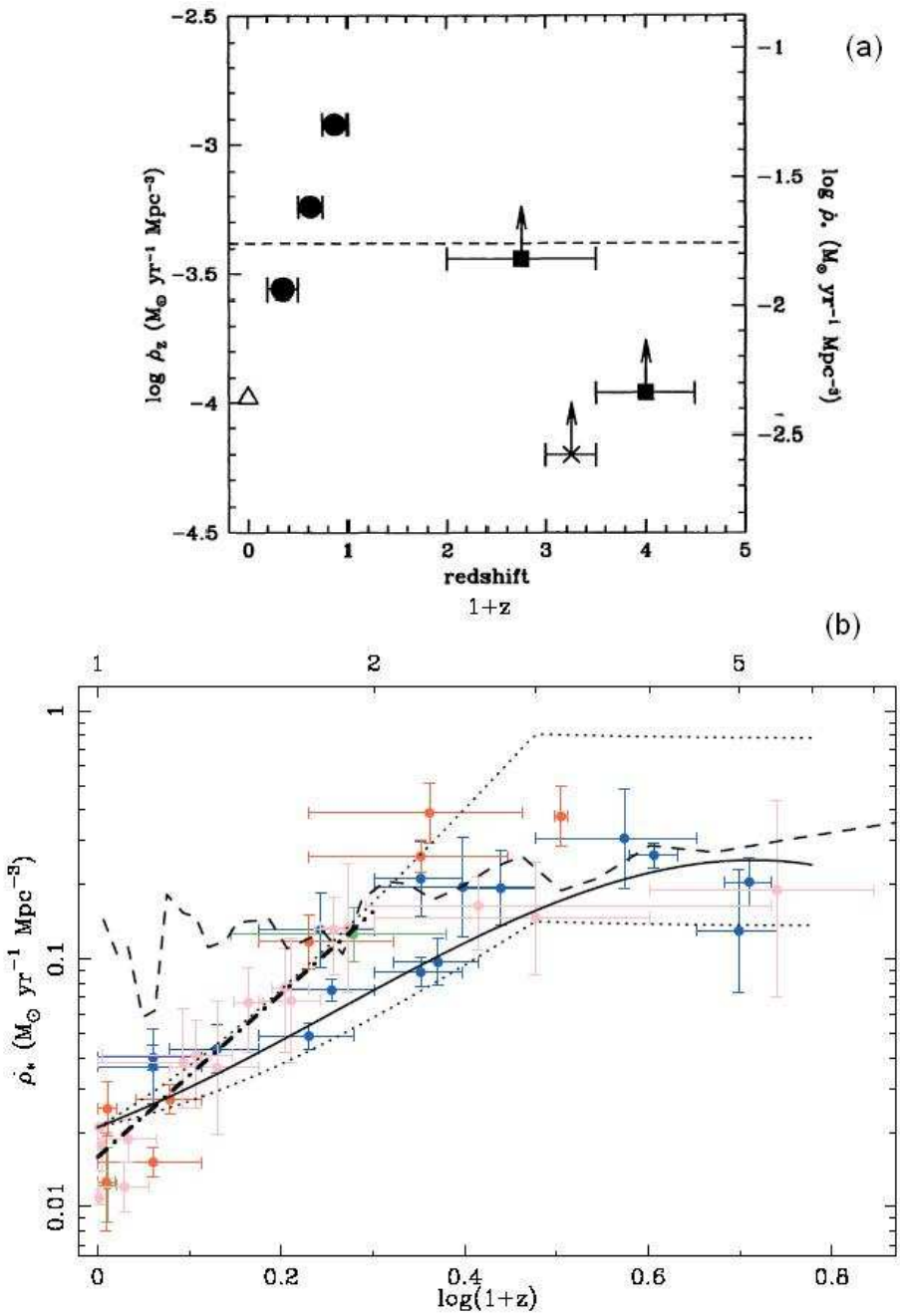

Figure 1.8: Evolution of SFR density with redshift. a) taken from Madau et al. (1996). Triangles: Gallego et al. (1995), Filled dots: Lilly et al (1996), Cross: Steidel et al. (1996), Filled square: lower limits from HDF. b) taken from Hopkins et al. (2004). The points are color-coded by rest-frame wavelength as follows: Blue: UV; green: [O ii]; red: Hα and H1β; pink: X-ray, FIR, submillimeter, and radio. Note: the difference in absolute values between the two plots is due to the different cosmological parameters used.

and Madden 2005 for irregular galaxies). Such galactic dust models treat this component with differing geometries and with varying degrees of sophistication.

Many works rely on semi-empirical treatments of the SEDs, particularly in IR spectral range (e.g. Devriendt, Guiderdoni, & Sadat 1999, Chary & Elbaz 2001; Dale & Helou 2002; Lagache, Dole & Puget 2003; da Cunha, Charlot & Elbaz 2008). The goal of such an approach is generally the interpretation of large samples of data, matching reference SEDs, which are often physically motivated to observations, in order to derive the galaxy properties.

Other codes perform more complex radiative transfer calculations through the dusty ISM of composition given by a specific dust mixture (see § 1.1.5), constructing models with various degrees of sophistication and specialisation. The majority of the codes have been designed to be applied to a particular type of galaxy. The number of models written is large so only a small selection will be mentioned here.

Starburst Galaxies

These models are designed to model the SEDs of large star-forming galaxies and therefore usually concentrate on the areas of star-formation themselves, often including sophisticated modelling of the radiative transfer through molecular clouds, where the stars are born. Some also include a treatment for the radiative transfer through the diffuse cirrus surrounding the molecular clouds, however this is normally quite approximate. Examples include: Rowan-Robinson & Crawford (1989); Krugel & Siebenmorgen (1994); Efstathiou, Rowan-Robinson & Siebenmorgen (2000); Takagi, Arimoto & Hanami (2003) and Siebenmorgen & Krugel (2007). As well as a series of papers by Dopita et al. (2005, 2006a,b) and Groves et al (2008).

High redshift - sub-mm Galaxies

It is becoming increasingly clear that sub-mm detected galaxies at high redshift, although sharing several characteristics of local starbursts, display distinct differences, for example showing higher specific star formation rates (star formation rate / stellar mass) (Bauer et al. 2005), and have higher dust obscuration rates (Hammer et al. 2005). The

SED modelling of these galaxies, therefore, presents a different challenge to that of the starburst galaxy and several models have been written to achieve this (e.g. Efstathiou & Rowan-Robinson 2003 and Efstathiou & Siebenmorgen 2009).

Spiral Galaxies

Several dust models have been constructed to model and interpret the SEDs of local spiral galaxies and, in particular, to place constraints on the optical thickness of discs, the attenuation curve and scale lengths for the stars and dust. Examples include the work of Kylafis & Bahcall (1987), Byun et al. (1994), Witt et al. (1992), Bianchi et al (1996), a series of papers by Xilouris et al. (1997, 1998 and 1999) and a series of papers by Popescu et al (2000), Misiriotis et al (2001), Tuffs et al (2004), Möllenhoff, Popescu & Tuffs (2006). Because star formation is less intense in these galaxies, it means dust reprocessing by the diffuse cirrus component becomes relatively more important. Hence, it is the radiative transfer through the cirrus component which is usually the most sophisticated part of these codes. In order to reproduce observations, it is commonly found that the cirrus has to be in some way "clumpy" with some areas denser than others (see e.g. Popescu & Tuffs 2005).

General geometry Monte-Carlo codes

There is another set of models which employ the Monte-Carlo technique. This technique allows for a more general geometry in order to deal with galaxy formation codes which calculate spacial information for a simulated galaxy. Examples of this type of code include DIRTY (Gordon et al. 2001 and Misselt et al. 2001); Bianchi (1996); Baes et al (2003); RADISHE (Chakrabarti et al 2008; Chakrabarti & Whitney 2009); TRADING (Bianchi 2007,2008); SUNRISE (Johnnson 2006 and Johnnson, Groves & Cox 2009) and ART^2 (Li et al 2008). Of these perhaps the most advanced are the SUNRISE model and the TRADING model. These two models include the extinction and emission from the dust as well as the clumping of gas and stars, SUNRISE through the addition of starforming regions, following Groves et al. (2008) and TRADING where adaptive mesh techniques allows the code to reach resolutions of star-forming complexes. The main drawback of Monte-Carlo codes is the very large computational times required to model each galaxy.

This could be a problem if, in particular, you were interested in generating a theoretical catalogue of thousands of galaxies which could be compared to large observational surveys.

1.5 An existing dust model - GRASIL

The GRASIL code was designed as a general purpose dust model. Within the code the choice of the galactic profile is such that it can be used to model the SED of many types of galaxies. The radiative transfer treatment includes a sophisticated treatment of both the cirrus and molecular cloud components, but does not rely on the Monte-Carlo technique, so is relatively quick. Piovan et al. (2006) presents another dust model which has also been constructed with similar goals in mind and shares many characteristics with GRASIL.

The GRASIL model combines a stellar population code, which calculates the bare stellar emission of the galaxy, with a radiative transfer dust code, which calculates the effect of the ISM of the galaxy on this stellar emission. The final output is a dust affected galactic SED. In order for the stellar population part of the code to simulate the stellar emission, it first requires knowledge of the chemical evolution of the galaxy.

It has been used successfully in two main ways:

- In combination with a simple chemical evolution model, Che-Evo, in order to calculate SEDs, which can then be used to study individual galaxies, inferring the galaxies properties, for example star-formation histories and dust masses (e.g. Panuzozo et al 2007a,b; Vega et al 2008; Iglesias-Paramo et al 2007)

- In combination with more sophisticated galaxy evolution models, particularly semi-analytic models (SAMS), in order to predict SEDs which can be compared to observed SEDs, thereby testing the proposed galaxy formation scenarios proposed. The GRASIL code has been used successfully with the GALFORM model (Cole et al 2000; Granato et al 2000; Baugh et al 2005; Lacey et al 2008), the MORGANA model (Monaco et al 2007; Fontanot et al 2007, 2009); and the ABC model (Granato et al 2004; Silva et al 2005; Lapi et al 2006; Cook et al 2008).

A third application, testing the importance of the dust evolution on the SEDs of

galaxies of different type, was carried out by Schurer et al (2008), details of which can be found in chapter 3.

An overview of the GRASIL model will be given here, more details can be found in Silva et al 1998 and Silva 1999, hereafter S98 and S99 respectively.

1.5.1 Stellar Population Model

The single stellar populations included in GRASIL are based on the Padova stellar models and cover a large range of ages and metallicity. The SSPs include asymptotic giant branch (AGB) isochrones, which incorporate a treatment of the dusty envelope around these stars, and have been calibrated on the most recent data for the V-K colours of the large magellanic cloud's star clusters (see Marigo et al. 2008; Bressan et al. 1998). The spectral synthesis technique consists in summing up the spectra of each stellar population provided by a simple stellar population (SSP) of appropriate age and metallicity (Z), weighted by the star-formation rate (SFR) (Ψ) at the time of the star's birth (Bressan et al. 1994):

$$F_\lambda(t_G) = \int_0^{t_G} SSP_\lambda(t_G - t, Z(t)) \times \Psi(t) dt \tag{1.1}$$

Where t_G is the age of the galaxy and t is the birth age of an individual SSP (see also below the treatment of age dependent attenuation).

1.5.2 Dust Model

GRASIL then calculates the radiative transfer of the starlight, the heating of the dust grains and the emission from these grains, with a self-consistent calculation of grain temperatures, for an assumed geometrical distribution of the stars and dust and a specific grain model.

The stars can be modelled in two main components: the bulge and the disc, the latter not being present when modelling elliptical galaxies. The geometry is shown in figure 1.9. The spherical bulge has an analytic King profile, $\rho \propto (r^2 + r_c^2)^{-3/2}$ extended up until the tidal radius $r_t = 10^{2.2} r_c$, where the scalelength r_c is a free parameter. The disc is described by a radially and vertically exponential profile, $\rho \propto exp(-r/r_d) exp(-|z|/z_d))$

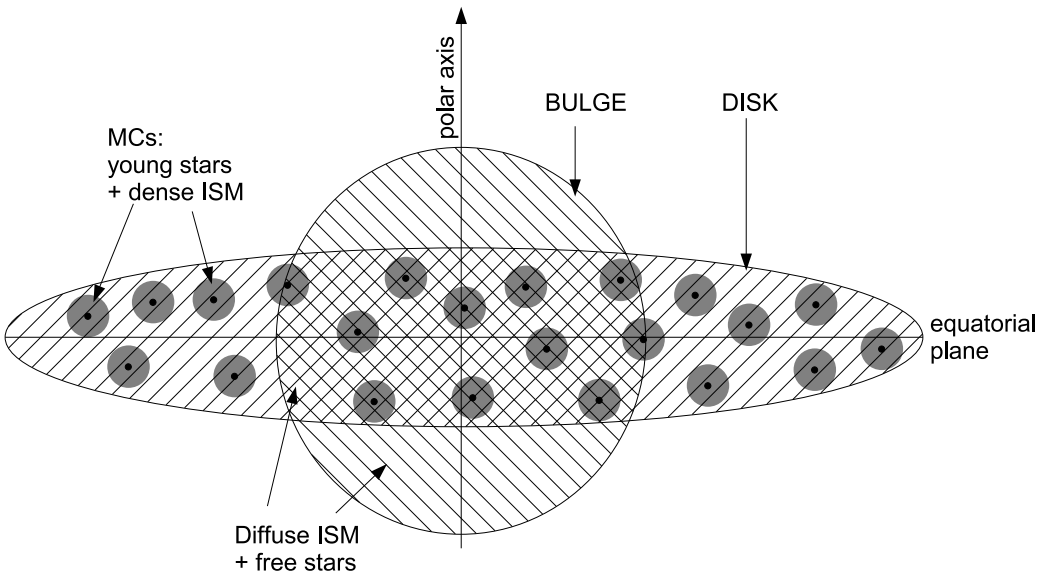

Figure 1.9: Sketch of geometry of stars and dust in the GRASIL model for the case of a galaxy with both a disc and a bulge.

truncated at $r_t = 6R_d$ where the radial scalelength r_d and vertical scalelength z_d are free parameters.

The dust component has the same disc and bulge profiles as the stellar component but can have scalelengths independent of the stellar component. Within these profiles the gas and dust is further split into two main components: dense molecular clouds and diffuse cirrus. The ratio of the total mass in gas located in the molecular clouds to the total gas mass is a free parameter f_{mc}. When a galaxy is composed of only a bulge or a disc, the molecular clouds are dispersed evenly throughout the galaxy. However, when a galaxy is modelled with both a disc and a bulge, as shown in figure 1.9 the molecular clouds are located solely in the disc. Stars are assumed to form inside the molecular clouds and progressively escape them on a timescale t_{esc}. Specifically, the fraction of stars inside clouds at time t after they formed is assumed to be:

$$F(t) = \begin{cases} 1 & (t < t_{esc}) \\ 2 - \frac{t}{t_{esc}} & (t_{esc} < t < 2t_{esc}) \\ 0 & (t > 2t_{esc}) \end{cases} \tag{1.2}$$

where t_{esc} is a free parameter of the model. The radii and mass of the molecular clouds are also free parameters of GRASIL, though the results actually depend only on the combination M_{mc}/R_{mc}^2, which determines, together with the dust-to-gas ratio, the optical depth of the clouds (see S98), where M_{mc} is the mass of a molecular cloud and R_{mc} is the radius of a molecular cloud.

The dust is assumed to consist of a mixture of carbonaceous and silicate grains and polycyclic aromatic hydrocarbons (PAH), see § 1.1.5. The carbonaceous particles are assumed to have the optical properties of randomly-orientated graphite spheres. The silicate grains are assumed to be amorphous silicates. The optical properties of silicate and graphite grains are taken from Laor & Draine (1993), the optical properties of PAH molecules from Draine & Li (2007). The size distribution used in this paper for our fiducial models are those chosen by S98 to match the extinction and emissivity curves of the local ISM. The size distribution for both the carbon and silicate components are described by a double power

law specified by equation 1.3.

$$\frac{dn_i}{da} = \begin{cases} A_i n_H a^{\beta_1} & a_b < a < a_{max} \\ A_i n_H a^{\beta_1 - \beta_2} & a_{min} < a < a_b \end{cases} \tag{1.3}$$

Where dn_i is the number density of grains of type i with radii in the interval [a, a + da], n_H is the number density of H nuclei and A_i is the atomic abundance of type i relative to hydrogen. The size ranges (a_{min}), (a_b) and (a_{max}) of the dust grains and the exponents β_1 and β_2 are free parameters. The values of these parameters chosen in order to match observations are, for the graphite grains: $a_{min} = 8\mathring{A}$, $a_b = 50\mathring{A}$, $a_{max} = 2500\mathring{A}$, $\beta_1 = -3.5$ and $\beta_2 = -4.0$. For the silicate grains: $a_b = 50\mathring{A}$, $a_{max} = 2500\mathring{A}$ and $\beta_1 = -3.5$.

The luminosities of the different stellar components (the stars in the bulge, in the disc and young stars still in clouds) are calculated using the population synthesis model described. The GRASIL code then calculates the radiative transfer of the starlight through the specified dust distribution. For the molecular clouds a full radiative transfer calculation is performed. However for the diffuse dust, the effects of scattering are only approximated by assuming an effective optical depth related to the true absorption and scattering optical depths by: $\tau_{eff} = [\tau_{abs}\,(\tau_{abs} + \tau_{sca})]^{1/2}$ and assuming that there is no re-absorption of the radiation emitted by the cirrus. Using these approximations, GRASIL calculates, for each point inside and outside the galaxy, the dust attenuated stellar radiation field. Once this is known, it is then possible to calculate for each point inside the galaxy the absorption of radiation, thermal balance if in thermal equilibrium or thermal fluctuations if not, and hence, re-emission for each grain composition and size. Combining the contributions from the attenuated starlight and from the dust re-emission, a SED for the galaxy is calculated which depends on the angle from which the galaxy is viewed.

Chapter 2

Modelling the effects of dust evolution on the SEDs of galaxies

In this chapter we present photometric evolution models of galaxies, in which, in addition to the stellar component, the effects of an evolving dusty interstellar medium have been included with particular care. Starting from the work of Calura, Pipino & Matteucci (2008), in which chemical evolution models have been used to study the evolution of both the gas and dust components of the interstellar medium in the solar neighborhood, elliptical and irregular galaxies, it has been possible to combine these models with a spectrophotometric stellar code that includes dust reprocessing (GRASIL) (S98) to analyse the evolution of the spectral energy distributions (SED) of these galaxies. We test our models against observed SEDs both in the local universe and at high redshift and use them to predict how the percentage of reprocessed starlight evolves for each type of galaxy. The importance of following the dust evolution is investigated by comparing our results with those obtained by adopting simple assumptions to treat this component. The bulk of this chapter has been previously published in a refereed paper Schurer et al. (2009) as well as a conference proceeding: Schurer et al (2008).

2.1 Introduction

As discussed in chapter 1, the correct treatment of the radiative transfer through the dust component is clearly an important problem. Consequently many models have been proposed to calculate this effect, some of which are described in § 1.4, one model is described in slightly more detail in § 1.5 and another is presented in detail in chapter 4. One of the main limitations of nearly all these models is that they do not follow the evolution of the dust component in detail due to the added complexity this would involve. Instead they are forced to rely on several common assumptions.

Many of the proposed models are based on the dust composition models calculated for the Milky Way (see § 1.1.5), and for simplicity use this same dust composition for all morphological types of galaxies and for every stage of their evolution. However, unsurprisingly, observations indicate that dust properties are likely to vary with age and morphological type. For example observations of very high redshift and hence young galaxies (Maiolino et al. 2004), and dwarf irregular galaxies (eg. Galliano et al. 2005), have been used to infer very different sizes and compositions of dust grains in these galaxies than those observed in the Milky Way. So it is unlikely to be sufficient to model the effects of dust at all redshifts and in galaxies with very different properties and star formation histories using only one grain distribution model. It is also common to calculate a total mass of dust by assuming a dust-to-gas mass ratio proportional to the metallicity of the galaxy, with the same constant of proportionality in all environments (e.g. Granato 2000 et al.; Baugh 2005 et al., similarly our new SED-dust model GRASIL-3D also makes this assumption). An assumption which is far from certain, for example it has been found that in dwarf irregular galaxies a lower than expected dust-to-gas ratio has been observed (Hunt, Bianchi & Maiolino 2005; Galliano et al. 2003, 2005). Hence it would be beneficial when modelling the effects of dust reprocessing in a range of different environments to be able to relax these assumption and select appropriate dust properties for each galaxy individually. Unfortunately observational evidence regarding the exact dust composition outside our own galaxy is very limited. It is therefore necessary, at the present time, in order to model SEDs of galaxies of different type and at different stages in their evolution to rely on theoretical

models which follow the evolution of dust (see § 1.2).

In this chapter the effects of making these basic assumptions for the dust evolution will be examined. This was done by using the dust evolution model of CPM08 (see § 1.2) to follow the chemical and dust grain evolution of galaxies of different morphology and then combine it with the GRASIL code (S98) (see § 1.5) to use the calculated stellar and dust evolution in order to calculate the SED expected for the galaxy. The importance of following the dust evolution is tested by comparing these fiducial SEDs with SEDs generated adopting two common simplifications: That the dust to gas mass ratio is proportional to the metallicity, and that the dust composition in all galaxies is equal to that derived for the Milky Way. The main goal of this work will be a quantitative comparison between the SEDs generated using the fiducial model and that adopting the simplifications. In such a way it is possible to estimate what errors could theoretically be expected from adopting such assumptions.

We test our models of the three morphologies (spirals, irregulars and ellipticals) against observed SEDs in the local universe (Dale et al. 2007) and the model elliptical galaxies at early times against observations of their expected high redshift counterparts, SCUBA galaxies (Clements et al. 2008) and massive post-starburst galaxies at high redshift (Wiklind et al. 2008). We also use the models to predict how the percentage of reprocessed starlight evolves for each type of galaxy.

In this work it was only possible to follow in detail the evolution of the chemical composition of the dust and not how the size distribution and chemical makeup of the individual grains evolve, a potentially large but for now unavoidable limitation. To test this, alternative size distributions for the irregular galaxy and for the young starbursting elliptical galaxy were proposed based on observed extinction curves and the resultant SEDs are presented.

The plan of this chapter is as follows: In § 2.2 the chemical and dust evolution model is explained, in § 2.3 the integration of the chemical-dust-evolution model with GRASIL is briefly described, and the choice of parameters discussed, in § 2.4 the calculated SEDs are presented and are compared to observations, in addition a quantitative comparison is made between them and the SEDs generated using the simple dust assumptions, in §

2.5 the implications of our work is discussed. Some concluding remarks are given in § 2.6.

2.2 Chemical evolution models

The chemical evolution models that this chapter is based upon are presented in the CPM08 paper. These models follow the chemical evolution of several different elements in both the gas and the dust components of the ISM, of spiral, elliptical and irregular galaxies. More detailed descriptions of these models can be found in Matteucci & Tornambè (1987), Matteucci (1994) and Pipino et al. (2002, 2005) for the elliptical galaxies, Chiappini et al. (1997, 2001) for the spirals and Bradamante et al. (1998) for irregular galaxies. For convenience the main details will be summarized here.

2.2.1 Gas Evolution

All the models consider only one gas phase. In all models the instantaneous recycling approximation is relaxed and the stellar lifetimes are taken into account. The abundance of several of the elements in the gaseous phase of the ISM (H, He, Li, C, N, O, α-elements, Fe, Fe peak elements and S-process elements) are followed from the birth of the galaxy. The following processes are considered.

- The subtraction of elements from the gaseous phase of the ISM due to star formation.
- The production in stellar winds in low and intermediate mass non-binary stars with masses 0.8 - 8 $M_{\odot}$.
- The production in type Ia SNe by binary stars in systems with combined masses 3-16 $M_{\odot}$.
- The production in type II SNe of massive stars of masses 8 - 100 $M_{\odot}$.
- The increase in primordial elements due to infalling gas.
- The loss of elements from gas outflows due to galactic wind as the thermal energy of the gas exceeds its binding energy (only present in the irregular and elliptical models).

Low and intermediate mass stars contribute to the ISM metal enrichment through quiescent mass loss and a planetary nebula phase by adopting prescriptions by van den Hoek & Groenwegen (1997). For massive stars and type Ia SNe the empirical yields suggested by François et al. (2004) are adopted.

The star-formation efficiencies and the rate of infall in addition to the Initial Mass Function (IMF) are selected for each of the galaxy morphologies in order to reproduce observed chemical abundances.

Spirals

The galactic disc is approximated by several independent rings, 2 Kpc wide, without interchange of matter between them. In this picture, spiral galaxies are assumed to form as a result of two main infall episodes. During the first, the halo and the thick disc are formed. During the second, a slower infall of external gas forms the thin disc with the gas accumulating faster in the inner than in the outer region, with timescales equal to about 1 Gyr and 8 Gyr respectively (inside-out scenario). The star formation rate is given by the expression:

$$\psi(r,t) = \nu \left[\frac{\sigma(r,t)}{\sigma(r_\odot,t)}\right]^{2(k-1)} \left[\frac{\sigma(r,t_{Gal})}{\sigma(r,t)}\right]^{k-1} \sigma^k_{ISM}(r,t) \tag{2.1}$$

Where $\sigma(r,t)$ is the total mass (gas + stars) surface density at a radius r and time t, $\sigma(r_\odot,t)$ is the total mass surface density in the solar region. The starformation efficiency, ν, is set to $\nu = 1\ Gyr^{-1}$ and becomes zero when the surface density drops below $\sigma_{th} = 7\ M_\odot pc^{-2}$ as suggested by Kennicutt (1989). For the gas density exponent k a value of 1.5 has been assumed by Chiappini et al. (1997) in order to ensure a good fit to the observational constraints of a large set of local spirals (Kennicutt 1998). The resultant star formation history is shown in figure 2.1a for a 2 Kpc wide ring located 8 Kpc from the Galactic centre, which represents the solar neighborhood.

The IMF adopted is a simplified two-slope approximation to the actual Scalo (1986) IMF which is expressed by the formula:

$$\phi_{scalo}(m) = \begin{cases} 0.19 \cdot m^{-1.35} & \text{if } m < 2M_\odot \\ 0.24 \cdot m^{-1.70} & \text{if } m > 2M_\odot \end{cases} \tag{2.2}$$

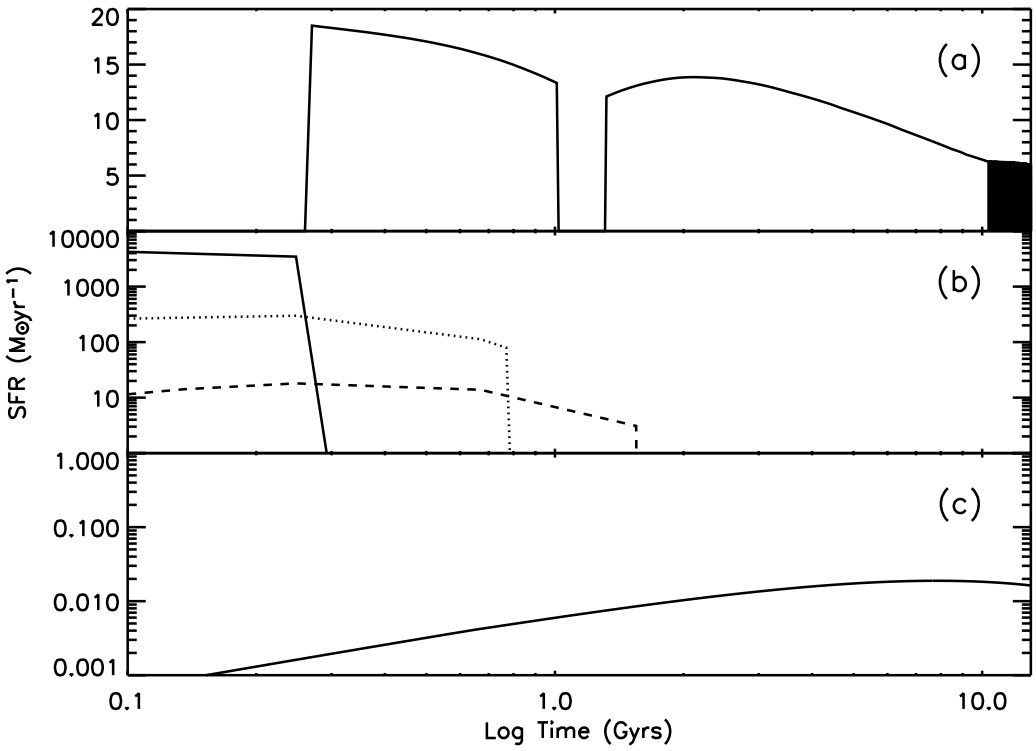

Figure 2.1: Predicted SF history in; a) the solar neighborhood, where the threshold effect is quite clear after a time of about 10 Gyrs ; b) elliptical galaxies of masses $10^{10}M_{\odot}$ - dashed line, $10^{11}M_{\odot}$ - dotted line,$10^{12}M_{\odot}$ - solid line; c) irregular galaxies

Ellipticals

There is a long lasting debate on the scenario for the formation of elliptical galaxies. While it is clear that dark matter structures build up in a hierarchical fashion from smaller to bigger ones, there are strong hints that the much more complex physics of visible matter, impossible to simulate from first principles, reverses, to some level this trend. Indeed, recent observations made in the past few years (Cowie et al. 1996; Guzman et al. 1997; Brinchmann & Ellis 2000; Kodama et al. 2004; Juneau et al. 2005; Bell et al. 2005; Noeske et al. 2007), add further support to previous suggestions coming mostly from detailed studies of chemo-photometric properties (e.g. Thomas et al. 2005 and references therein) for so called "cosmic downsizing", that large elliptical galaxies formed their stars at high redshift in a huge burst of star formation, and after that evolved in a almost passive way (for a recent comprehensive review see Renzini 2006). Indeed, a few modern semi-analytic models (e.g. Granato et al. 2004, Bower et al. 2006) try to obtain, within a computation of hierarchical build-up of dark matter potential wells, a rapid and high redshift assembly of baryons in large galaxies (which are dominated by ellipticals), in other words breaking the hierarchy of galaxy formation and mimicking to some extent the monolithic scenario (Somerville 2005). A fundamental ingredient may be a proper treatment of the AGN feedback, neglected in all previous computations. Which could make passive these galactic system after an early ($z > 2$) and short phase (~ 1 Gyr) of rapid mergers of similar sub-units.

A detailed modelling of the physical mechanisms responsible for the downsizing is clearly outside the scope of this present work. Thus, here we adopt and investigate the simple monolithic model proposed in CPM08 which has been carefully calibrated against the chemistry of ellipticals, deferring the investigation of alternative and more complex possibilities to future work. The elliptical galaxies in CPM08 form as a result of a rapid collapse of a homogeneous sphere of primordial gas leading to a period of intense star-formation. This star-formation is assumed to halt as the energy of the ISM, heated by stellar winds and SNe explosions exceeds the binding energy of the gas, sweeping away almost all of the residual gas. At later times the galactic wind is maintained by type Ia SNe provided that the thermal energy exceeds that of the binding energy of the gas.

The star-formation rate is a Schmidt law expressed as:

$$\psi = \nu G^k(t) \tag{2.3}$$

Where G is the total gas mass with an exponent $k = 1$. The star formation efficiency, ν, is assumed to increase with mass (as originally postulated in Matteucci 1994) in order to reproduce the positive correlation of [Mg/Fe] with mass (e.g. Thomas et al. 2005). In this chapter models of galaxies of three different masses have been followed. Galaxies with a final stellar mass of $10^{10} M_{\odot}$ (the low mass galaxy described in CPM08) with a star-formation efficiency $\nu = 5\ Gyr^{-1}$. Galaxies with a final stellar mass of $10^{11} M_{\odot}$ (model La1 as described in CPM08) with a star-formation efficiency $\nu = 15\ Gyr^{-1}$. Galaxies with a final stellar mass of $10^{12} M_{\odot}$ (model Ha1 as described in CPM08) with a star-formation efficiency $\nu = 25\ Gyr^{-1}$. The star-formation history is shown in figure 2.1b.

The IMF adopted here is a Salpeter IMF of form:

$$\phi_{Salp}(m) = 0.17 \cdot m^{-1.35} \tag{2.4}$$

The IMF in different galactic system is a topic hotly debated in literature. For instance, Baugh et al. (2005) showed that the only way to reproduce the statistic of sub-mm sources, usually considered the precursor of local ellipticals, in the context of their "standard" semi-analytic model is to adopt an extremely top-heavy IMF during mergers. However their model still shows discrepancies with observed trends of α/Fe in local ellipticals (Nagashima et al 2005), and predicts masses of sub-mm sources too low by more than one order of magnitude Swinbank et al (2008).

Irregulars

Two separate formation scenarios for irregular galaxies were proposed in CPM08. In this work only the first scenario is followed, in which the irregular galaxies are assumed to assemble from the infall of protogalactic small clouds of primordial chemical composition and to produce stars at a slower rate than spirals. This formation scenario has been proposed to model dwarf irregular galaxies of a magellanic type.

The star formation rate is a Schmidt law as shown in equation 2.3, with $k = 1$ and a low star-formation efficiency $\nu = 0.05\ Gyr^{-1}$. The star-formation history is shown in figure 2.1c. The IMF adopted is Salpeter as given by equation 2.4.

2.2.2 Dust Evolution

In addition to the gas phase the CPM08 model also follows the evolution of several of the elements in the interstellar dust. The elements considered are C, O, Si, Mg, Fe, S. The factors considered are similar to those affecting the evolution of the ISM and are:

- The subtraction of dust elements due to star formation.
- The production in stellar winds in low and intermediate mass non-binary stars with masses 0.8 - 8 $M_{\odot}$.
- The production in type Ia SNe by binary stars in systems with combined masses 3-16 $M_{\odot}$.
- The production in type II SNe of massive stars of masses 8 - 100 $M_{\odot}$.
- The loss of dust in outflows due to galactic wind.
- The destruction of dust primarily from SNe shocks.
- The accretion of dust in dense molecular clouds.

The dust condensation efficiencies assumed in the stellar winds and in SNe are those suggested by Dwek (1998).

The destruction rates in SNe shocks and the accretion rates in molecular clouds follow suggestions by McKee (1989) and Dwek (1998).

Spirals

In the paper of CPM08 only the dust properties of the solar neighborhood are considered.

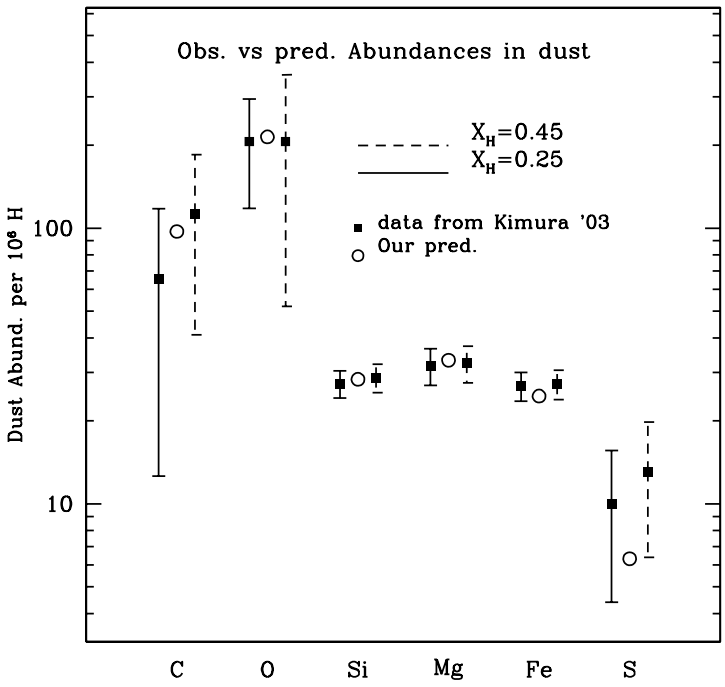

Figure 2.2: Comparison between the predicted dust abundances for the refractory elements by the CPM08 model for the solar neighbourhood (circles) and the elemental abundances observed in the local interstellar cloud by Kimura, Mann & Jessberger (2003) (squares), using two different estimates of the ionization fraction of hydrogen

The accretion rates are set to realistic values following Dwek (1998) and the destruction rates are set separately for each element and are related to their individual condensation temperatures, so that depletion fractions of the elements in the model can reproduce those observed in the local warm medium. The results are shown in figure 2.2. For the purposes of this work we are interested in following the evolution of the mass of carbon dust particles and silicates (dust particles composed of O, Mg, Si, S, Ca, Fe). The evolution of these particles are shown in figure 2.3a.

The solar neighborhood is believed to be representative of the Galaxy as a whole. Hence, for this work, the properties calculated for the solar neighborhood will be used as global properties for the whole galaxy.

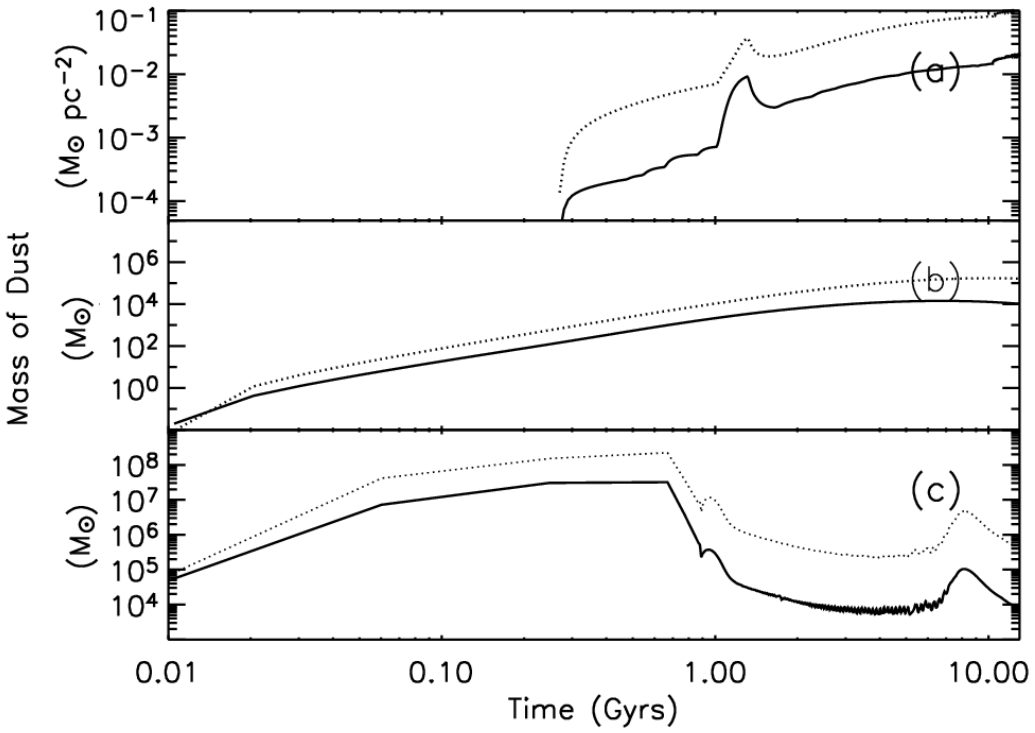

Figure 2.3: Predicted evolution of the dust masses for galaxies of different morphologies, showing evolution of carbon (solid line) and silicates (dashed line); a) spiral galaxies ; b) Elliptical galaxies; c) Irregular galaxies

Ellipticals

For the initial starburst phase the same efficiencies for accretion and destruction as in the solar neighborhood are assumed. However, after the onset of the galactic winds elliptical galaxies will be largely devoid of cold gas. Therefore it is assumed that no accretion can occur and a much lower value for the destruction efficiency is used, as derived by McKee (1989), for a hot and rarefied medium. Also an additional destruction term is included to treat the thermal sputtering which is thought to be the dominant source of destruction in hot plasmas. Following Itoh (1989) we assume that in a ~ 1 keV plasma nearly 90 per cent of the dust grains will evaporate by sputtering in $\tau_{destr_{sput},i} \sim 10^5/n_e$ $(yrcm^{-3})$ where the electron density has been self-consistently evaluated at each timestep. The resultant dust evolution is shown in figure 2.3b.

Irregulars

For irregular galaxies the destruction value for the solar neighborhood is used. However, since the observed molecular H content in dwarf irregular galaxies is very small, with molecular-to-atomic gas fractions of ~ 10 per cent or lower (Lisenfeld & Ferrara 1998, Clayton et al. 1996) it is assumed that no accretion can occur. The resultant dust evolution is shown in figure 2.3c .

2.3 Interfacing with the GRASIL dust model

The model which we used to calculate the SEDs of the chemical and dust evolution model discussed above is the GRASIL model, details of which are given in § 1.5. This model combines a stellar population synthesis code to calculate the stellar spectrum with a model to calculate the radiative transfer of the starlight through the dusty ISM.

2.3.1 Choice of parameters

The value of the GRASIL parameters chosen for the different galaxies are listed in table 2.1. The reasons for the choices made are given below:

Table 2.1: Adopted Values for the GRASIL parameters, - for the elliptical models the values outside the brackets are for the starbursting phase, the values in the brackets are for the passively evolving phase

	Spiral	Elliptical		Irregular
		$10^{11} M_\odot$	$10^{12} M_\odot$	
t_{esc} [1]	2	250 (0)	250 (0)	2
f_{mc} [2]	0.5	0.5 (0)	0.5 (0)	0.1
r_c^* [3]	...	0.21 (0.21)	0.68 (0.68)	...
r_d^* [4]	2.35	... (...)	... (...)	1
z_d^* [5]	0.14	... (...)	... (...)	0.5
r_c^d [6]	...	0.21 (0.42)	0.68 (1.36)	...
r_d^d [7]	5	... (...)	... (...)	1
z_d^d [8]	0.1	... (...)	... (...)	0.5
M_{mc} [9]	10^6	10^6 (10^6)	10^6 (10^6)	10^6
R_{mc} [10]	16	16 (16)	16 (16)	40

[1] Timescale for the evaporation of molecular clouds, in $Myrs$. [2] Fractionary gas content in the molecular clouds. [3] Radial scalelength of the stellar component in the bulge, in Kpc. [4] Radial scalelength of the stellar component in the disc, in Kpc. [5] Vertical scalelength of the dust component in the disc, in Kpc. [6] Radial scalelength of the dust component in the bulge, in Kpc. [7] Radial scalelength of the dust component in the disc, in Kpc. [8] Vertical scalelength of the dust component in the disc, in Kpc. [9] Total gas mass in each molecular cloud, in $M_\odot$. [10] Radius of each molecular cloud, in pc

Escape timescale (t_{esc})

This is a very important parameter controlling how long the young stars remain in their birth clouds. A value of 2 Myrs for spiral and irregular galaxies is chosen following Granato et al. (2000). S98 found that larger values were needed to fit local starbursts: $t_{esc} = 20 - 60$ Myrs, to reflect the dense dusty environments found. In a similar way one would expect much higher escape timescales for the early starbursting phase of elliptical galaxies. The rates of star-formation however predicted by the CPM08 model far exceed those observed in local starbursting galaxies and as a result the escape timescale could reasonably be expected to be longer still. This value remains a free parameter of the model since the precise dust condition present in SCUBA galaxies are unknown. In this work it has been set to 250 Myrs, a value found to provide good fit to SCUBA galaxies at high redshift (see § 2.4.3). After the onset of the galactic winds in the elliptical galaxy all of the cold gas is blown out of the galaxy and molecular clouds cannot form, as a result star formation is stopped and consequently $t_{esc} = 0$.

Optical depth of molecular clouds (M_{mc}, R_{mc})

Combined these two parameters control the optical depth of the molecular clouds according to the ratio M_{mc}/R_{mc}^2, where M_{mc} is the mass of a molecular cloud and R_{mc} is the radius of a molecular cloud. Like in § 4.4.2, following Granato et al. (2000) values of $M_{mc} = 10^6 M_\odot$ and R_{mc}=16 pc are chosen for the spiral and elliptical galaxies, values which have been found to give good SED fits and are consistent with observations.

GRASIL has not been previously used to model irregular galaxies. In order to fit the SED in the MIR, molecular clouds with a lower optical depth had to used in this work (see § 2.4.2).

Ratio of gas mass in molecular clouds to total gas mass (f_{mc})

For spiral galaxies we choose a value of $f_{mc} = 0.5$ for this parameter which agrees well with the values used to fit local spirals in S98.

The passively evolving late phase in elliptical galaxies will have no molecular clouds

so $f_{mc} = 0$. A value of 0.5 is adopted for the starbursting stage.

Lower value for the molecular-to-atomic gas fraction are observed in irregular galaxies than in spiral galaxies (see § 2.2.2) and since most of the hydrogen in molecular clouds is in H_2, while most of the diffuse cirrus gas will be atomic H_1 this lower value suggests a lower value of f_{mc}. Consequently a value of $f_{mc} = 0.1$ has been chosen.

Geometry (r_c^*, r_d^*, z_d^*, r_c^d, r_d^d, z_d^d)

The spiral galaxy is modelled as a pure disc for both the stellar and the dust components with scalelengths, (r_d^* and z_d^* for the stellar component and r_d^d and z_d^d for the dust component) set following the results of Misiriotis et al. (2006), who used COBE/DIRBE maps and COBE/FIRAS spectra to constrain a model for the spatial distribution of the dust, the stars and the gas in the Milky Way.

The elliptical galaxies are modelled using a pure bulge for both the stellar and the dust components. The elliptical stellar scalelength, r_c^* is given by the chemical evolution model of CPM08. S98 found that in order to obtain a good fit to a template constructed from local elliptical galaxies a dust scalelength, r_c^d, much larger than the stellar scalelength was required. This conclusion was also reached by Panuzzo et al. (2007) who found it necessary to have dust scalengths almost double the stellar ones in order to fit a late type galaxy of the Virgo cluster. Spatially extended dust has also been observationally detected by Temi, Brighenti & Mathews (2007), who have detected spatially extended dust in two optically normal galaxies NGC 5044 and NGC 4636. Although it should be noted that Temi et al. (2007) concluded that due to the short sputtering lifetime for extended dust $\sim$ 7 Gyrs and no evidence for a recent merger, that the most likely source of this dust was due to galactic winds powered by a central AGN, whereas in the CPM08 model the proposed mechanism for the galactic wind is different, with SN1a and stars alone able to power the wind for several Gyrs (see Pipino et al. 2005). Therefore due to observational evidence and also typical values used in previous studies, in the passively evolving phase, we have set the dust scale-length to be twice the stellar scale-length. For the early star-bursting phase the dust is likely to be more concentrated, so the dust scale-length is set equal to the stellar one.

The irregular galaxy is modelled as a pure disc for both the stellar and the dust components. Observations for the dust distribution in irregular galaxies are still largely inconclusive so we have set the dust scale-length equal to the stellar one.

2.3.2 Generating SEDs

In order for GRASIL to be able to calculate the intrinsic stellar SED of a galaxy the stellar population code requires a star formation history and a metallicity evolution which are generated by the chemical evolution code, and an IMF which is set to that used in the chemical evolution code. To calculate the dust affected SED GRASIL requires a total mass in dust (in this work the dust-to-gas ratio will be the quantity discussed) and chemical composition of dust (the carbon over silicate ratio) which are set by the dust evolution model the other geometrical parameters are then set to the values described in § 2.3.1 and the grain size distribution to that derived in S98, details of which are given in § 1.5 and table 2.2.

For comparison SEDs are also calculated for galaxies with the chemical evolution described by the CPM08 model but without the detailed dust evolution properties. Instead two common assumptions will be adopted.

- That the ratio of the dust mass to gas mass is proportional to the metallicity, through a constant normalised to the Milky Way, using the value 0.008 calculated from observations for the dust to gas mass ratio as discussed in CPM08. So *dust mass* $\propto$ *metallicity*$\times$ *gas mass*.

- That the chemical composition does not evolve. So that the fraction of carbon to silicate will be set to the value 0.19 for all times and morphologies, a theoretical value found by CPM08 for the ratio of C/Si at 13 Gyr in the solar neighborhood model.

In addition, for the irregular galaxy and for the starbursting phase in elliptical galaxies, the effect on the SED of releasing a third assumption, made routinely in other works as well as for the fiducial models in this work, namely that the dust size grain distribution does not evolve and remains constantly identical to that of the Milky Way is investigated. Details

Table 2.2: Parameters for size distribution of the dust component in different environments (see equation 1.3). The MW size distribution is that derived by S98 to match observations from the MW. The SMC and QSO SDSSJ1048+46 size distributions are calculated in this work to match observed extinction curves.

	MW (S98)	SMC	QSO SDSSJ1048+46
Carbon			
a_{min} ($\AA$)	8	5	...
a_b ($\AA$)	50	25	400
a_{max} ($\AA$)	2500	1000	700
β_1	-3.5	-3.0	-3.5
β_2	-4.0	-4.5	...
Silicate			
a_{min} ($\AA$)	...	...	...
a_b ($\AA$)	50	50	5
a_{max} ($\AA$)	2500	10000	10000
β_1	-3.5	-3.9	-3.5
β_2	...	...	...

of the size distributions used are given in table 2.2 (see also equation 1.3), more details of the choices made will be given in § 2.4.2 and § 2.4.3.

For clarity when the full dust treatment is used as described in the CPM08 paper it will be referred to as the full CPM08 model. When the two assumptions outlined above are adopted it will be referred to as the simple dust model. The difference between the two models will be referred to as the *disparity*. This would be the error introduced by the adoption of the simplifications if one assumes that the fiducial model is correct. It is only a theoretical error.

2.3.3 Treatment of PAH molecules

The abundance of PAHs is calculated from the chemical composition of the dust predicted by the CPM08 model, specifically their abundance is proportional to the total abundance of carbon molecules in the dusty component of the ISM. The exact treatment

of the absorption and emission processes for the PAH bands are then calculated following the same procedure described in S99 and Vega et al. (2005) but updated with the most up-to-date cross-sections outlined in Draine & Li (2007) calculated using new laboratory data and spectroscopic data observed by the *spitzer space telescope*

Although PAH emissions have been found to be a ubiquitous feature of both the Milky Way and external galaxies it is worth noting that the strengths of the PAH bands have been found to vary between galaxies, with low metallicity galaxies and galaxies hosting AGNs in particular being found to be deficient in PAH emission. This has led several authors to speculate that the abundances of PAHs could be linked to the particular environmental conditions present in their host galaxy. For example it thought that they could be preferentially destroyed by strong UV radiation (e.g. Madden et al. 2006) and, could be more susceptible to SNe shocks (e.g. O'Halloran et al. 2006). This suggests that the evolution of PAHs may not necessarily be identical to that of the larger carbon grains. This effect has been partly accounted for by following the treatment of PAHs outlined in Vega et al. (2005). Where in order to agree with observations from around hot stars and H_{II} regions, from within our galaxy, the abundance of PAHs in the molecular clouds within GRASIL, where the UV radiation will be strongest, had to be suppressed by a large factor (≈ 1000 with respect to the cirrus component). Using such a prescription it was shown that GRASIL could reproduce the MIR spectrum of local star-forming galaxies.

Since in this work the evolution of the PAH dust population has not been specifically followed a detailed analysis of the spectrum in the MIR will not be possible. However linking the abundance of the PAHs to both the environment, by suppressing the PAH abundance in molecular clouds, and to the chemical composition of the dust should be a reasonable approximation and should be sufficient to highlight broad trends in the emission from this region.

2.3.4 Comparison to Observations

Low Redshift

The theoretical SEDs are compared to observed nearby galaxies of similar morphological type. The data sample used is that described in Dale et al. (2007) which presents SEDs for the 75 galaxies of the SINGS sample selected to span a wide range of morphologies, luminosities and IR to optical ratios. The data set comprises of galaxies at an average distance of ~ 10 Mpcs and contains SEDs from UV to radio wavelengths and includes :

- UV data from GALEX
- optical fluxes from the RC3 catalogue (de Vaucouleurs 1991).
- IR data from 2MASS, ISO, IRAS, SPITZER
- Sub-mm data from SCUBA
- Radio data - from literature including the New VLA Sky survey

All the galaxies of a particular morphological type are normalised to a common value in the K-band.

Our spiral model is designed to reproduce observations of the Milky Way, hence, to represent this morphological type, all spirals of type SBb to SBc and SAb to SAc in the SINGs data set were chosen, numbering twenty four. Our irregular galaxy is designed to reproduce observables of magellanic type irregular galaxies therefore the ten galaxies of type Im will be used. Our elliptical galaxy model is designed to reproduce the observables of passively evolving elliptical galaxies. Of the six elliptical galaxies in the SINGS sample two NGC 855 and NGC 3265 show very bright UV colours in addition to strong IR emission probably indicating ongoing moderate starformation. These two galaxies were identified as starforming galaxies by Dale et al. (2007) and were therefore not used in this work.

High Redshift

In order for the elliptical galaxy formation scenario presented in this work to be correct, one would expect to find observed galaxies at high redshift with SEDs similar to

those presented in this work. It is therefore essential to check that our young elliptical models are representative of the birth of typical elliptical galaxies at high redshift, by comparing the theoretical models to observations. However, for each of the masses of galaxy, only one star formation history has been followed with a fixed set of values for all of the parameters, so the models could not be expected to account for all high redshift objects. Also due to the sheer variability of high redshift galaxies the construction of an 'average' high redshift SED is not possible. Consequentially we compare our models to two different high redshift data sets (details of which can be found in the relevant sections), each thought to be representative of a different stage of the young galaxies evolution, to check that a reasonable proportion of the observed galaxies have SEDs similar to that predicted by our models.

A chi-squared fitting technique was employed to calculate the age and redshift of the model which gives the best fit to the observed points. Theoretical SEDs for the elliptical galaxy in its starbursting and post-starbursting phases were generated at several time steps, from 0.05 Gyrs to 2 Gyrs. Each of these SEDs is then normalised and compared to the observed spectra of the galaxy. Since neither of the data sets have spectroscopic redshifts the theoretical SEDs at all the time steps are compared to the observed SED for a range of redshift values and then the age and redshift which corresponds to the best fit is selected using a chi-squared minimisation technique. Due to the inherent uncertainty from using such a limited template set, in order to avoid spurious results the possible redshift range will be limited to within 30 per cent of the photometric redshift values calculated previously by other authors, using more sophisticated fitting procedures.

2.4 Results

2.4.1 Properties of Spiral Galaxies

Figure 2.4 shows the results for the theoretical SEDs generated at 12 Gyrs compared to the mean SED of spiral galaxies of types SBb to SBc and SAb to SAc from the SINGS sample. The theoretical model shows a good correlation with the observed spiral galaxies. This suggests that the assumption that the global properties of the galaxy can be

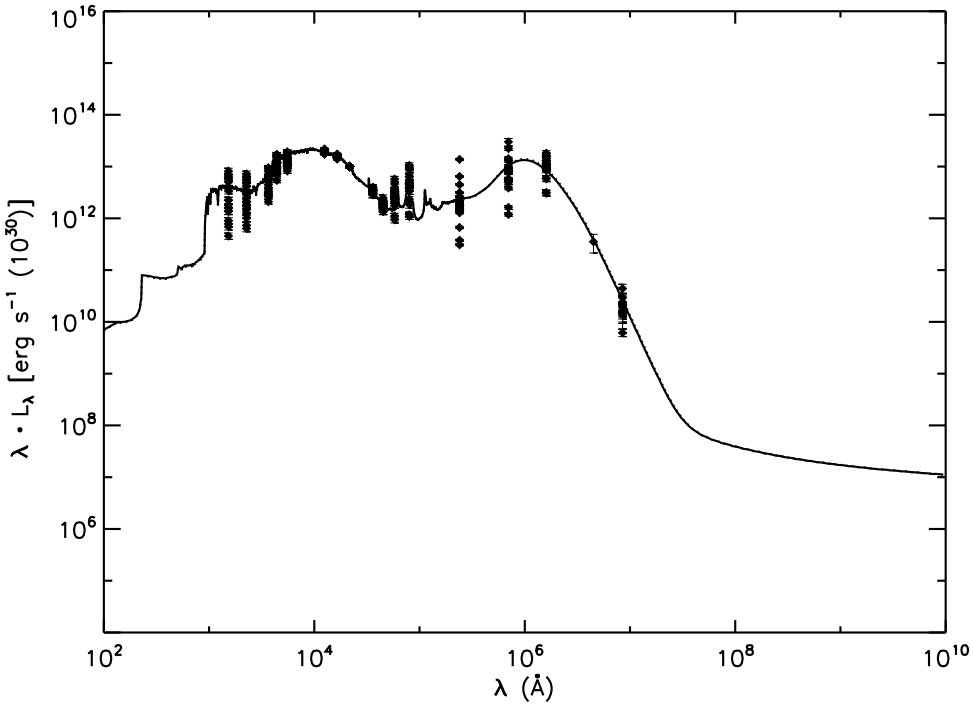

Figure 2.4: Comparison of theoretical spiral model at 12 Gyrs with the SEDs from all spiral galaxies of morphological type ranging from SBb to SBc and SAb to SAc in the SINGS sample, normalised to the k band. Solid line - Full CPM08 model. Dotted line - simple dust model

represented by the chemical and dust evolution model of the solar neighbourhood at late times is a good one.

The evolution of the SED of spiral galaxies is shown in figure 2.5. Due to the mainly quiescent slow evolution of the spiral galaxies the SEDs do not show large changes throughout their lifetime and there is little variation in the percentage of starlight reprocessed by the galaxy which for ages greater than 1 Gyr remains fairly constant at a value of 30 per cent (see figure 2.6).

Also included in figure 2.5 are the SEDs generated for the same chemical evolution model but adopting the two dust assumptions. Since the simple dust assumptions are normalised to the full CPM08 model for the solar neighbourhood at 13 Gyrs the SEDs at

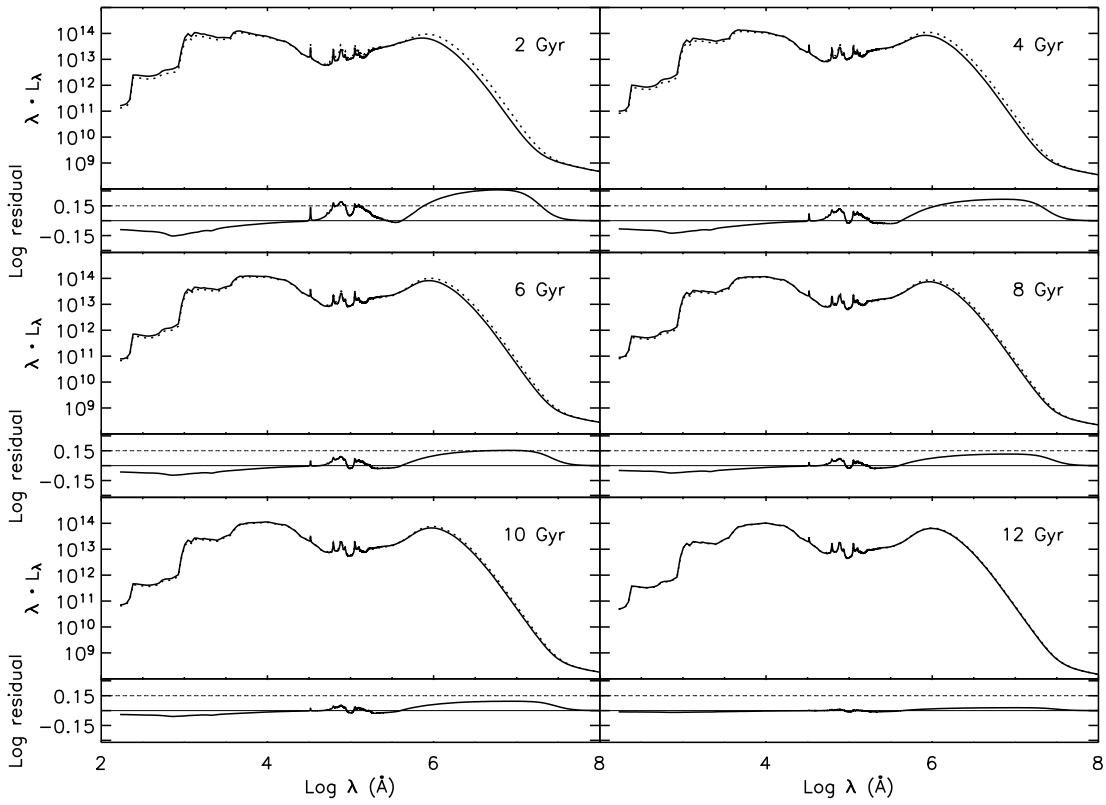

Figure 2.5: The evolution of the SED of the spiral galaxy. The larger six plots shows the SEDs at different times in the evolution of the galaxy (with units erg $s^{-1}(10^{30})$). The solid line shows the SEDs generated using the full CPM08 model, the dashed line the evolution adopting the simple dust model. The lower panels displays the log residual between the two models.

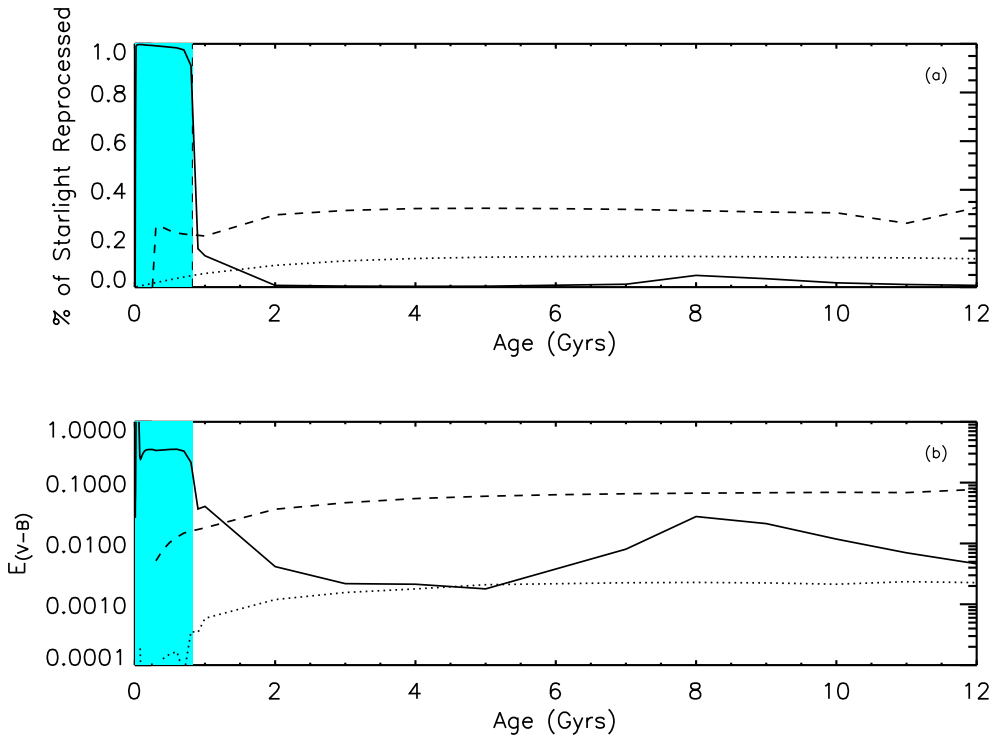

Figure 2.6: a) Fraction of stellar radiation dust reprocessed: Solid line - elliptical, dotted line - irregular, dashed line - spiral b) Evolution of extinction coefficient: Solid line - elliptical, dotted line - irregular, dashed line - spiral. The blue shaded area represents the age before the galactic wind starts in the elliptical model during which it is undergoing a period of extreme starformation

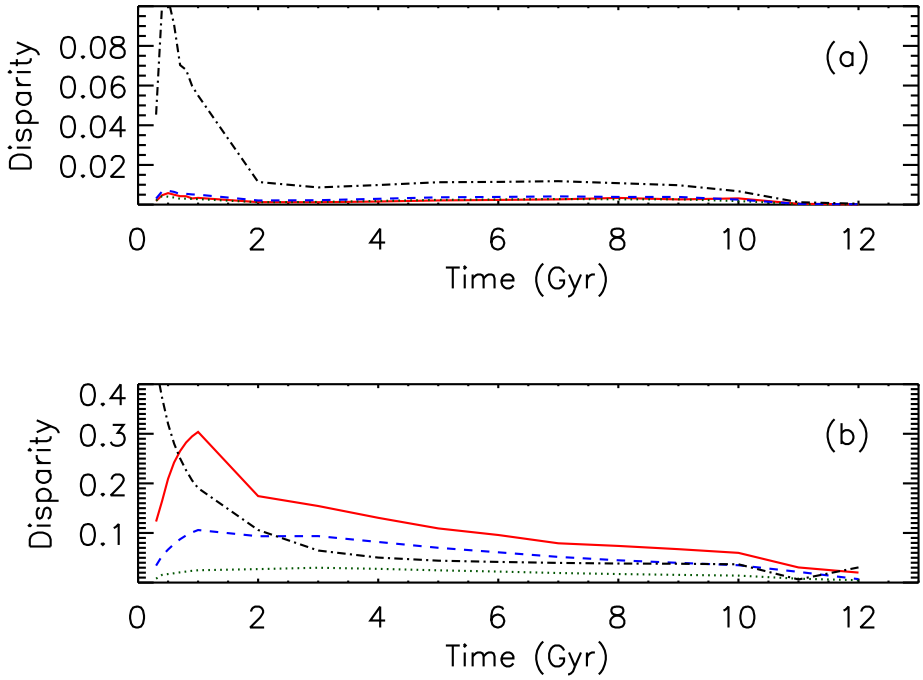

Figure 2.7: The residuals between the SEDs generated by the full spiral CPM08 model and SEDs generated by using the simplifications that (a) the chemical composition remains equal to the Milky Way values at all times, (b)the dust-to-gas ratio scales with the metallicity. Blue dashed line - UV, green dotted line - optical/NIR, Black dot/dashed line MIR, Red solid line - FIR. The disparity is given as the absolute mean log value of the residuals between the two models in the specified wavelength region

12 Gyrs are still in very close agreement. As the age of the galaxy decreases the residuals increase (figure 2.7) as the assumptions made for the dust-to-gas ratio and carbon over silicate ratios diverge from our theoretically calculated values.

Of the two simplifications the disparity introduced by assuming a dust-to-gas ratio dominate the residuals. Assuming a constant Milky Way chemical composition of the dust has little effect on the SED because after initial fluctuations during the first 2 Gyrs this ratio remains fairly constant, throughout the rest of its lifetime (figure 2.8a). Hence making the simplification that the chemical composition does not evolve with time will only lead to small differences in the SED (figure 2.7a) for the majority of the spiral galaxies life. At

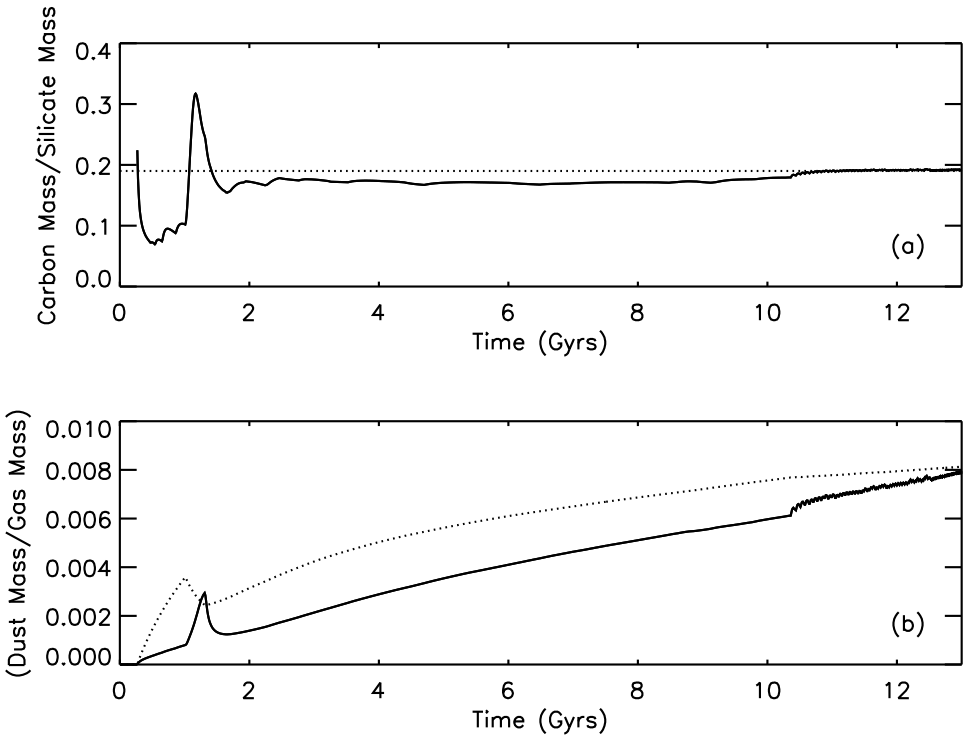

Figure 2.8: Spiral Galaxy: (a) Comparison between the value of the C/Si calculated by the full CPM08 ratio (solid line) with the constant value assumed if the chemical abundance remains identical to the present value for the solar neighbourhood (dotted line). (b) Comparison of the dust-to-gas ratio value calculated by the full CPM08 model (solid line) with the expected value if a dependence on the metallicity is assumed (dotted line).

early times the different chemical composition calculated mainly affects the MIR part of the SED due to the resulting differences in the abundance of PAHs.

The assumed dust-to-gas ratio however leads to a more significant disparity particularly when the galaxy is younger (figure 2.7b) since our model predicts a relationship between the dust-to-gas ratio and the metallicity which is not entirely linear (figure 2.8b). Therefore adopting this assumption will introduce disparities which largely increase as the age of the galaxy decreases. This assumption will result in too much dust in the galaxy and this will lead to an excess of reprocessing. The disparity will be most significant in the FIR part of the spectrum (figure 2.7b).

In this work only the chemical evolution in the solar neighbourhood has been

followed and the SED of the whole galaxy has been constructed by globalising the results. Although this has been shown to be a reasonable assumption for old spiral galaxies in the local universe, since the SEDs generated are representative of observations, it is unlikely to be valid at higher redshifts. The chemical evolution has two infall episodes; first the halo and the thick disc forms followed by the second phase in which the thin disc forms. So at early times the halo and thick disc will dominate the galaxies properties and the global properties could differ greatly from that of the solar neighborhood. The results for very young spiral galaxies (ages $\leq$ 1 Gyr) should therefore be taken with caution.

The CPM08 model and indeed all complete dust evolution models currently written only deal with the total mass of different elements contained in grains. As a result no information is contained regarding how these elements are combined to form grains and what size distribution these grains should have. Instead a composition and size distribution for the dust grains must be assumed. In previous works using GRASIL it has been usual to use the grain distribution population suggested in S98. In that paper both the observed extinction curves from the diffuse medium within the Milky Way and the observed galactic emission from dust was reproduced using a combination of graphite and silicate grains and PAH molecules.

Our spiral chemical and dust evolution model is designed to match observed properties of the solar neighbourhood and as a result it should also be capable of reproducing the observed galactic extinction and emission. Our model however predicts a slightly different ratio for the dust-to-gas ratio as well as a different graphite to silicate ratio than that used in S98. Therefore if we use the S98 size distribution in combination with the theoretical quantities of dust we have calculated the resultant extinction and emission properties will differ slightly from those observed.

No adequate dust model was found in the literature which could satisfactorily reproduce the observed extinction curves with the low value of 0.19 for the ratio of carbon to Silicon predicted by our model (for example see Zubko et al. 2004). Hence, for simplicity the S98 dust composition already included within the GRASIL model was used. A likely possibility is that existing dust models are tuned on low density environments (cirrus) while our C/Si value should refer to a galactic average.

2.4.2 Properties of Irregular Galaxies

Figure 2.9 shows the results for the theoretical SEDs generated at 12 Gyrs compared to the SEDs for all the magellanic type irregular galaxies of the SINGS sample. Although the irregular galaxies show some scatter in their SEDs the theoretical model manages to fit the average properties remarkably well. Also shown in the figure is the SED generated if the two dust simplifications are used. By using these simplifications quite a clear discrepancy between the two SEDs is introduced particularly in the IR and UV. Although still largely consistent with the observed SEDs there is a strong hint that the simplified dust treatment is leading to more dust reprocessing than that observed in the average galaxy in the sample. A common measure of the quantity of dust reprocessing in a galaxy is the observed IR/UV ratio (e.g. Dale 2007). Using the same formalism as Dale et al. (2007) and equation 4 from Dale & Helou (2002) the median Total IR to UV ratio was calculated for the irregular magellanic galaxies in the sample to be 0.22. This agrees well with the value of 0.21 calculated from the results of the full CPM08 model. For the simple dust model however a value of 0.67 was calculated implying that to much energy has been absorbed in the UV and emitted in the IR.

For the most part the disparity between the SED generated using the full dust treatment and that generated using the simplifications can be attributed to the assumption that the dust-to-gas ratio scales with metallicity (figure 2.10b). As figure 2.11b shows the theoretical values calculated by our model are much lower than those calculated from the Milky Way scaling relation, by approximately a factor of 6. This much lower dust to gas ratio can be mainly attributed to the absence of accretion in our irregular galaxy model which will results in smaller quantities of dust forming than would be expected following the common Milky Way metallicity scaling relation, where dust accretion is prevalent. Such a finding is consistent with the work of Galliano et al. (2003 & 2005) where dust masses were estimated for 4 local dwarf galaxies and for two (NGC 1569 and He 2-10) values for the dust-to-gas ratio lower by a factors 4-7 and 2-10 than expected were found and Hunt et al. (2005) and Walter et al. (2007) who estimated the dust masses in local dwarf galaxies and found values consistently smaller than expected.

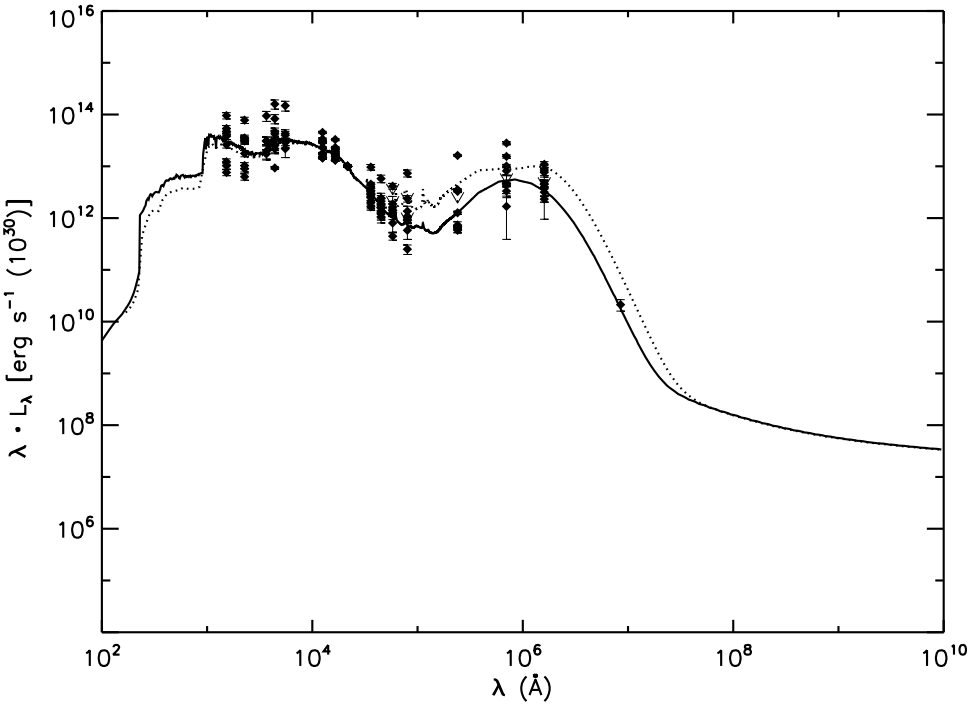

Figure 2.9: Comparison of theoretical irregular model at 12 Gyrs with SEDs of all irregular galaxies of magellanic type in the SINGS sample. Solid line - Full CPM08 model. Dotted line - simple dust model

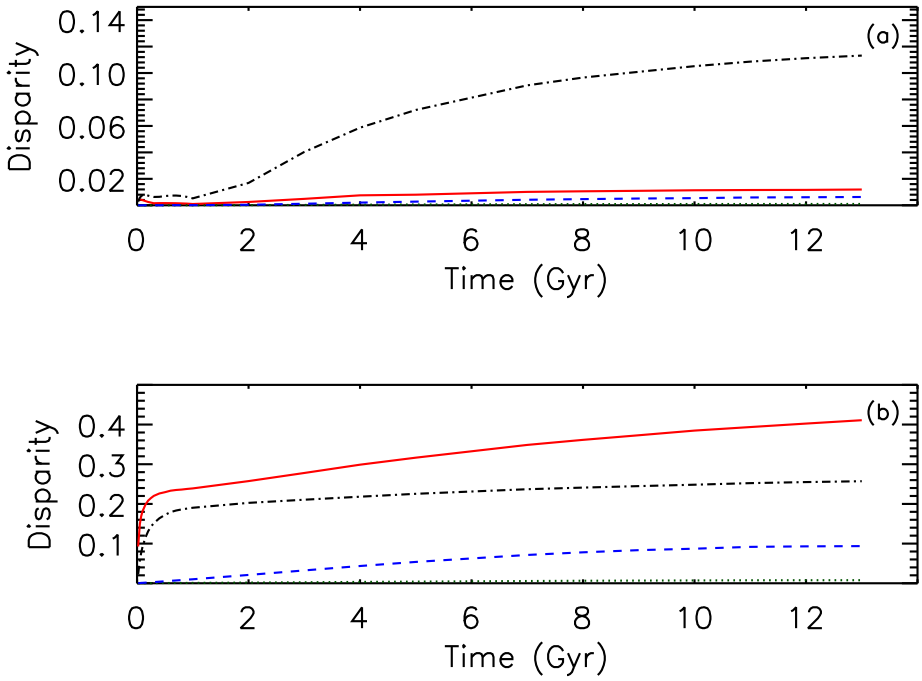

Figure 2.10: The residuals between the SEDs generated by the full irregular CPM08 model and SEDs generated by using the simplifications that (a) the chemical composition remains equal to the Milky Way values at all times, (b)the dust-to-gas ratio scales with the metallicity. Lines the same as in figure 2.7

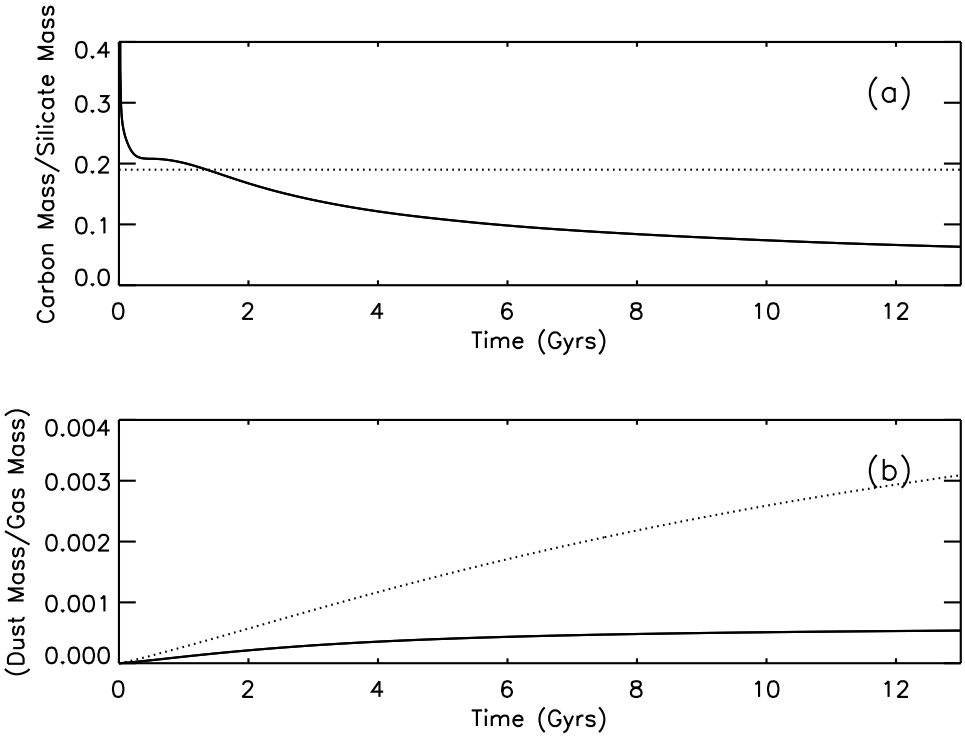

Figure 2.11: Irregular Galaxy: (a) Comparison between the value of the C/Si calculated by the full CPM08 ratio (solid line) with the constant value assumed if the chemical abundance remains identical to the present value for the solar neighbourhood (dotted line). (b) Comparison of the dust-to-gas ratio value calculated by the full CPM08 model (solid line) with the expected value if a dependence on the metallicity is assumed (dotted line).

Figure 2.11a shows that at ages greater than about 2 Gyrs the chemical composition calculated by the CPM08 model is significantly different from that calculated for the solar neighbourhood, resulting in a much lower C/Si ratio. Figure 2.10b shows that the main effect on the SED of the galaxy of this lower C/Si ratio will be in the MIR part of the spectra, with only a small effect at other wavelengths. The effect on the MIR of a change in the chemical composition needs to be treated with caution, since a major contributor to this part of the spectra are PAHs, whose evolution is not specifically followed by the CPM08 models (see § 2.3.3). The effect of the lower C/Si value predicted by CPM08 on the SED will largely be due to a reduction in the number of PAH molecules and therefore in the luminosity radiated in the PAH bands.

Although the treatment of the PAHs in this work is insufficient to put any strong constraint on the nature of the PAHs in the galaxies modelled, it is worth noting the relatively low abundance of C/Si predicted for the irregular galaxy, compared to that of the solar neighbourhood. This is interesting since it is in agreement with the striking observed correlation between the strength of PAH features and the metallicity of the galaxy (see e.g. Engelbracht et al. 2005; Madden et al. 2006; Wu et al. 2006; O'Halloran et al. 2006), with low metallicity galaxies, such as our theoretically modelled irregular galaxy, exhibiting very weak or no features. Several different explanations have been proposed for this correlation. These include the suggestion of more efficient PAH destructive mechanisms in lower metallicity galaxies (e.g. Galliano 2005; Madden et al. 2006) due to harder radiation and the paucity of dust. Alternatively, O'Halloran et al. (2006) proposed that the PAHs could be destroyed by numerous shocks observed in low metallicity systems. While it has also been shown by Galliano et al. (2008), that it is possible to explain the trend of PAH abundance with metallicity, using chemical evolution models. Starting from the summations that lower metallicity galaxies are on average younger than higher metallicity galaxies and that carbon dust and PAHs are predominantly produced in AGB stars which recycle their ejecta into the ISM after a relatively long period of time. It follows that the trend can be seen as a reflection of this delayed injection of carbon dust into the ISM by AGB stars, since younger systems will have had insufficient time to become enriched with PAHs. The CPM08 chemical evolution models used in this work puts forward a new suggestion since they show

that even in older low metallicity systems there is likely to be a lower abundance of carbon and therefore PAH molecules, a possibility which could explain or at least contribute to the observed trend.

The relatively lower value of C/Si predicted by the CPM08 model with respect to that predicted for the solar neighbourhood can be explained by examining the different production and destruction rates used in the two different environments. In the solar neighbourhood model, carbon is assumed to be destroyed with a higher efficiency than the silicates. This was chosen in order to explain the local dust abundance pattern (see CPM08), and is consistent with the fact that carbon has a condensation temperature lower than many silicates. However, the solar neighbourhood model also includes dust accretion, whose rate is assumed to be independent of the particular element. For this reason, the abundance pattern produced by the preferential destruction of certain elements is partially smoothed out by the non-differential accretion. In the irregular model, however, where dust accretion is absent, the higher destruction rate attributed to the carbon is not compensated in the same way, giving rise to the lower C/Si value.

A possible source of error in this work is the absence of an additional 'very cold grain' (VCG) component as proposed by Galliano et al. (2003 and 2004). In these papers a population of grains at very low temperatures were introduced in order to explain an excess in the emission in the sub-mm in the low metallicity galaxies observed. Such a component could be located at the centre of dense clouds (see e.g. Galliano et al. 2003) or in the galaxies outskirts where the radiation field is weak (see e.g. Draine et al. 2007). Galliano et al. (2003 and 2005) estimated that for four low metallicity irregular galaxies between 40 and 80 per cent of the total dust mass is in the form of VCGs. Such a dust component is not currently included in our models and if confirmed by additional sub-mm observations the inclusion of such a large cold dust grain population should be investigated. However any effect is likely to be slight. For the irregular galaxies over 80 per cent of the reprocessing is taking place within the molecular clouds, heated by the young stars (As opposed to about 25 per cent in the spiral model). The emission of which is characterised only by the geometry and dust-to-gas ratio of the molecular clouds and would therefore be unaffected by a population of VSGs. If a substantial proportion of the rest of the dust takes the form

of VCGs the result would be a reduction in the amount of other larger sizes of dust grain in the cirrus. In our irregular model the cirrus component only has a small observed effect on the SED at wavelengths longer than the peak IR wavelength. Therefore any effect will be slight and will probably result in a slight decrease in emission in the very FIR and an increase in the sub-mm, where the VCGs will emit.

The evolution of the SED of irregular galaxies is shown in figure 2.12. The quiescent low star formation rate leads to SEDs which only slightly evolve with time. The mass of dust present in the galaxy initially increases rapidly until a time $\sim$ 1 Gyrs is reached at which point it begins to plateau (see figure 2.3c). The fraction of reprocessed light in the galaxy follows suit, rising rapidly to a value of $\sim$ 15 per cent and then remains fairly constant throughout its lifetime. A value which is one half of the predicted light reprocessed in spiral galaxies.

As figure 2.10 shows the disparity between the SEDs generated using the simplifications and the full dust treatment actually decrease gradually as the galaxy gets younger with the difference from introducing the dust-to-gas scaling relation always dominating that from assuming a constant chemical composition. With the largest effect always in the IR with a very small effect in the optical and NIR part of the spectrum.

The dust size distribution in irregular galaxies is likely to differ from that of the Milky Way, (e.g. Galliano et al. 2005). This is highlighted by the fact that extinction curves have been observed in both the small magellanic cloud (SMC) and large magellanic cloud and have been found to differ from that of the Milky Way. The SMC extinction curve is of particular interest since it is an irregular dwarf galaxy with a substantially lower metallicity than the Milky Way and should represent a dust environment similar to our theoretical irregular model. The predicted extinction curve for the mass and composition of dust predicted by our irregular model has been compared to the observed SMC curve in order to constrain a dust grain size distribution. As figure 2.13 shows just by adopting the chemical composition predicted by the full CPM08 model even with the size distribution already calculated to match the properties of the Milky Way a reasonable fit is obtained to the extinction curve, so the different chemical composition alone can go some way to explaining the observed extinction curve. By fine tuning the parameters governing the size

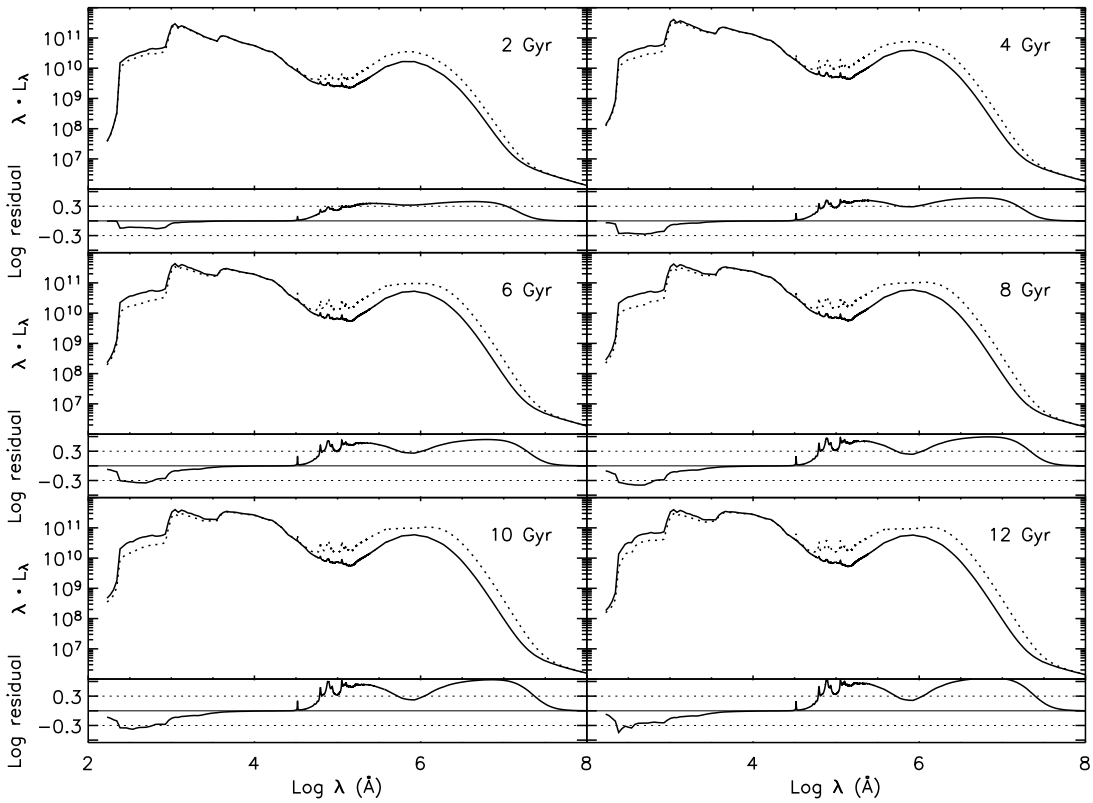

Figure 2.12: The evolution of the SED of the irregular galaxy, panels the same as for figure 2.5

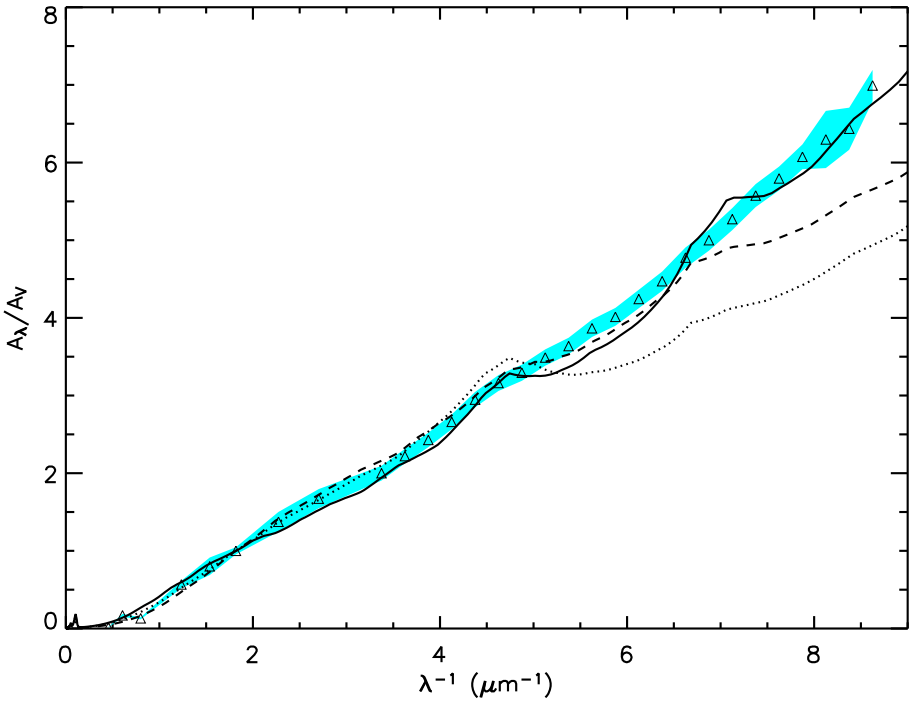

Figure 2.13: Best fit dust composition to SMC extinction curve. Solid line - full CPM08 model with optimised size distribution; dashed line - full CPM08 with S98 size distribution; dotted line - Milky Way chemical composition, S98 size distribution . The blue shaded area shows the associated uncertainty in the observed extinction curve.

distribution in equation 1.3 an improved fit can be obtained, as shown in the figure. The values of the best fit parameters are shown in table 2.2.

Figure 2.14 displays a comparison of the SEDs for the full model adopting the size distribution constrained using the SMC extinction curve to the SEDs for the full model using the standard Milky Way derived size distribution. It shows that the difference is small at all times, largely because the difference in the two size distributions is small.

2.4.3 Properties of Elliptical Galaxies

In our elliptical galaxy formation scenario there are two distinct stages. An initial rapid collapse of a sphere of primordial gas leading to intense star formation and a second

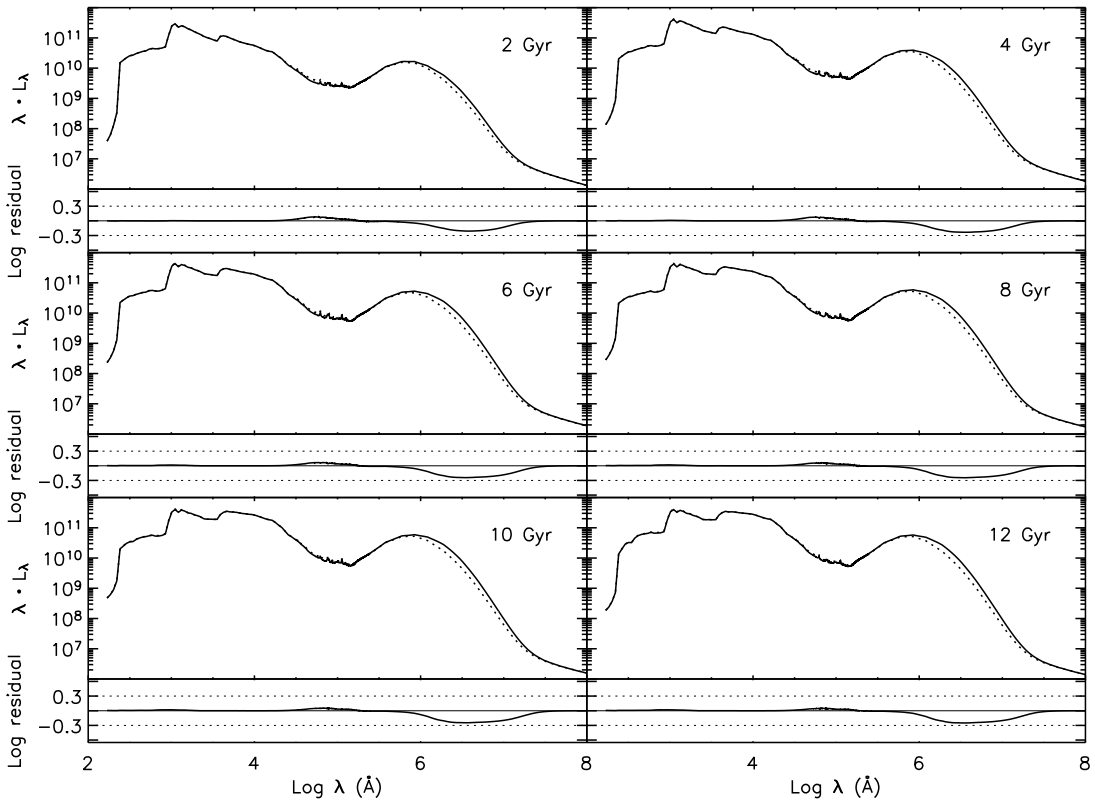

Figure 2.14: The effect of the SMC size distribution on evolution of the SED of the irregular galaxy, solid line full CPM08 model with MW size distribution, dashed line - full CPM08 model with SMC size distribution

quiescent stage where the star formation has stopped as almost all of the gas is blown away by galactic winds. These two stages will be discussed separately. Unless stated all results shown are for the elliptical model with a final stellar mass of $10^{11} M_{\odot}$.

Starbursting phase - High redshift

The evolution of the SED of our elliptical model during the starbursting phase is shown in figure 2.15. Initially all the stars will be located within their birth clouds (molecular clouds) however since the dust mass is initially negligible the SED at these very early times will have the form of just the bare stellar component. The molecular clouds will soon become rapidly enriched with dust due to dust production in type II SNe and as a result the reprocessing will rise quickly, almost to 100 per cent after 0.005 Gyrs (figure 2.6). As the age of the galaxies increase more stars will have had time to escape from their molecular clouds and as a result will be radiating in the more diffuse cirrus hence the gradual decrease in reprocessing as observed in the figure. The small amount of PAH emission seen in the SEDs of figure 2.15 is as a result of the large proportion of dust emission coming from the molecular clouds. Due to the suppression of the abundance of PAHs in these environments they will consequentially produce little PAH emission. After the onset of the galactic winds at 0.7 Gyr the majority of the dust is blown out of the galaxy so the amount of reprocessing drops, at same the time the star formation is stopped and the galaxy enters the passively evolving stage.

Figure 2.16 shows the effect that the two simplifications will have on the SEDs. Of the two, adopting the assumption that the dust-to-gas ratio will scale with the metallicity will have the biggest effect. This is because as figure 2.17 shows that although such a relationship does hold for these young galaxies initially (ages < 0.3 Gyrs) the dust-to-gas value calculated by the model soon diverges from the expected value based on the metallicity and as a result using this simplifications leads to large disparities in the SEDs.

Assuming a milky way chemical composition for the dust however has little effect on the SEDs at early times. This is because as figure 2.17 shows the chemical composition at least initially is remarkably similar to the value of 0.19 calculated for the solar neighbourhood. As the burst progresses the C/Si begins to drop leading to small differences

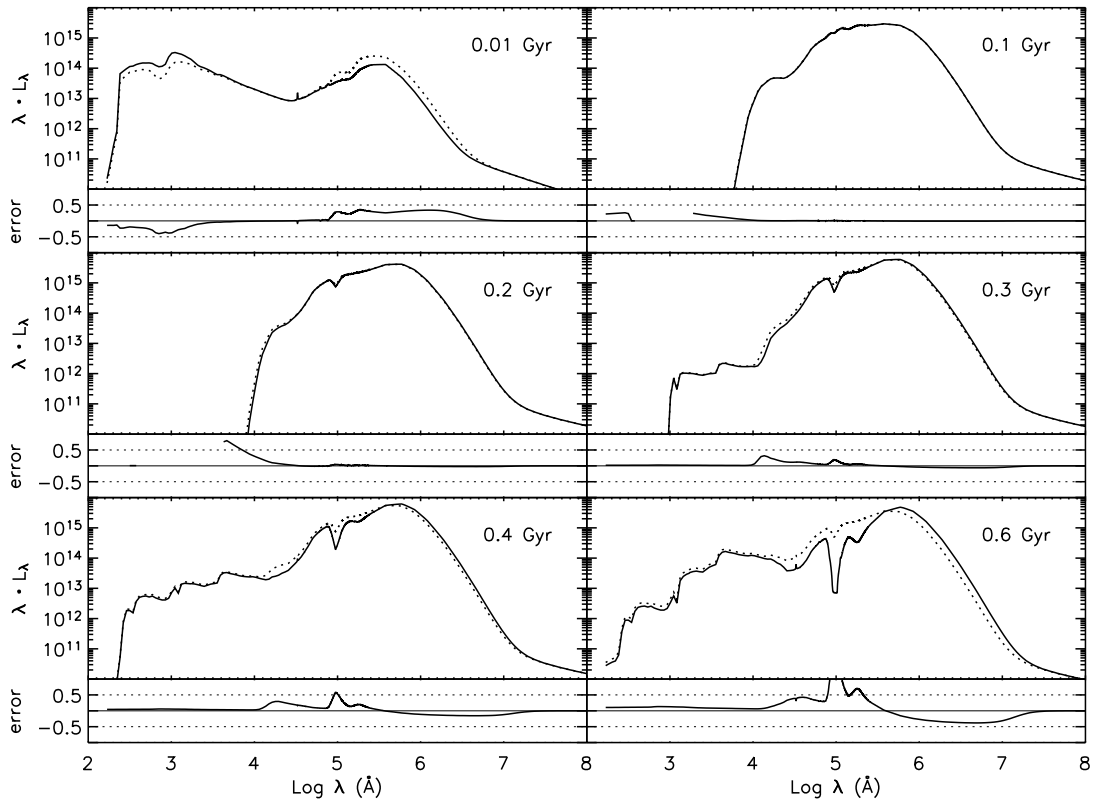

Figure 2.15: The high redshift evolution of the SED of the elliptical galaxy, panels the same as for figure 2.5

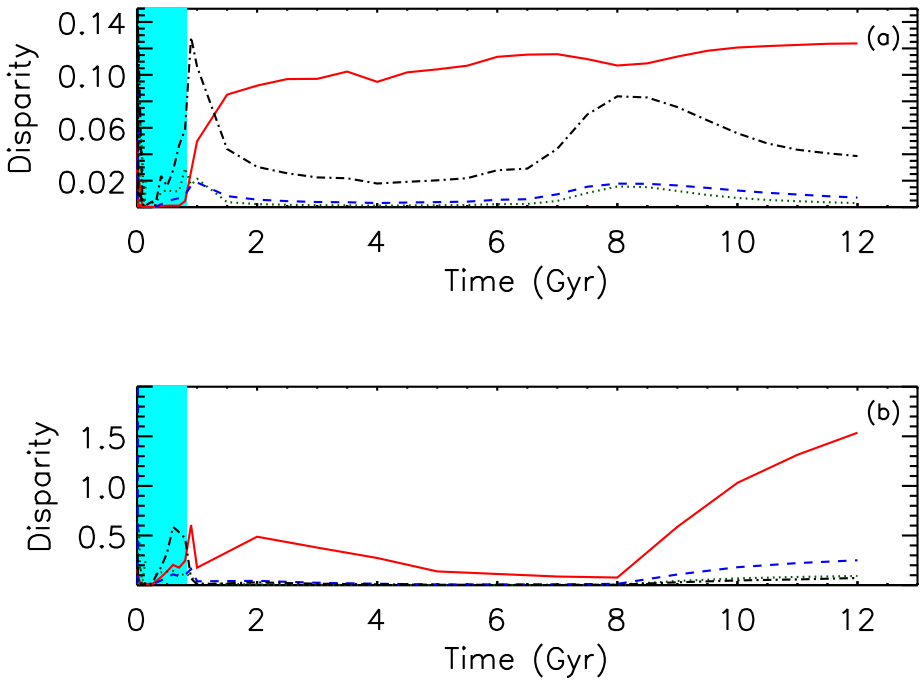

Figure 2.16: The residuals between the SEDs generated by the full elliptical CPM08 model and SEDs generated by using the simplifications that (a) the chemical composition remains equal to the Milky Way values at all times, (b)the dust-to-gas ratio scales with the metallicity. Lines the same as in figure 2.7. The blue shaded area represents the age before the galactic wind starts in the elliptical model during which it is undergoing a period of extreme starformation

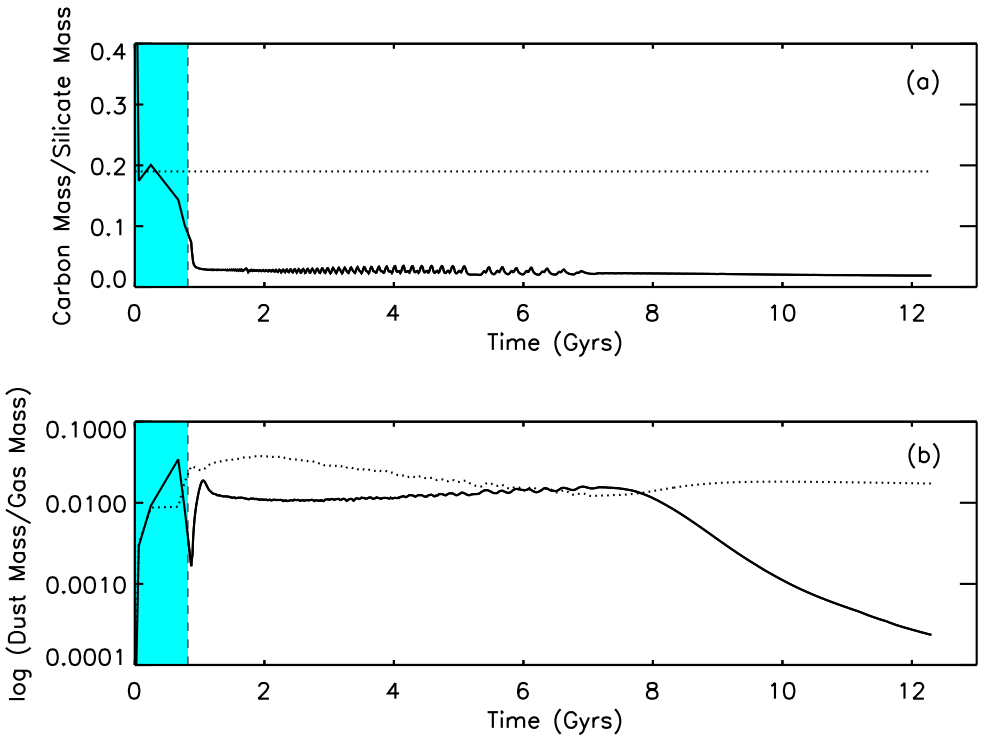

Figure 2.17: Elliptical Galaxy: (a) Comparison between the value of the C/Si calculated by the full CPM08 ratio (solid line) with the constant value assumed if the chemical abundance remains identical to the present value for the solar neighbourhood (dotted line). (b) Comparison of the dust-to-gas ratio value calculated by the full CPM08 model (solid line) with the expected value if a dependence on the metallicity is assumed (dotted line). The blue shaded area represents the age before the galactic wind starts in the elliptical model during which it is undergoing a period of extreme starformation

between the SEDs of the full CPM08 model and the simple dust model (see figure 2.16b).

Although the model calculates that the chemical composition of the total dust component is likely to be quite similar to that of the solar neighbourhood throughout the burst it does not necessarily follow that the individual grains will be of the same composition and have the same size distributions as that observed locally. In the local universe much of the dust is thought to be produced in the stellar winds of low and intermediate mass stars. However in young galaxies at high redshift with ages less than 1 Gyr such stars would not have had sufficient time to evolve to this stage, instead the dust will be predominantly produced in SNe, for detailed information of the relative production rates of the various mechanisms see figures 2 and 6 in CPM08. Hence the dust properties in these young galaxies is thought to be very different to that observed in the local universe in the Milky Way and in the SMC.

One possible tool for the study of dust in the high redshift universe is QSOs. According to recent models of QSO-galaxy co-evolution (e.g. Granato et al. 2004 and Di Matteo et al. 2005) during the early stages of galaxy and black hole growth the AGN is embedded in gas and dust and is therefore difficult to identify as an QSO, however after the onset of galactic winds because large quantities of dust and gas will be swept away the QSO can be observed. The properties of observed QSOs should therefore be predicted by our elliptical model at times shortly after the onset of the galactic wind. Maiolino et al. (2006) showed that the chemical abundances observed in QSOs best match the chemical abundances calculated for our giant $10^{12} M_{\odot}$ elliptical model at times later than 0.5 Gyrs corresponding to the epoch just after the onset of the galactic winds supporting this theory. By studying the SEDs of QSOs it has been possible to infer extinction curves for these objects and by studying these observed curves it should be possible to constrain a size distribution for our young elliptical galaxies.

Maiolino et al. (2004) calculated an extinction curve for a high redshift QSO, SDSSJ1048+46 at a redshift of z=6.193 and found that the extinction curve differs greatly from the extinction curves observed at low redshift. The observed extinction curve has been compared to the extinction curve predicted by several models which have been written to predict the size distribution of dust from SNe including, Bianchi & Schneider (2007) and

Nozawa et al. (2007). These size distributions have been found to be consistent with the observed QSO extinction curve, leading to the conclusion that the dust observed in the extremely high redshift objects could indeed be dominated by SNe dust. The processes involved in the formation of dust in SNe is complicated and is far from being completely understood. Indeed the size distributions predicted by Nozawa et al. (2007) and Bianchi & Schneider (2007) differ substantially from each other. In addition both papers only consider the production and destruction of dust in SNe, neither follow the accretion and destruction of the SNe remnants in the ISM as well as that by the galactic winds.

In this work starting from the dust masses calculated by the CPM08 $10^{12} M_{\odot}$ elliptical model, at a galactic age of 0.5 Gyr, the parameters in equation 1.3 which correspond to the best fit to the Maiolino et al. (2004) extinction curve at Z$\sim$6 have been calculated. The resultant extinction curve is shown in (figure 2.18). The best fit parameters are shown in table 2.2.

Figure 2.19 shows the effect that adopting this size distribution will have on the SEDs of elliptical galaxies during their starburst phase. The SEDs generated vary substantially from those generated using the Milky Way size distribution particularly in the NIR and MIR.

SCUBA galaxies

The theoretical SEDs for the $10^{11} M_{\odot}$ young elliptical galaxies are compared to SCUBA galaxies at high redshifts. These galaxies have been found to be dust enshrouded sources with very high star formation rates. It is believed that these SCUBA galaxies could represent the birth of giant elliptical galaxies (Lilly et al. 1999, Eales et al. 2000) and should therefore correspond to the starbursting phase of our elliptical models. The data used is from the SHADES survey of the SXDF field (Clements et al. 2008). This survey is ideal for the purposes of this work since it has a good photometric coverage with observations from the optical Suburu / XMM-Newton field Deep Field (SXDF) (*B*, *V*, *R i'* and *z'*), Spitzer (IRAC 3.6, 4.5, 5.8, 9 μm and MIPs 24, 70 and 160 μm) and SCUBA. Only the galaxies with the highest redshift from the sample were used, namely galaxies which were found by Clements et al. (2008) to have a photometric redshift greater than two. In total these galaxies numbered thirteen.

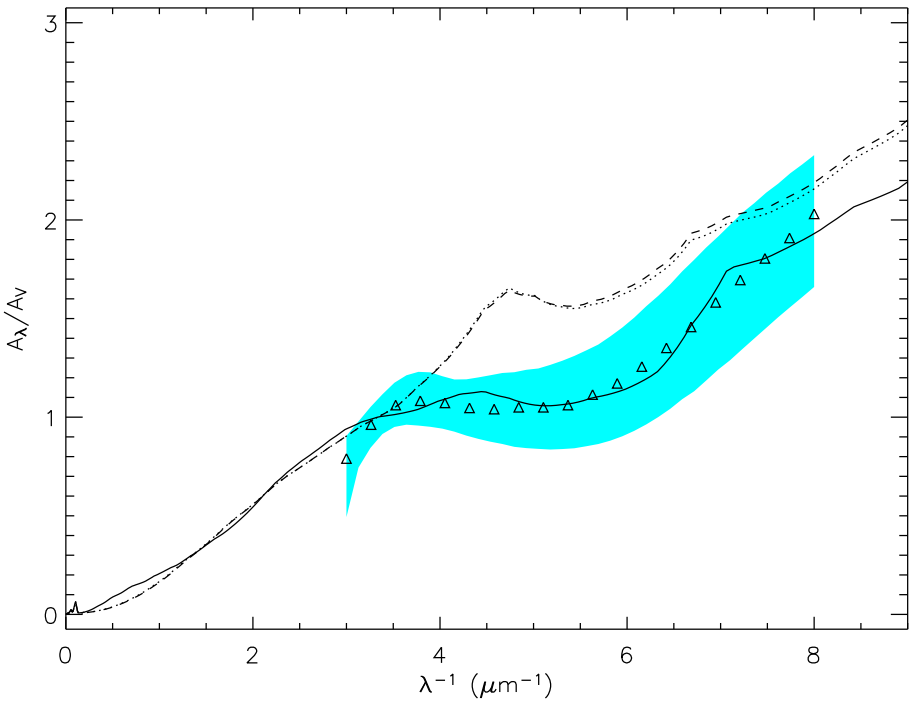

Figure 2.18: Best fit dust composition to the SDSS 1048 +46 quasar extinction curve. Solid line - full CPM08 model with optimised size distribution; dashed line - full CPM08 with S98 size distribution; dotted line - Milky Way chemical composition, S98 size distribution. The blue shaded area shows the associated uncertainty in the observed extinction curve.

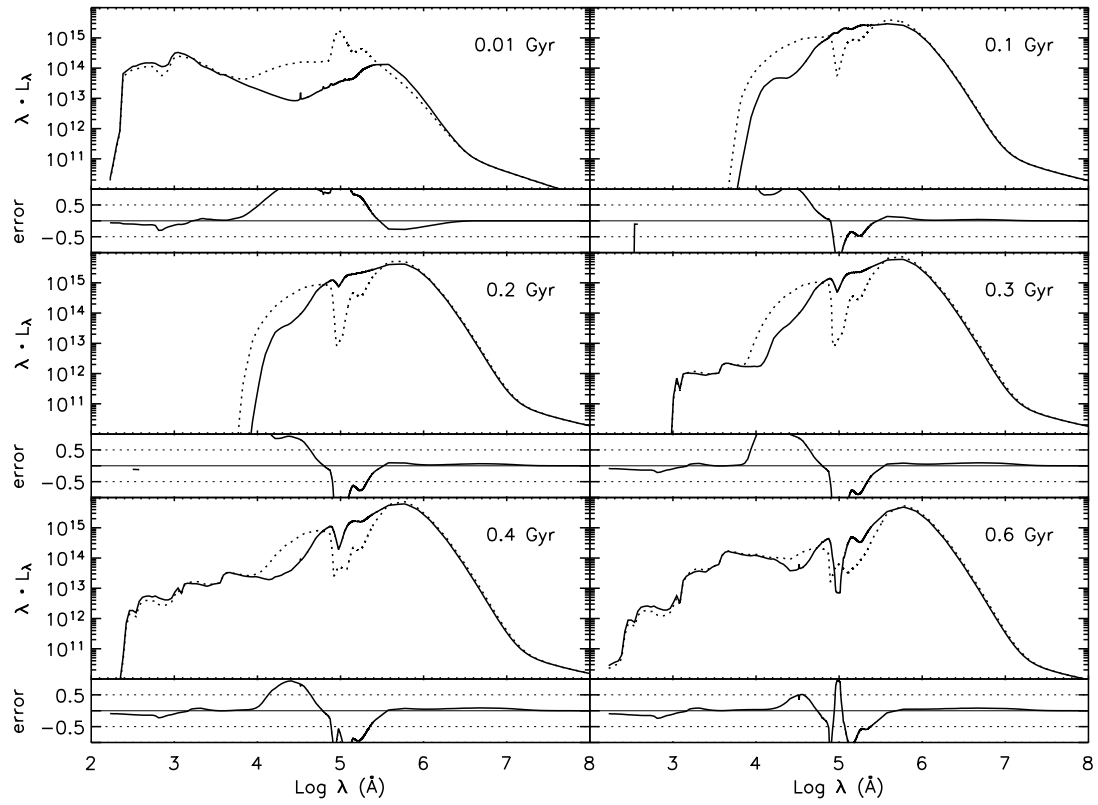

Figure 2.19: The effect of the quasar size distribution on evolution of the SED of the young elliptical galaxy, solid line full CPM08 model with MW size distribution, dashed line - full CPM08 model with the dust consistent with the z$\sim$ 6 QSO.

Figure 2.20 shows that for four of the observed galaxies in the SHADES dataset our model was able to match the general shape of the SED and the observed amount of reprocessing. The average age of the best fitting full CPM08 models for the four galaxies shown is 0.55 Gyrs. At such an age the theoretical model will still have ongoing star formation. Because only one star formation history has been followed and no parameters varied perfect matches could not be expected to all observed galaxies. However, as shown, even with this one simple star formation history, the observed SEDs of four out of the thirteen galaxies investigated in this work could be reasonably reproduced. This suggests that the rationale of treating these galaxies as obscured starbursts with a dust mass calculated by the CPM08 model is consistent with the observations. Also shown in the figure are the spectra for the simple dust model and for the full dust model with the dust composition calculated in order to fit the QSO SDSSJ1048+46. Although the SEDs generated using the full model with the size distribution consistent with the z$\sim$6 QSO diverge from that of the full CPM08 model significantly, the theoretical SEDs are still largely consistent with the data. The SEDs generated by the simple dust model on the other hand lead to slightly worse fits, although a much more thorough analysis is needed to come to a more definite conclusion.

Giant post-starbusrt galaxies at high redshift

The theoretical SEDs calculated for young elliptical galaxies are compared to massive galaxies which have been observed to be already highly evolved at high redshifts (Wiklind et al. 2008). Since these galaxies are likely to be massive the giant $10^{12} M_{\odot}$ elliptical galaxy will be used in the fits. The galaxies in the data set have been selected by Wiklind et al. (2008), so that they are dominated by a stellar population older than $\sim$ 100 Myr and situated at z $\geq$ 5. They should therefore correspond to a later stage in the evolution of our giant elliptical galaxy model, the post starburst stage. Data points are available in the optical (ACS - B, V, i, z) NIR (VLT/ISAAC - J H K_s) - MIR, deep imaging with the Spitzer Space Telescope with IRAC (3.6, 4.5, 5.7 and 8.0 μm) and MIPS (24 μm). For the chi-squared fitting the point at 24 μm was not included since emission in this region could be dominated by an AGN.

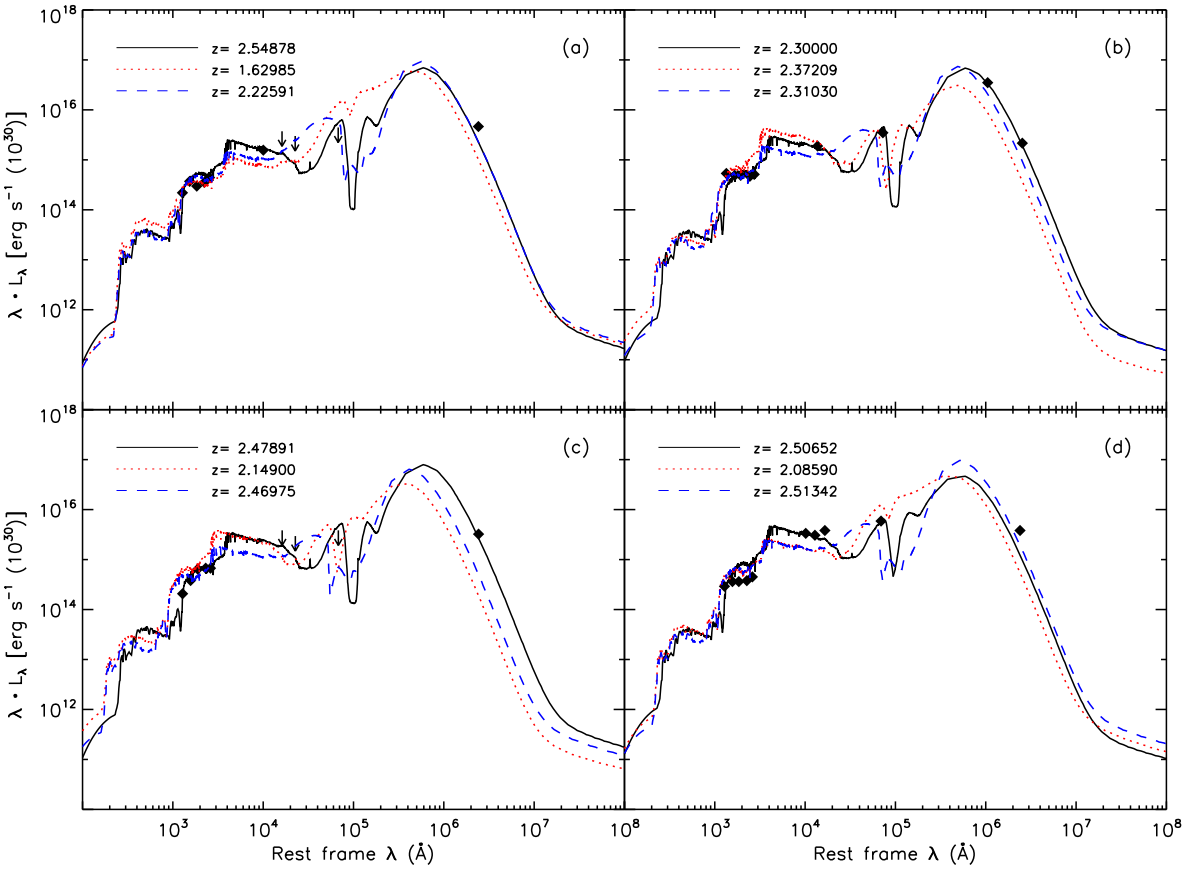

Figure 2.20: Comparison of $10^{11} M_{\odot}$ theoretical elliptical model with the SED of SCUBA galaxies: a) SHADES-SXDF 10, b) SHADES-SXDF 11, c) SHADES-SXDF 12, d) SHADES-SXDF 7. Solid line - full CPM08 model. Dotted line - simple dust model. Dashed line - full CPM08 model with dust consistent with the z∼6 QSO. The rest frame wavelength is correct for the redshift calculated for the full CPM08 model. The abscissa values for the curves for the simple dust model and the full CPM08 model with dust consistent with the z∼6 QSO were appropriately re-scaled. The redshift values calculated by Clements et al. (2008) are: z= 2.08 for SHADES-SXDF 10, z=2.30 for SHADES-SXDF 11, z=3.07 SHADES-SXDF 12, z=2.31 SHADES-SXDF 7

Many of the observed galaxies could be well matched by our theoretical model and figure 2.21 shows good fits to four of the galaxies in the sample. The fits for the full CPM08, the simple dust model and the full dust model with the dust composition calculated in order to fit the QSO SDSSJ1048+46 are all good. The theoretical SEDs diverge from each other mostly in the rest frame FIR and since no observations exist for this part of the spectrum the difference in fits in the SEDs is slight. The average age of the best fitting full CPM08 models for the four galaxies shown is 0.61 Gyrs. At such an age our giant elliptical model corresponds to a post starbursting system with no current star formation. It should be noted that because only one star-formation history was followed in this work our calculated value for the stellar ages of the galaxies should be taken as an indication of one possible formation scenario not as an actual value.

For several of the galaxies in the sample, intriguingly the observed MIPS flux at 24μm far exceeds the flux predicted by our model, for example BBG 3348. This galaxy has been observed in the x-ray with a luminosity of $3 \times 10^{43} erg\ s^{-1}$ and it is therefore plausible that the observed MIPS flux could have a contribution from an obscured AGN. Such a source could explain the higher flux observed in this band but would have a minimal impact on the part of the SED covered by the ACS/ISAAC/IRAC bands (see e.g. Mobasher 2005) and would therefore not effect the presented SED fit in this region.

Figure 2.22, however, shows an alternative formation scenario for this galaxy, in which the predicted SED of the $10^{11} M_{\odot}$ model is normalised and compared to the observed SED. The best fit model has been found to have a stellar age of 0.6 Gyr, the same age as that calculated for the $10^{12} M_{\odot}$ model. As can be seen from the fit, the MIPS 24μm flux is predicted by the model without the need of an obscured AGN. In this $10^{11} M_{\odot}$ model, star formation is still ongoing at such an age. Due to the nature of the dust model used, this young star formation will be entirely obscured within dense molecular clouds so will only contribute to the flux in the rest frame MIR and FIR. The older stars that have been able to escape the molecular clouds however will be only slightly absorbed due to the less dense cirrus producing a similar SED in the optical and NIR as the $10^{12} M_{\odot}$ model described above.

Both scenarios described, obscured starburst or a passive galaxy with an AGN

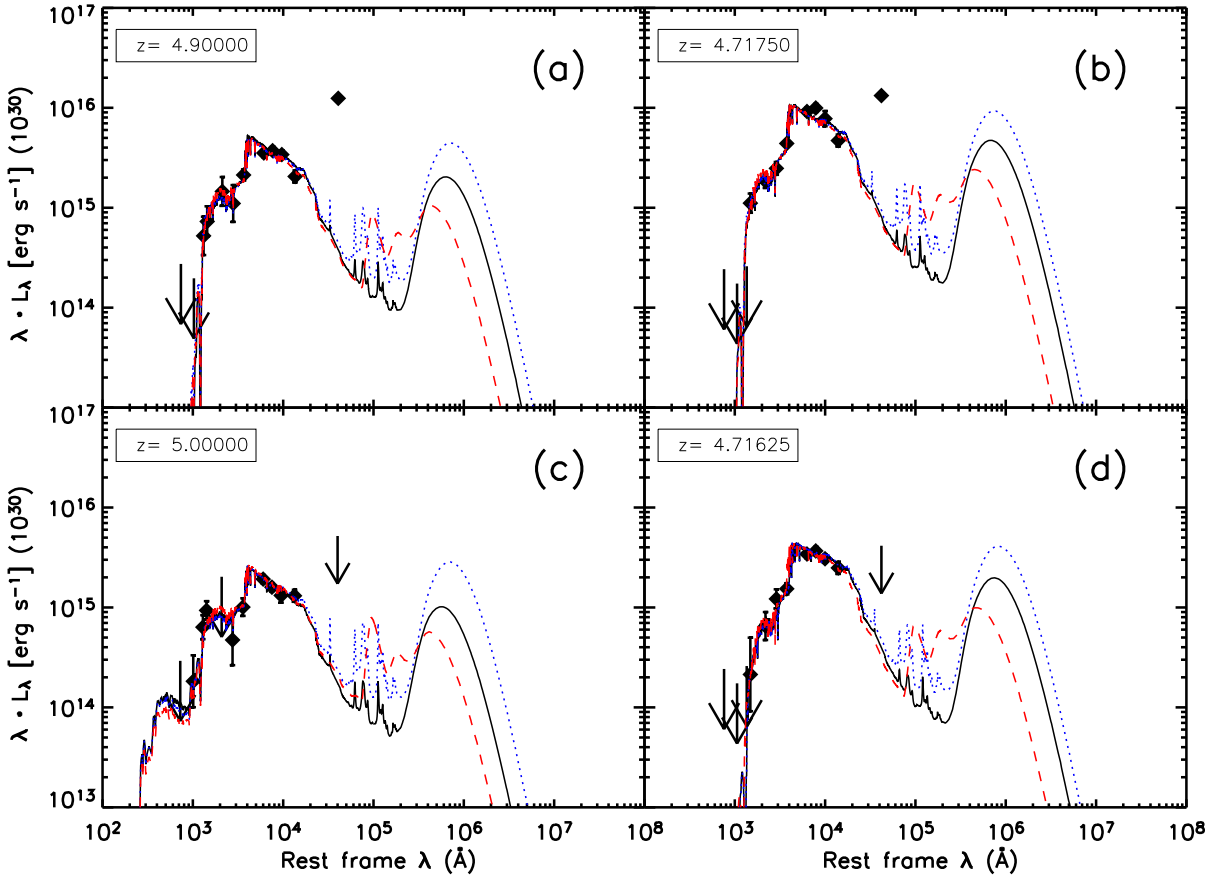

Figure 2.21: Comparison of the $10^{12} M_{\odot}$ theoretical elliptical model with the SED of balmer break galaxies: a) BBG 2910, b) BBG 3348, c) BBG 3361, d) BBG 4071. Black solid line - full CPM08 model. Blue dotted line - simple dust model. Red dashed line - full CPM08 model with dust consistent with the z∼6 QSO. The rest frame wavelength is correct for the redshift calculated for the full CPM08 model, the value given in the top left corner of the panel. In all cases the redshift values were the same for the two other models, except for BBG 4071, where a redshift of 4.34875 was calculated for the simple dust model, the abscissa values for the curve were appropriately re-scaled. The redshift values calculated by Wiklind et al.(2008) are: z=4.9 for BBG 2910, z=5.1 for BBG 3348, z=5.0 for BBG 3361 and z=5.0 for BBG 4071.

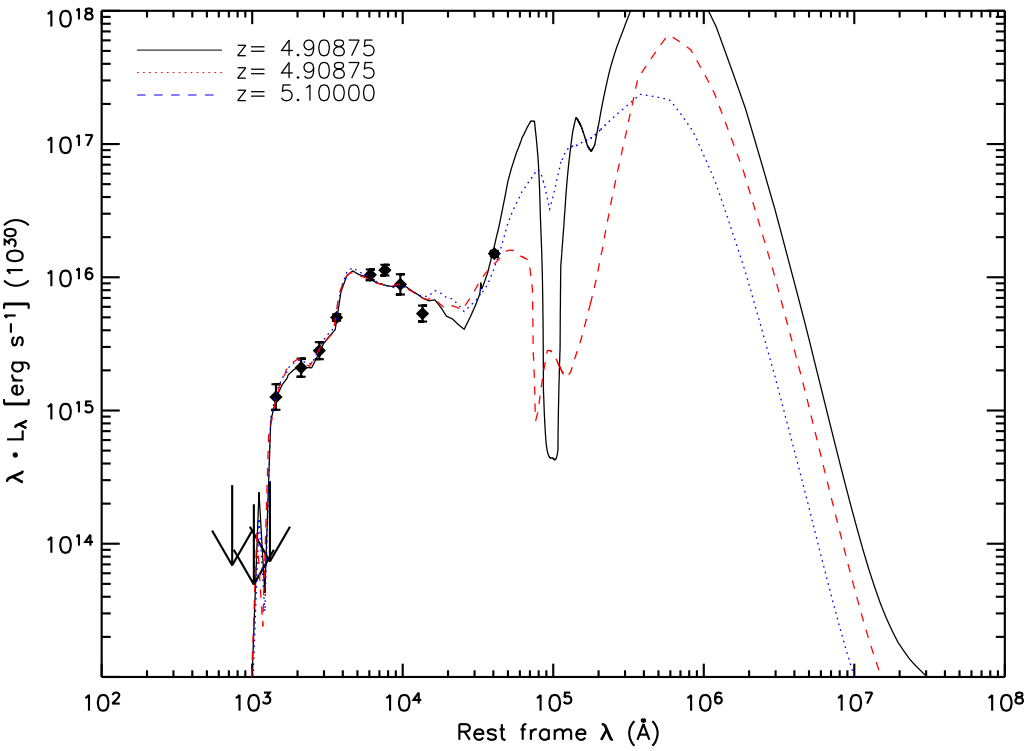

Figure 2.22: Comparison of the $10^{11} M_{\odot}$ theoretical model to galaxy BBG 3348 from the Wiklund sample. Dotted line - simple dust model. Dashed line - full CPM08 model with dust consistent with the z∼6 QSO. The rest frame wavelength is correct for the redshift calculated for the full CPM08 model. The abscissa values for the curves for the simple dust model and the full CPM08 model with dust consistent with the z∼6 QSO were appropriately re-scaled. Wiklind et al. (2008) calculated a redshift value of z=5.0

are equally consistent with the data. Longer wavelength observations would be required to discriminate between them.

Quiescent stage- low redshift

Figure 2.23 shows the result for the theoretical SED of the elliptical model generated at 12 Gyrs compared to the SEDs of the four 'passive' local elliptical galaxies from the SINGS sample. The SED generated by the model with the full dust evolution matches the observations well. Elliptical galaxies display fairly homogeneous optical colours, a trend reflected in the observed galaxies in figure 2.23, which have almost identical SEDs from the optical to the NIR. The SED in this region is reproduced well by our full theoretical model and also the simple dust model. The four galaxies though, show larger scatter in the FIR and in the UV.

Although there is much scatter in the observed FIR bump, probably due to a differing dust content, the full CPM08 model predicts FIR emission which agrees well with the average of the observed points. It can therefore be thought of as having a dust content consistent with this sample. However, when the simple dust model using the two simple dust assumptions is used, SEDs are generated which significantly overestimate the amount of FIR observed. Presumably because of the larger dust content present, due to the assumption that the dust-to-gas ratio scales with the metallicity (see figure 2.17b). In this work the assumption has been introduced that the dust component is more extended than that of the stellar component with a scalelength twice as large (see § 2.3.1). To check the robustness of our results on this assumption the SED of the elliptical model at 12 Gyr with a scalelength of the dust equal to that of the stellar component was calculated. This is also shown in figure 2.23 and it can be seen that although this assumption does have a noticeable effect on the SED the fit for the full CPM08 model is still consistent with the observations while the simple dust model stills over predicts the emission in the FIR.

Out of the four 'passive' elliptical galaxies in the sample all four have observations in the NUV and three have observed points in the FUV. Although the galaxies do show a small amount of scatter in this region the theoretical model is able to reproduce a UV-upturn which is consistent with the average points. The UV scatter too could be partially

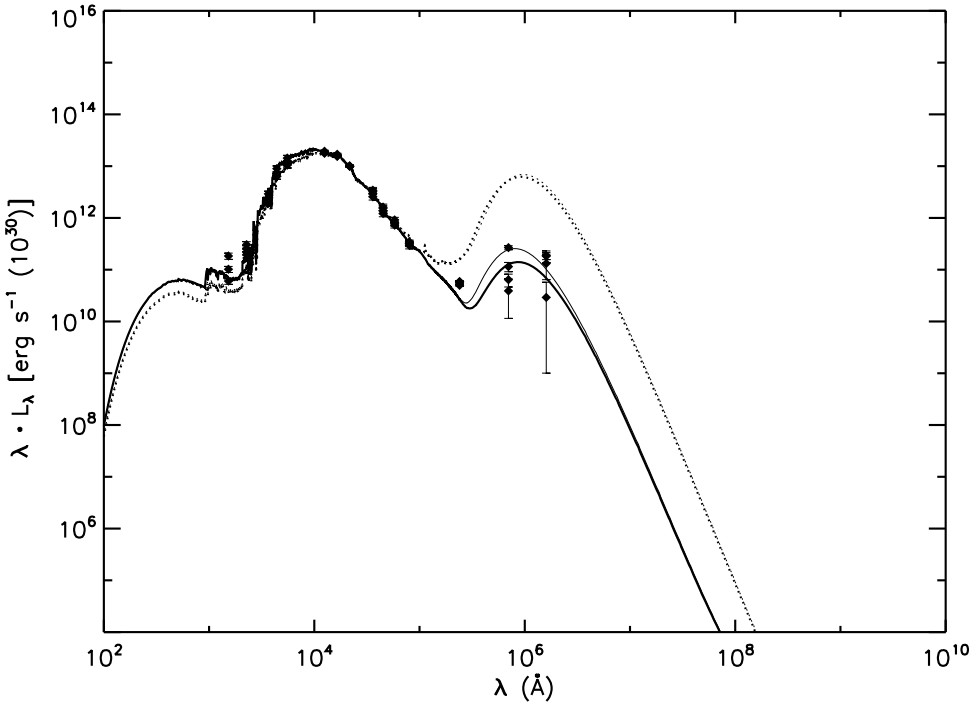

Figure 2.23: Comparison of theoretical elliptical model at 12 Gyrs with an average SED taken from four elliptical galaxies of the SINGS sample. Solid line - Full CPM08 model; dotted line - simple dust model. The thick line is for a scalelength of dust twice as large as that of the stellar component while the thin line is for equal scalengths (for the simple dust model the thin and thick lines are almost identical).

explained by differing amounts of extinction due to different dust contents. Indeed the simple dust model seems to under-predict the luminosity in the FUV, presumably because of the greater dust content present. However, it has also been claimed by several authors (e.g. Kaviraj et al. 2007) that the range of UV colours observed in different early type galaxies, could be due to a small amount of recent star formation ($1\% - 3\%$) in a large proportion of galaxies. This however is beyond the scope of the present work.

The theoretical evolution of the SED of the elliptical galaxy is shown in figure 2.24. Young stars are the main contributors to the UV so since there is no star formation the elliptical galaxies are weak in the UV. The amount of reprocessing in the galaxy (figure 2.6) is always small, at all times less than 5% and follows the mass of dust present in the galaxy (figure 2.3b) so it peaks at ~ 8 Gyrs and then declines due to destruction from the x-rays emitted by the hot gas.

Figure 2.16 shows that of the two simplifications the largest effect on the SEDs, comes from assuming the dependence of the dust-to-gas ratio on the metallicity, which will lead to large disparities in the SED. This is because this assumption leads to large differences in the dust to gas ratio with the results obtained from the full CPM08 model (see figure 2.17b). As figure 2.16 shows the disparity will be largest impact in the FIR.

2.5 Implications of this Work

In this work only one likely chemical and dust evolution model, with one star-formation history, has been followed for each morphological type of galaxy based on average properties of the galaxy type as a whole. It is therefore not possible to prove conclusively the accuracy of the models, since it is unlikely that they will match exactly the SED of any one specific galaxy. However, since the chemical-evolution models are designed to match average properties, the generated SEDs would be expected to match the general appearance of many galaxies of the specific type and this is indeed what has been found. In this work plots have been presented which show acceptable fits to local spirals, irregulars and ellipticals simultaneously in their starbursting, post star-bursting and passive phase. It should also be noted that although both models contain many parameters, very little fine tuning has been

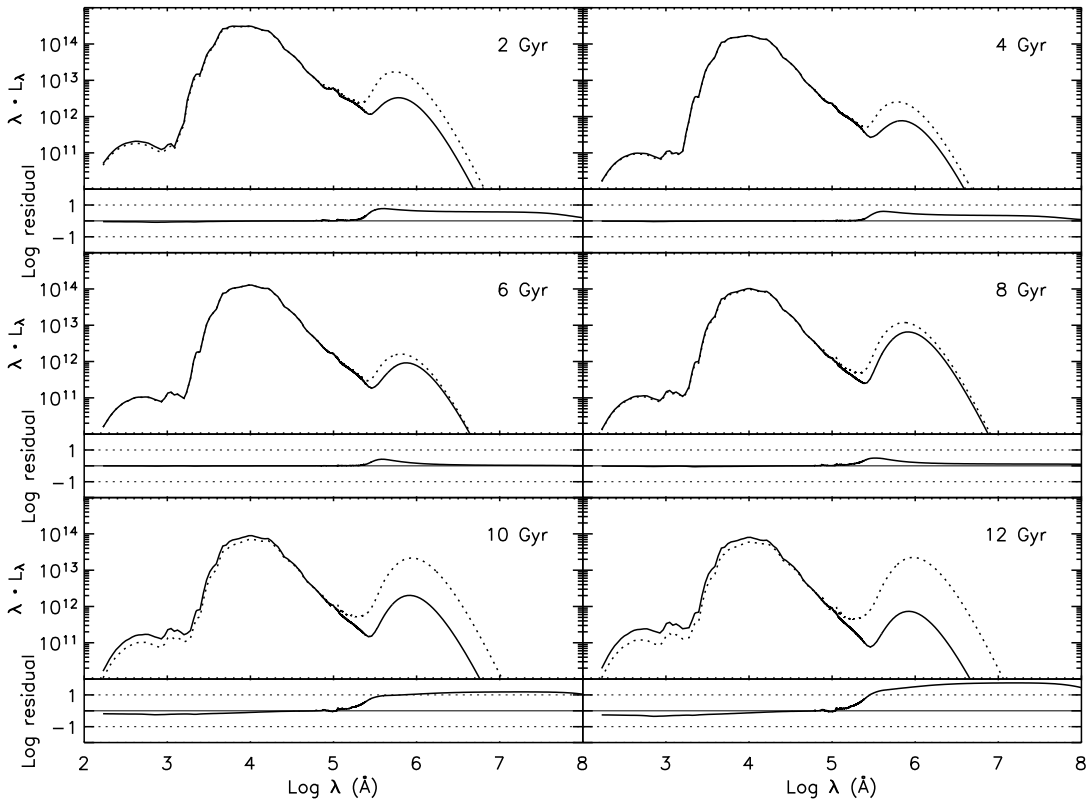

Figure 2.24: The evolution of the SED of the elliptical galaxy, panels the same as for figure 2.5

performed to fit observations. Instead the parameters have been set either to physically reasonable values based on observations or to values which, when used previously, have been found to give good fits to observations. As a result, the fits are remarkably good and, although far from conclusive, seem to validate both the chemical evolution model used (the CPM08 model) and the stellar population model adopted (GRASIL). Only two parameters were tuned in this work to match the observations. For the irregular galaxies in order to fit the MIR part of the SEDs of local dwarf irregulars the optical depth of the molecular clouds (molecular clouds) in which the stars are born, needed to be reduced to a lower optical depth than the molecular clouds in other starforming galaxies. It is not possible to say whether the improved fit requires a lower molecular cloud mass or a larger molecular cloud radius because the optical depth is dependent on both the mass and the radius and is given by: M_{mc}/R_{mc}^2. For the elliptical galaxies, to match the large amount of reprocessing observed in the SEDs of the SCUBA galaxies in the SHADES dataset, the time spent initially by the young stars in the dense molecular clouds was increased to a larger value than that found for local normal starforming galaxies.

In the CPM08 paper it was found that the dust depletion pattern is determined by the balance between destruction and accretion and since neither process can be constrained accurately from the solar neighborhood nothing definite can be learned about the rate of either. However, in both the elliptical and irregular galaxies the accretion rates should be negligible, hence, by studying such environments it should in theory be possible to derive constraints for the destruction rates of the different elements. The reasonable fits to local galaxies support the values chosen.

The use of theoretical template SEDs in comparisons with photometry has proved to be a useful tool in order to gain insights into high redshift galaxies, in particular for determining a photometric redshift (e.g. Rowan-Robinson et al. 2008). Among the templates commonly used are those of well studied starburst galaxies in the local universe, such as ARP 220 and M82. However there is evidence that starburst galaxies at high redshift display different characteristics to their low redshift counterparts. For example showing higher specific star formation rates (star formation rate / stellar mass) (Bauer et al. 2005) and have higher dust obscuration rates (Hammer et al. 2005). It is therefore important

to develop a set of multi wavelength templates specific to the type of galaxy expected at high redshift, particularly due to the recent launch of the European Space Agencys (ESA) Herschel Space Observatory (Pilbratt 2005), which will increase the wavelength coverage for these objects. Our models deal with both the chemical and dust evolution in these early galaxies in a self consistent way and in this work the SEDs generated have been shown to match high redshift galaxies simultaneously in both the starbursting and post starbursting stage. They should therefore provide ideal templates for the analysis of these high redshift galaxies. Further work will be carried out to generate and test a range of high redshift templates.

Also investigated in this work are the potential errors you could expect by introducing two common simplifications into the modelling of galaxies: that the dust-to-gas mass ratio is proportional to the metallicity, and that the dust composition in all galaxies is equal to that derived for the Milky Way. These *errors* are given as the difference between our fiducial models with the detailed dust treatment and the models using the two simplifications. They will only be correct for the models presented here and not for any real galaxy in particular. However the chemical evolution models have been thoroughly tested against observations in previous works and in this work the SEDs have been shown to be broadly consistent with the SEDs of the morphological type modelled. Therefore the disparities presented in this work can be viewed as an example of the magnitude of errors that could be expected if the simplifications are adopted in spiral, irregular and elliptical galaxies. In particular it has been shown that for spiral galaxies the errors that could be expected are small and decrease with the age of the galaxy, this is unsurprising since these simplifications have been developed based on the Milky Way in the case of the chemical composition and the Milky Way in addition to observations of local starforming galaxies in the case of the dust-to-gas ratio. For irregular and elliptical galaxies however it has been shown that potentially the disparities introduced by adopting the two simplifications could be much larger. Of the two simplifications it has been shown that in both galactic types that the simplification likely to lead to the largest disparities is assuming the dependency on the metallicity of the dust-to-gas ratio and that the largest disparities would be expected in the IR part of the spectrum.

The main limitation of this work is that only the total mass in each of the main dust species is followed. The model does not calculate in what proportions they combine with to make up dust grains and what the size distribution of these dust species could be. As a result a major assumption had to be introduced for the composition of the dust grains, that the size distribution does not evolve and all times will be identical to that calculated to match properties of the Milky Way (S98 size distribution). This assumption was relaxed in irregular galaxies where a dust composition consistent with the SMC extinction curve was calculated and in young elliptical galaxies where a dust composition consistent with the extinction curve of a high redshift QSO was found. It was shown that adopting the dust composition based on the SMC had only a small effect on the SEDs. The effect of adopting the dust composition consistent with the QSO in young elliptical galaxies had a large effect particularly in the NIR and MIR. With the current observational data it was not possible to put strong constraints on which size distribution is the more realistic but the huge difference in the SEDs generated using the two different distributions highlights how important using the correct size distribution could be and how it could have large consequences for surveys or any observations taken shortward of the peak of the dust emission. Precisely the wavelength range which the Herschel Space Observatory is set to operate in.

2.6 Summary

Starting from the models proposed in the CPM08 paper the chemical and dust evolution models have been combined with the GRASIL spectrophotometric population synthesis code in order to generate SEDs for the solar neighborhood and irregular and elliptical galaxies from the birth of the galaxy to an age of 13 Gyr.

The SEDs have been compared where possible to observed SEDs. A good fit has been obtained for the spiral model when compared to local spiral galaxies, the elliptical model has simultaneously fitted observations of high-redshift starbursting (SCUBA) galaxies, high-redshift post starburst galaxies and local galaxies, while the irregular galaxy model has been shown to match adequately the SEDs of local irregular galaxies of magellanic type. The results are particularly remarkable since very few of the GRASIL parameters were fine

tuned in order to obtain these results, instead they were merely set to a combination of observationally motivated values or to values which have been found to give good fits to observations in previous works. The good fits give further indications that the galaxy formation scenarios chosen for each morphological type in order to fit the chemical properties of these galaxies are indeed valid. In addition the good fits particularly to the local elliptical and irregular galaxies suggest that the dust treatment adopted in the CPM08 paper are reliable and in particular support the destruction and accretion rates chosen. From these fits to observations it has been shown that the optical depth in molecular clouds in irregular galaxies is likely to be lower than that of normal starforming galaxies. It has also been found that in order to match the observations of SCUBA galaxies the stars in the young extreme starbursting galaxies initially spend a large period of time in dense molecular clouds before escaping.

It has been shown that SEDs generated using either the assumption that the dust grain distribution in all environments is equal to that of the Milky Way or the assumption that the dust-to-gas mass ratio scales with the metallicity differ from those calculated using a full dust evolution model. Of these assumptions it has been found that assuming a dust-to-gas ratio will introduce the largest disparities while the disparities introduced from an assumed chemical composition are small, only having a potentially large effect in the MIR, due to a change in the abundance of PAH molecules. For spiral galaxies the disparities incurred by adopting the assumptions are small and will decrease with age and therefore increase with redshift, to a large part due to the normalisation of the assumptions in this model to the results calculated for the spiral galaxy at 13 Gyrs. The disparities introduced by adopting the assumptions are more significant in the galaxies of the two other morphologies at all ages particularly in elliptical galaxies and therefore dust assumptions tuned to match those of the Milky Way should be used with caution in these galaxies.

It has also been shown that while using a Milky Way size distribution to model irregular galaxies should be a reasonable simplification, for elliptical galaxies at high redshift such a simplification could potentially lead to large errors.

The reasonable fit of the young elliptical galaxy to SCUBA galaxies at a redshift of ~ 2.2 and to a massive post starburst elliptical at a redshift of ~ 5 suggests that the

starbursting scenario adopted in this work is a reasonable one and that models generated by these models could act as useful templates to fit to high redshift galaxies.

Chapter 3

Modelling SEDs with Artificial Neural Networks

In this section we describe the implementation of an Artificial Neural Network (ANN) into the GRASIL model with the purpose of significantly reducing the computation time. Details are given about the ANN method in general and about the specific application in the GRASIL model. The form of the input neurons are discussed and results of the implementation presented. This chapter will provide the basis of a paper, Silva, Schurer et al. (2009), to be submitted soon.

3.1 Introduction

As recalled in the chapter 1, the SED of galaxies contains a convolved information on their stellar and gas content, on the age and abundances of stellar populations, on the chemistry and physical state of the interstellar medium, on the star formation rate (SFR) and history. It is therefore the most direct probe to study galaxy formation and evolution, both by direct observations and by theoretical modelling.

From the theoretical point of view, the modelling of galaxy formation and evolution in a cosmological context involves many processes at very different scales, from Mpcs to a pc and under. The widest range of observed galaxy properties have been analysed using

the so-called semi-analytic methods (White & Rees 1978; Lacey & Silk 1991; White & Frenk 1991), that consist in calculating the evolution of the baryon component using simple analytical approximations, while the evolution of the dark matter is calculated directly using gravity-only N-body or Monte Carlo techniques.

The final step to get the output simulated galaxy catalogues which can be compared to observations, is the computation of the full wavelength range SED for each mock galaxy. This should be calculated by appropriately taking into account for each galaxy its particular star formation and metallicity history and geometrical arrangement of the stellar populations and of the ISM, as predicted by the model. The simulated SED catalogue can then be compared to real observed galaxy surveys, so as to check whether the predictions are or are not representative of the real universe and to retrieve some information on the galaxy formation process. In principle, the best way to proceed would be a to use a model which allows any geometrical configuration for the distribution of stars and ISM, such as a full Monte Carlo radiative transfer code, or our new code, GRASIL-3D, described in chapter 4. This is not feasible, however, because of diverging computing times. In fact, radiative transfer Monte Carlo codes at present are used coupled with hydro-simulations of single galaxies, not for cosmological applications (e.g. Jonsson et a. 2006; Chakrabarti et al. 2007; Li et al. 2008). Since the attempt to theoretically understand the assembly of baryons within the hierarchy of dark matter halos is inevitably subjected to strong uncertainties and degeneracies, as many observational constraints as possible must be taken into account by models, in order to get some hints as to the overall scenario and possibly the main physical processes involved. Therefore only a complete multi-wavelength analysis of galaxy data can help to unlock the complexities of galaxy formation and evolution.

Most semi-analytical models (SAMs) have made use of simple empirical treatments to compute the SED (e.g. Guiderdoni et al. 1998; Kauffmann et al. 1999; Somerville & Primack 1999; Hatton et al. 2003; Blaizot et al. 2004; De Lucia, Kauffmann & White 2004). The only SAMs that includes a UV to sub-mm radiative transfer computation are GALFORM (Cole et al. 2000; Granato et al. 2000; Baugh et al 2005; Lacey et al. 2008), MORGANA (MOdelling the Rise of GAlaxies aNd Active nuclei, Monaco et al. 2007; Fontanot et al. 2007, 2009), and ABC (Anti-hierarchical Baryonic Collapse, Granato et al.

2004; Silva et al. 2005; Lapi et al. 2006). These models have been interfaced with GRASIL to make detailed comparisons and predictions in different spectral ranges.

As previously mentioned in § 1.5, the GRASIL code has been written in order to calculate an accurate SED in a relatively quick time and it is this which has allowed the model to be used extensively for calculating the SEDs for the above mentioned SAMs. Despite this the calculation of the IR SED by GRASIL is still often the bottleneck of the whole project and the computing time becomes prohibitive when considering the exploitation of large-scale structure simulations such as the Millennium Simulation (Springel et al. 2005), which would require millions of galaxy calculations.

To improve on this, with the idea in particular for use with cosmological applications, we have implemented in GRASIL the possibility of computing SEDs with an Artificial Neural Network (ANN) algorithm. This will reduce the computing time significantly without having to rely on unrealistic template approaches or simplified analytical recipes. According to the required application one can choose the desired computational method: a full GRASIL calculation or the quicker ANN mode. The bottleneck within the GRASIL code is the calculation of the radiative transfer through the cirrus and the molecular clouds. It is therefore these two processes that the ANNs will be applied to, with the option of using the ANN for either or both of the processes.

Almeida et al. (2009) have already used the ANN algorithm to insert the GALFORM+GRASIL model into the Millennium Simulation to study the properties of the population of sub-mm galaxies. Their method is complementary to the one presented here. They identify the properties of the GALFORM galaxies which are able to determine, through an ANN, their GRASIL SEDs. The method is successful and extremely fast. Their implementation is particularly suited to fully exploit the Millennium Simulation, however, each realization of GALFORM requires its own training of the ANN. The method we have implemented here, on the other hand, is less fast but more general, because the output is directly linked to the galactic properties effectively determining the SED in GRASIL (e.g optical depths, masses of dust, radiation field etc.). Therefore one single training is potentially able to cover a large variety, if not any, application.

3.2 Artificial Neural Networks

3.2.1 Basic concepts

ANN were first introduced as very simplified models of brain behavior (McCulloch & Pitts 1943; Rosenblatt 1958; Widrow & Hoff 1960), mathematical models able to learn from examples and data. They proved very useful in tackling many computationally complex problems, generally non-linear, pattern recognition, classification and function approximation. They are now widely used in all scientific areas such as biochemistry, neuroscience, computer science, mathematics, finance, physics as well as in astrophysics. The architecture of ANNs reflects in someway the biological brain, in that they consists of processing units (neurons) with multiple connections organized as a network and working in parallel. These connections have adaptable strengths (synaptic weights) which modify the signal transmitted to and from each neuron. But in practice ANN can be considered powerful data modelling tools with different possible implementations to address different problems. Their ability to learn, generalisation and adaptability offer several advantages over other data mining and analysis tools.

The working of ANNs is defined by their architecture, propagation rule and learning algorithm:

- **Network Architecture**: The architecture or topology of ANNs refers to the pattern of connections between the computing units and the propagation of data. It can be split into 2 main classes, the *feed-forward* (FF) and the *feedback* (FB) or recurrent ANNs. In the FF case, the information moves only in the forward direction from the input to the output neurons. Recurrent networks contain feedback connections, cycles and loops. The neurons are commonly organized in *layers*, generally with an *input layer*, an *output layer* and possibly one or more *hidden layers*. In the FF pattern, each layer consists of units which receive their inputs from a layer directly below and send their output to units in a layer directly above. There are no connections within a layer. The simple network which can be built with no hidden layers is commonly called a *Perceptron* (Rosenblatt 1958), which can be used only for linear applications. For more difficult tasks, it is necessary to have at least one hidden layer (multi-layer

networks or perceptrons). In particular, the *universal approximation theorem* (Haykin 1999) states that one single layer of hidden units suffices to approximate any function (with a finite number of discontinuities) to arbitrary precision, provided the activation function (see the propagation rule) of the hidden layer is non-linear.

- **Signal propagation rule**: The basic working of the brain consists of neurons receiving electrochemical signals from other neurons, some of which excite the cell, other inhibit it. The neurons adds all these contributions and, if the sum is greater than a certain threshold, the neuron is activated, i.e. it transmits the signal further on. In analogy, each computational unit in the net receives a signal from all the neurons it is connected to, with the strength of each connection quantified by a weight. The unit multiplies each input signal by the weight of the corresponding connection and sums all the contributions. At least one non-linear *activation function* f is operated on the total signal to give the output value that is then passed on as an input to the neurons in the following layers. In practice: $o_j = f(\sum w_{jk}\, i_k)$, where o_j is the output signal from the jth neuron, i_k are the incoming signals from all the neurons connected to it, with corresponding weights w_{jk}. Typical activation functions are the sigmoid, $f(x) = \frac{1}{1+e^{-c\,x}}$, Gaussian $f(x) = e^{-(c\,x)^2}$, and Elliot $f(x) = \frac{c\,x}{1+|c\,x|}$.

- **Learning algorithms**: There are 2 main methods for the training of the ANNs, *supervised* and *unsupervised* nets. In the first case the net is trained with a given target, i.e. the ANN is taught that for a given input it has to provide a given output, and the net adapts its connections (weights) so as to produce the desired answer. In unsupervised learning the net does not have a target output. It is used to find patterns and group the data.

  There are several methods within the supervised learning, all of which consist of a comparison between the predicted output from the ANN with the target output. The most widely used one is the *back-propagation* (BP) algorithm (Rumelhart, Hinton & Williams 1986). The errors are propagated backwards from the output nodes (directly defined by the comparison between the predicted and target values) to the inner nodes. This method is used to calculate the gradient of the error of the network with respect

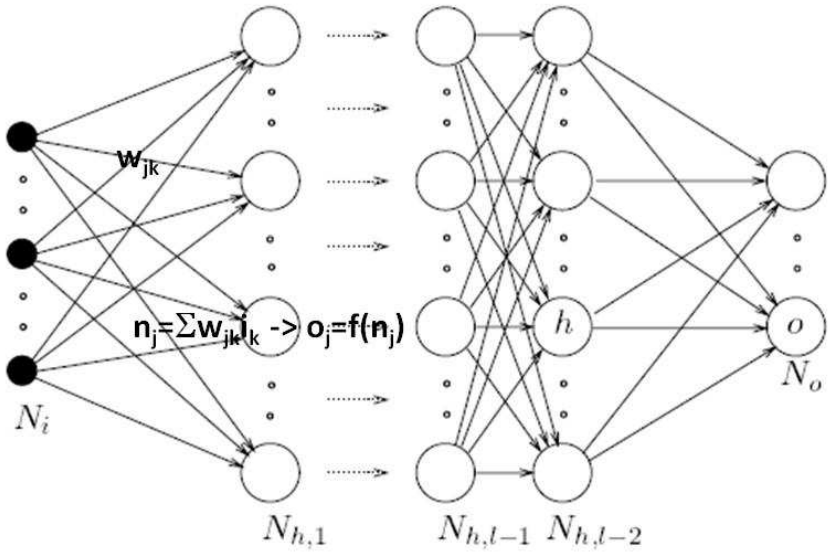

Figure 3.1: Schematic representation of a feed-forward multi-layer ANN: a network of connected computing units ("neurons"), with a set of input units (in our case the controlling parameters of the SED), and a set of output units (in our case the SED, one unit for each λ). The weights (strengths) of the connections between each couple of units of consecutive layers are the adjustable parameters of the ANN. This is accomplished by training the ANN to reproduce a large set of pre-computed inputs (SED controlling parameters)-outputs (corresponding SED). See text for more details.

to the network's modifiable weights and thus to adjust the weights to find the (local) minimum of the error function with the gradient descent method.

3.2.2 Feed-forward multi-layer back-propagation ANN

The ANN we have implemented in GRASIL is one of the most commonly used ones, the FF BP one. It formally works as follows (see Fig. 3.1):

1. Consider a M-layer network, with layer $l = 0$ the input layer, $l = M$ the output layer, and $l = 1, .., M-1$ the hidden layers. Each layer consists of $N^{(l)}$ neurons, with values

given by the vector $\vec{a}^{(l)}$.

2. An input vector $\vec{a}^{(0)}$ is provided with values for all of the input parameters, with a corresponding target vector $\vec{t}$ used for training, that can be compared with $\vec{a}^{(M)}$ to test and train the net.

3. The output from each layer $\vec{a}^{(l-1)}$ is used as an input to the upper layer to find $\vec{a}^{(l)}$. Each neuron $a_i^{(l)}$ of layer l is connected to all neurons $a_j^{(l-1)}$ of the previous layer through a weight $w_{ij}^{(l)}$ that defines a matrix $W^{(l)}$ (with $N^{(l)} \times N^{(l-1)}$ elements, with the row indices for the destination neuron, and column ones for the source neuron) and a bias vector $\vec{b}^{(l)}$ such that:

$$n_i^{(l)} = \sum_{j=1}^{N^{(l-1)}} w_{ij}^{(l)}\, a_j^{(l-1)} + b_i^{(l)} \tag{3.1}$$

$$a_i^{(l)} = f(n_i^{(l)}) \tag{3.2}$$

   i.e., first there is a linear transformation of the input vector $\vec{a}^{(l-1)}$ through the weight matrix $W^{(l)}$ and the addition of a bias vector $\vec{b}^{(l)}$, then the resulting vector $\vec{n}^{(l)}$ is operated on by a *transfer* or *activation* function f to yield the values of the neurons in the new layer.

4. An ANN will usually have *at least one non linear activation function*, with a common choice being the sigmoid function:

$$f(x) = \frac{1}{1 + \exp(-c\,x)} \tag{3.3}$$

   where c is a parameter. Usually $c = 1$ when the input neurons are scaled to range between -1 and 1 (see below). One of the most popular networks, that we adopt here, has one hidden layer, with a non linear sigmoid transfer function from the input to the hidden layer, and a linear transfer to the output.

5. The values of the weight matrices and of the bias vectors are the free parameters of the net. They are found by training the net by comparing many pairs of input $\vec{a}^{(0)}$

and target $\vec{t}$ vectors with a training set of cases. For each pair an error is computed typically as the sum-of-squares error:

$$E = \frac{1}{2} \sum_k (a_k^{(M)} - t_k)^2 \tag{3.4}$$

The aim is to minimize the total error function with respect to each element of $W^{(l)}$ and $\vec{b}^{(l)}$ (over all the pairs input-target, i.e. $E_{tot} = \sum E$).

A common way is to find the minimum of the multi-dimensional error surface in the weight space with the *gradient descent* method, in which the weights are adjusted from small initial random values by following the fastest decrease as given by the negative of the gradient of E:

$$\begin{aligned} w_{ij,new}^{(l)} &= w_{ij,old}^{(l)} - \alpha \frac{\partial E}{\partial w_{ij}^{(l)}} \\ b_{i,new}^{(l)} &= b_{i,old}^{(l)} - \alpha \frac{\partial E}{\partial b_i^{(l)}} \end{aligned} \tag{3.5}$$

The constant α is called the *learning rate*.

6. The gradients of E are calculated with the *back-propagation algorithm*, in which the error evaluated from the computed $\vec{a}^{(M)}$ and the target values $\vec{t}$ is back-propagated to assign an error to each neuron of the previous layers, from the output to the input. This error is a weighted sum of the errors computed for all upper neurons connected to it. In practice:

$$\begin{aligned} \frac{\partial E}{\partial w_{ij}^{(l)}} &= \frac{\partial E}{\partial n_i^{(l)}} \frac{\partial n_i^{(l)}}{\partial w_{ij}^{(l)}} = \frac{\partial E}{\partial n_i^{(l)}} a_j^{(l-1)} \\ \frac{\partial E}{\partial b_i^{(l)}} &= \frac{\partial E}{\partial n_i^{(l)}} \frac{\partial n_i^{(l)}}{\partial b_i^{(l)}} = \frac{\partial E}{\partial n_i^{(l)}} \end{aligned} \tag{3.6}$$

which can be easily found by the definition of $n_i^{(l)}$ as the linear weighted sum $W^{(l)}\,\vec{a}^{(l-1)} + \vec{b}^{(l)}$. So we have to find $\delta_i^{(l)} \equiv \frac{\partial E}{\partial n_i^{(l)}}$. For all the layers $l \leq M-1$, we consider that

a change in the $i-$th neuron of layer l will affect all the neurons of the upper layer $(l+1)$ connected to it:

$$\delta_i^{(l)} = \sum_{j=1}^{N^{(l+1)}} \frac{\partial E}{\partial n_j^{(l+1)}} \frac{\partial n_j^{(l+1)}}{\partial n_i^{(l)}} = \sum_{j=1}^{N^{(l+1)}} \delta_j^{(l+1)} \frac{\partial n_j^{(l+1)}}{\partial n_i^{(l)}} \tag{3.7}$$

$$\begin{aligned} \frac{\partial n_j^{(l+1)}}{\partial n_i^{(l)}} &= \frac{\partial(\sum_{k=1}^{N^{(l)}} w_{jk}^{(l+1)}\, a_k^{(l)} + b_j^{(l+1)})}{\partial n_i^{(l)}} = \\ &= \frac{\partial(w_{ji}^{(l+1)}\, f(n_i^{(l)}))}{\partial n_i^{(l)}} = w_{ji}^{(l+1)}\, f^{'}(n_i^{(l)}) \end{aligned} \tag{3.8}$$

$(a_k^{(l)} = f(n_k^l))$.

Therefore:

$$\delta_i^{(l)} = f^{'}(n_i^{(l)}) \sum_{j=1}^{N^{(l+1)}} \delta_j^{(l+1)}\, w_{ji}^{(l+1)} \tag{3.9}$$

From the knowledge of the error at the output layer, that is directly derived as:

$$\delta_i^{(M)} = \frac{\partial[\frac{1}{2}\sum_{j=1}^{N^{(M)}}(a_j^{(M)} - t_j)^2]}{\partial n_i^{(M)}} = (a_i^{(M)} - t_i) f^{'}(n_i^{(M)}) \tag{3.10}$$

the error is therefore propagated from the output layer backwards.

7. After each *epoch* of training (a passage over all the given input-target pairs) the weights are adjusted until the total error reaches a desired minimum value or a prefixed maximum number of epochs is reached. This scheme is actually subject to overtraining, i.e. the net could become too specialized for the specific cases used for its training. In order to define a valid stopping criterium, it is customary to make use also of a *verification set* of input-target pairs, not used for adjusting the weight but as a check of the error, so both the total error of the training and validation sets are checked at each iteration. The verification set, together with an empirical choice for the value of the learning rate, of the maximum number of iterations, and of the neurons of the hidden layer allows an optimal training of the ANN.

The trained ANN, i.e. the best fit values ($w_{ij}^{(l)}$) and $\vec{b}^{(l)}$, is then used to reconstruct the output corresponding to any given set of input parameters.

3.3 Implementing ANN in GRASIL

The prediction of galaxy spectra is a complex problem due to the high number of input and output variables, and the non-linearity among the elements. Neural networks represent a viable solution for this non-linear function prediction.

The typical computing time to run GRASIL on a $\sim$ 2 GHz CPU ranges from $\sim$ half a second for the no dust case to $\sim$ 10 minutes for the bulge plus disc case. A pure bulge (i.e. spherical symmetry) requires $\gtrsim$ 1 minute, a pure disc $\gtrsim$ 2 minutes, a bulge and disc geometry requires $\sim$ 10 minutes (the exact value depending on the number of radial and angular grid points set according to the "compactness" of the model). Most of the time is spent computing the IR emission from dust, of which $\sim$ 70 to $>$ 90% is required by the emission from the cirrus component. In fact, each volume element of the model in a 3D grid has its own radiation field and amount of dust, whose emission is calculated for each type of grain. Instead, computing the extinction of stellar radiation by the two dusty components of the ISM (molecular clouds and cirrus) is straightforward, $\sim$ 1 second. These considerations drove our strategy to use an ANN algorithm to reconstruct only the IR emission from molecular clouds and cirrus. To this aim, the calculation of the extinction by the molecular clouds and the cirrus provides the amount of energy absorbed and therefore the normalization for the two components, while we have implemented the ANN to predict their spectral shapes.

Due to the very different nature and treatment of the dense and diffuse components, the quantities (input neurons) that determine the IR SEDs are different for the molecular clouds and for the cirrus. Therefore we have considered and implemented in GRASIL two separate ANNs, so that it is possible to run the code in the "ANN mode" for both components or for only one of them. In the latter case, the emission from the other component is computed in the "full" mode.

We have implemented a 2 layer ANN, i.e. an input layer, 1 hidden layer and an

output layer, with a sigmoid activation function from the input to the hidden layer. Indeed by properly identifying the input neurons and setting the network parameters (number of neurons of the hidden layer, learning rate, maximum number of iterations) the universal approximation theorem means that this architecture is capable of universal optimal approximation. Moreover, it has been found empirically that networks with multiple hidden layers are more prone to getting caught in undesirable local minima (Duda & Hart 1973; Haykin 1999; Bishop 1995). To create and use the trained net to predict SEDs we have adapted the F90 code by B. Fiedler freely available at http://mensch.org/neural/.

3.3.1 Input and output neurons

For each dusty component we have identified the physical quantities defining their spectral shape. Their respective total luminosity is known from the direct computation of the amount of stellar energy within molecular clouds and emerging after extinction by molecular clouds, as well as the amount of stellar radiation heating the cirrus (i.e. emerging from molecular clouds together with that of more evolved stars already out of molecular clouds) and emerging from it. The prediction of the spectral shapes therefore require the definition of normalised quantities.

The identification of the driving input parameters is based of course on expectations and experience, but also, in particular for cirrus, on trial and error, in order to extract all the necessary quantities.

In the following $L_\star$ indicates the bolometric luminosity (total intrinsic stellar luminosity), $L_{\star,MC}$ the luminosity of stars within molecular clouds, $L_{\star,c}$ the luminosity of stars heating the cirrus. All luminosities and masses are expressed relative to one of them.

The output neurons are the SEDs, i.e. one value of λL_λ for each λ, both for for molecular cloud and for the cirrus. So their number depends on the desired resolution of the SEDs. Typically we use ~ 1000 wavelength points, i.e. output neurons, for broad band SEDs (several hundreds points are used to follow the ~ 20 PAH bands).

Input neurons for molecular clouds

The way in which we treat molecular clouds allows their contribution to be defined by two parameters:

- τ_{mc} = molecular cloud optical depth (given at 1 μm).
- $R_{mc}[pc]/(12\sqrt{(}L_{\star mc,46})$ = ratio of the molecular cloud radius over an estimate of the sublimation radius dependent on the luminosity of stars within each cloud (in 10^{46} erg/s) and the adopted sublimation temperature T_s for dust. We recall that while T_s is typically $1000 - 2000$ K for silicate and graphite grains, we used a lower value in molecular clouds (we found $T_s = 400$ K to properly represent the maximum attainable dust temperature in star forming molecular clouds) to account for the assumed central point source within molecular clouds instead of a (unknown) distribution of sources (see discussion in S98 and S99)

In Fig. 3.2 we show a family of SEDs of molecular clouds where we highlight the separate effect of the two driving parameters. This small number of parameters is because of the assumption of spherical molecular clouds with a central point source. With this configuration, once the stellar central source is fixed, the shape of molecular clouds depends only on their optical depth and on the ratio between the outer and inner (sublimation) radius (see Granato 1994 for more details). These control the temperature distribution of the dust through the cloud, the depth of the silicate feature, and the steepness of the MIR SED. We recall that for molecular clouds in GRASIL, $\tau \propto \delta\, M_{mc}/R^2_{mc}$, where δ is the dust to gas mass ratio, and the other quantities refer to the mass and radius of molecular clouds. The proportionality constant depends on the intrinsic dust properties.

Input neurons for Cirrus

The cirrus emission is defined by 7 neurons for spherical symmetry, 9 for discs and mixed geometry:

- $\log(L_{Cir}/L_{\star,c})$ = cirrus dust luminosity normalized to the stellar luminosity heating the cirrus. This therefore provides a measure of the amount of dust reprocessing.

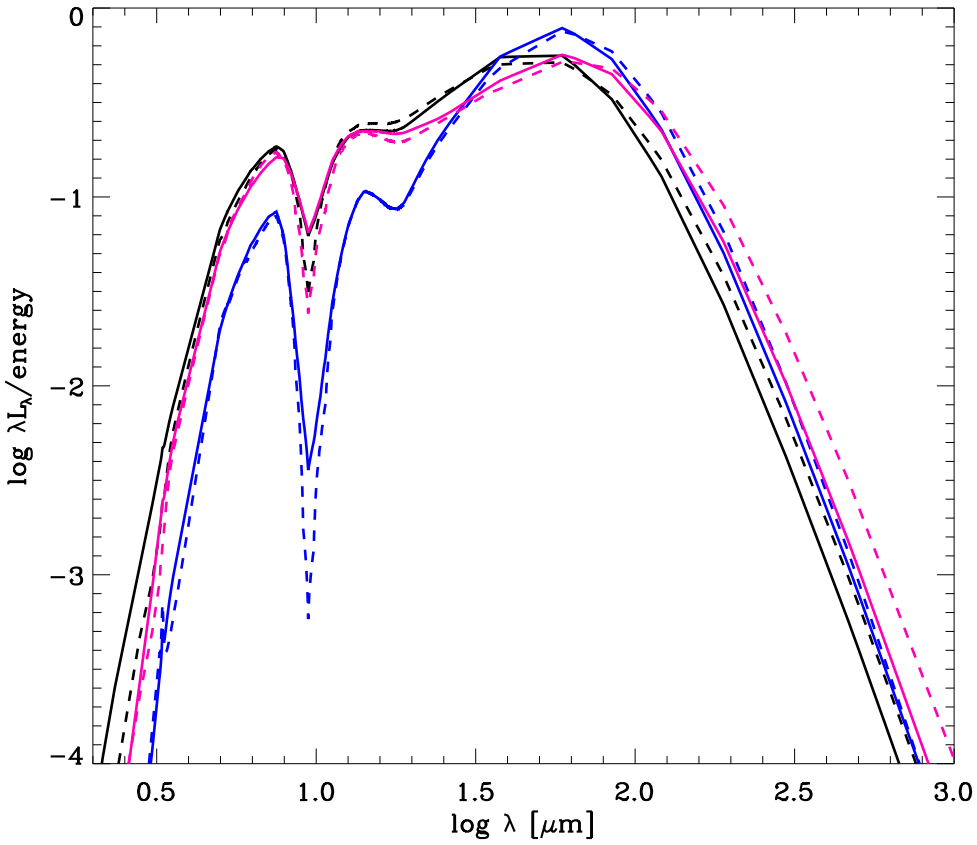

Figure 3.2: molecular cloud SED controlling parameters. Black line: SED obtained with $\tau_{mc} = 25.4$ at 1μm, and $rcloud[pc]/(12\sqrt{(L_{\star mc,46})} = 104$. Blue line: effect of varying τ alone, $\tau_{mc} = 50.8$ (obtained by doubling the dust to gas ratio). Pink line: effect of varying the molecular cloud extension alone, $rcloud[pc]/(12\sqrt{(L_{\star mc,46})} = 206$ (obtained by decreasing the escape time scale from 0.08 to 0.0014 Gyr). Continuous: full. Dashed: ANN. All the SEDs are normalized to their own energy to highlight the change in shape.

- $\log(M_{Cir}/L_{\star,c})$ = normalized cirrus dust mass, expected to be strongly correlated with the typical dust temperature.
- τ_p = polar optical depth due to cirrus alone (integral of the dust density distribution along the polar direction, given at 1μm).
- τ_e = equatorial optical depth due to cirrus alone (defined as τ_p but along the equatorial path)
- τ_h = optical depth if cirrus were spherically and homogeneously distributed.
- **Geometrical ratios**: Dependent on the geometry of the galaxy used (see figure 1.9 § 1.5) and For the bulge component: r_c^*/r_c^d; for the disc component r_d^*/r_d^d, z_d^*/r_d^*, z_d^d/r_d^d.
- **Hardness ratio**: ratio of the radiation field at 0.3μm over 1μm heating the cirrus (thus emerging from molecular clouds and stars already out of molecular clouds). Since small grains and especially PAHs are excited most effectively by relatively hard UV photons, this quantity is correlated with the ratio between the NIR-MIR emission they produce, and the far IR emission due to big grains.

The geometry and treatment of the interaction of the radiation field with the cirrus dust requires the accounting of this many parameters, since the behavior of the SED is highly non linear. Examples of the effect of the cirrus neurons are shown in Fig. 3.3.

3.4 Applications

3.4.1 Trained net

In order to predict SEDs with the ANN we first have to build a training net. By making use of a large SED library built with CHE_EVO+GRASIL, we have empirically adjusted the optimal values for the number of neurons in the hidden layer (20 for molecular clouds, 35 for cirrus), we set to 500 the maximum number of iterations, and to 0.001 the value of the learning rate.

Then we had to identify a suitable set of training examples encompassing a large case study. Since the ANN we have implemented reconstructs the GRASIL SEDs from

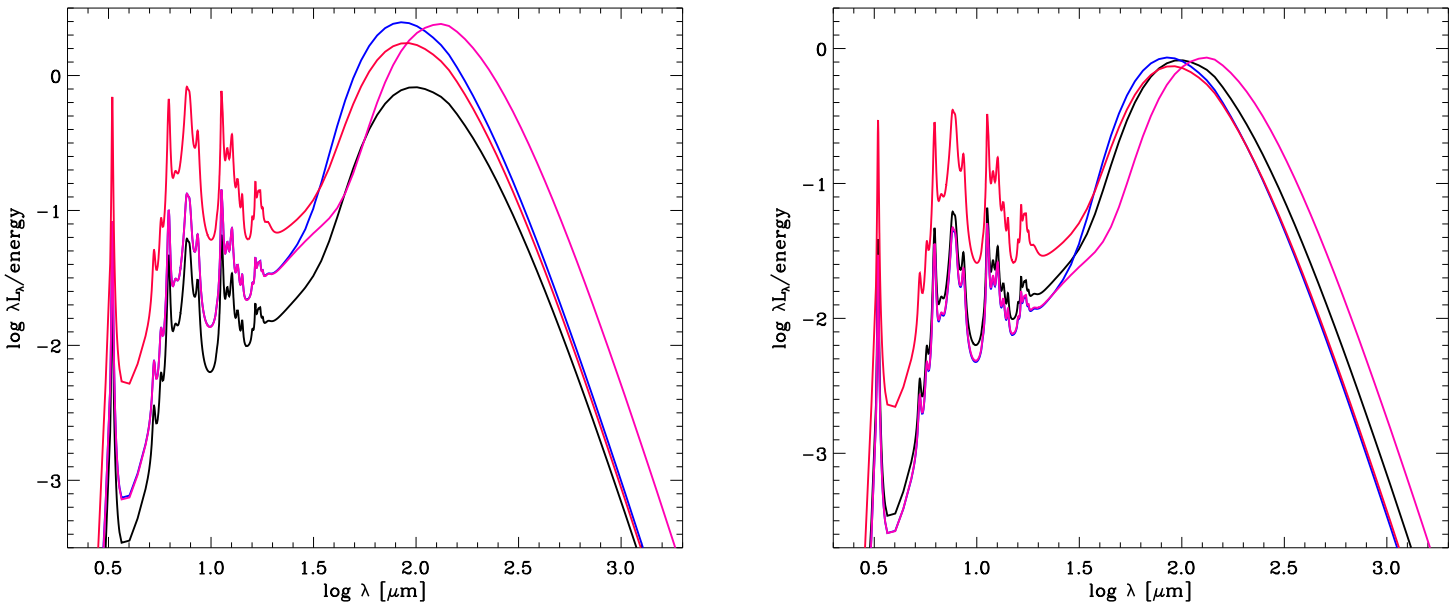

Figure 3.3: Some examples of the effect of the cirrus input neurons. Black line: reference cirrus SED. Blue line: change rcstar and rcdiff to 1/3 of their reference value (so same shape ratio), we get higher τ_p, τ_h and reprocessed luminosity. Pink line: Leave same radii as original, increase mass of cirrus to get same τs as blue, similar reprocessing as blue but very different shape. Red line: increase hardness ratio of the radiation field heating the cirrus, strong effect particularly for very small grains and PAHs. Upper panel: all SEDs normalized to the energy of the black line. Lower panel: SEDs normalized to their own energy to highlight the differences in shape.

their effective physical driving parameters, in principle we could build a single trained net able to work for any application, which would need to encompass a sufficiently large range of values of the input parameters. Actually, the definition of how large the range must be is non trivial, since the properties of the mock galaxies calculated in simulations of galaxy formation are non predictable a priori, nor are those of high-z galaxies in the real universe.

It has also to be understood if for the network to work for any given choice of input parameters, the trained net must include training examples with the *entire* set of inputs bracketing the required ones at the same time, or if it is sufficient to some extent that each single input value is independently within the values included for the training.

Indeed we may expect that the latter, much more favorable possibility is realized, since the advantage of the ANN technique with respect to classical interpolations is in the capability to learn the effect that each parameter has on the SED, mimicking the skill that a real GRASIL user develop with experience. The general performance we have experienced so far appears in fact to confirm our expectations, although it is not possible to show a rigorous demonstration of this. On the other hand, we expect the ANN to fail catastrophically, when one or more parameters are not within the range of values of the training set.

Actually, in some cases we found unacceptable results also when all of the input neurons were represented in the trained net. To improve this problem we found it necessary to use, for each component, two different MLPs, one to predict the SED below 20 μm, and one above. This is because below this wavelength the spacing of SED points has to be much smaller, in order to follow the many spectral features (PAHs and silicate features). Indeed, in the two wavelength regimes we employ typically $\sim 10^3$ and $\sim 10^2$ points respectively. Therefore, if we train a single network to follow the full IR spectral range, the weight of these many MIR SED points is overwhelming, and this results in general in less accurate MLPs, that sometimes may dramatically fail at longer wavelength. An example is shown in Fig. 3.4, where the cirrus emission is completely missed in the FIR and sub-mm using only a single ANN, but when the problem is split in two wavelength regimes the ANNs predict a much more accurate SED.

The reference training net we use in the following examples is built by including some thousands CHE_EVO+GRASIL models, strongly influenced by the range of parameter

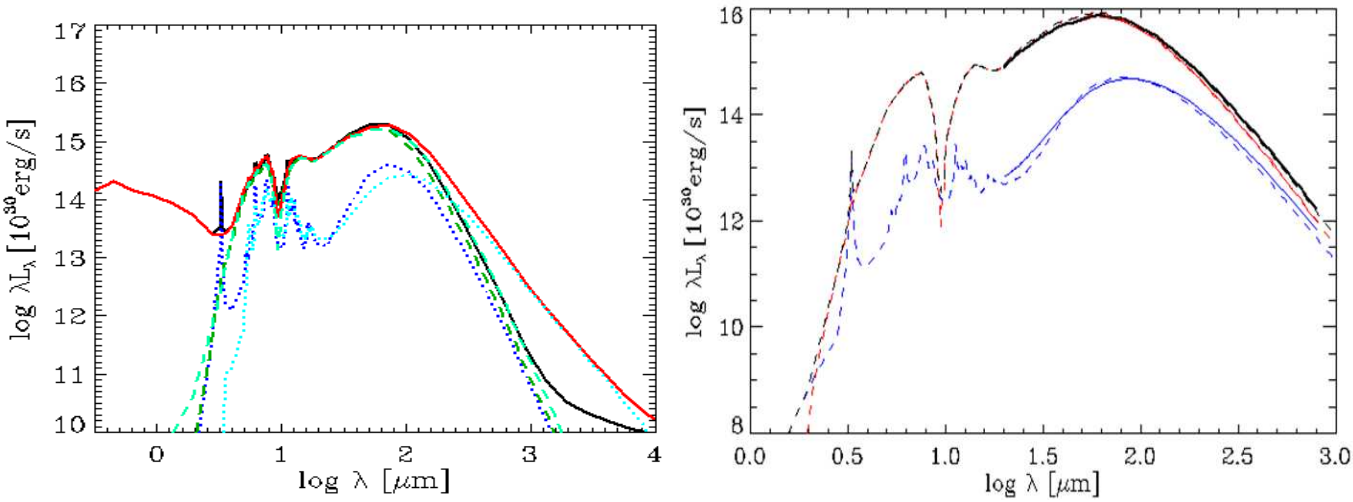

Figure 3.4: One catastrophic case for cirrus and its solution by splitting the ANN output below and above 20μm.

values used in several of our past works (e.g. S98, Vega et al. 2005, 2008, Schurer et al. 2009, Granato et al. 2000, 2004, Silva et al. 2005).

We note that the ANN adopted in the following has been trained on GRASIL models computed with a given, standard, abundance of PAHs and intrinsic dust properties (size distributions, relative abundances of graphite and silicates, slope of the dust emissivity in the submm the submm etc). The full GRASIL model has the freedom to modify these quantities, even if in normal situations this is not necessary (see for example chapter 2). Of course, to exploit this possibility different trained networks would be required.

3.4.2 Examples with single SEDs

In Figs. 3.5 and 3.6 we show the comparison between the computed and reconstructed SEDs for the well known galaxies ARP220 and M82, and their residuals, separately for the total SED, the molecular cloud emission and the cirrus emission. For the latter, the residuals that would be obtained by not splitting the ANN between MIR and FIR is also shown (cyan line). The result is extremely encouraging.

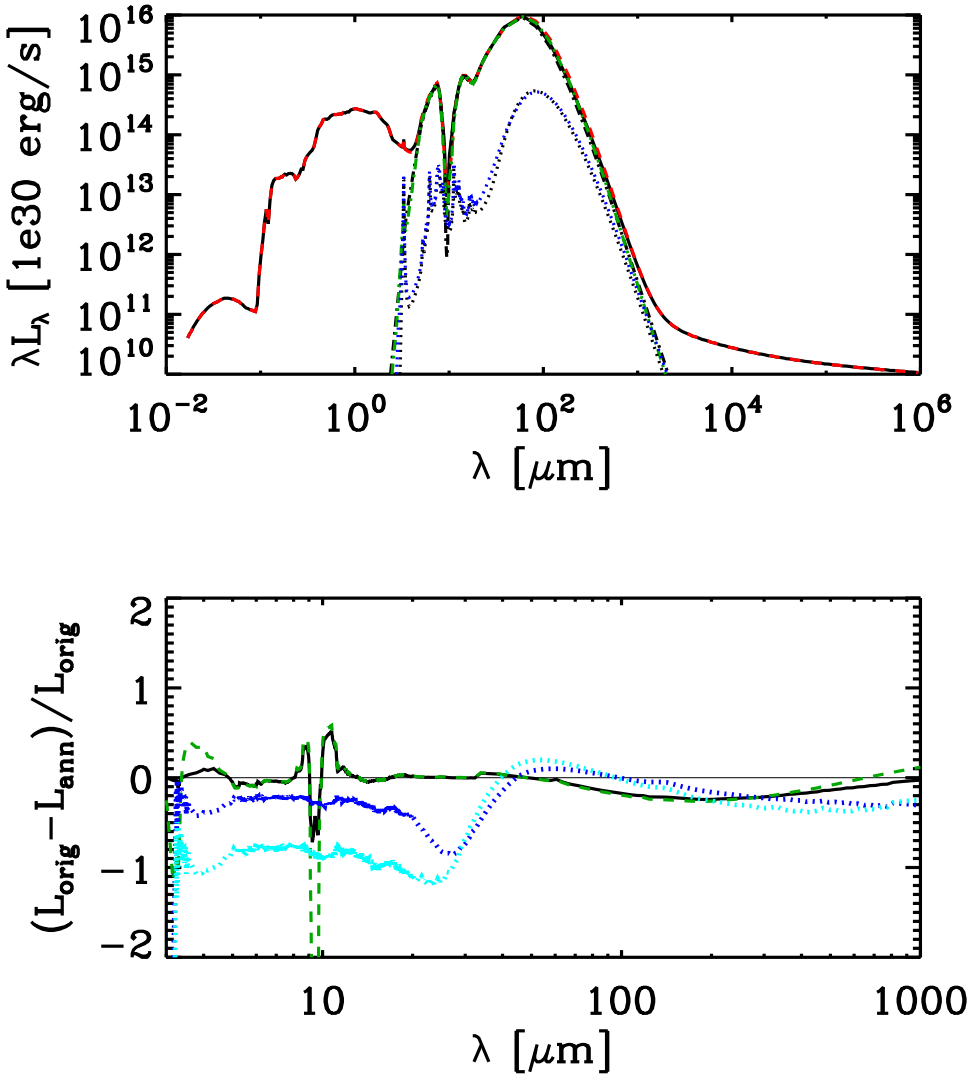

Figure 3.5: ARP220: Original vs ANN and residuals. Upper: Black continuous is total original, red dashed is total ANN; dot-dashed black and green is for molecular clouds; dotted black and blue is cirrus. Lower: Black continuous is residual for total; dashed green residual for molecular clouds; dotted blue residual for cirrus; dotted cyan residual for cirrus if the ANN were not split in the FIR.

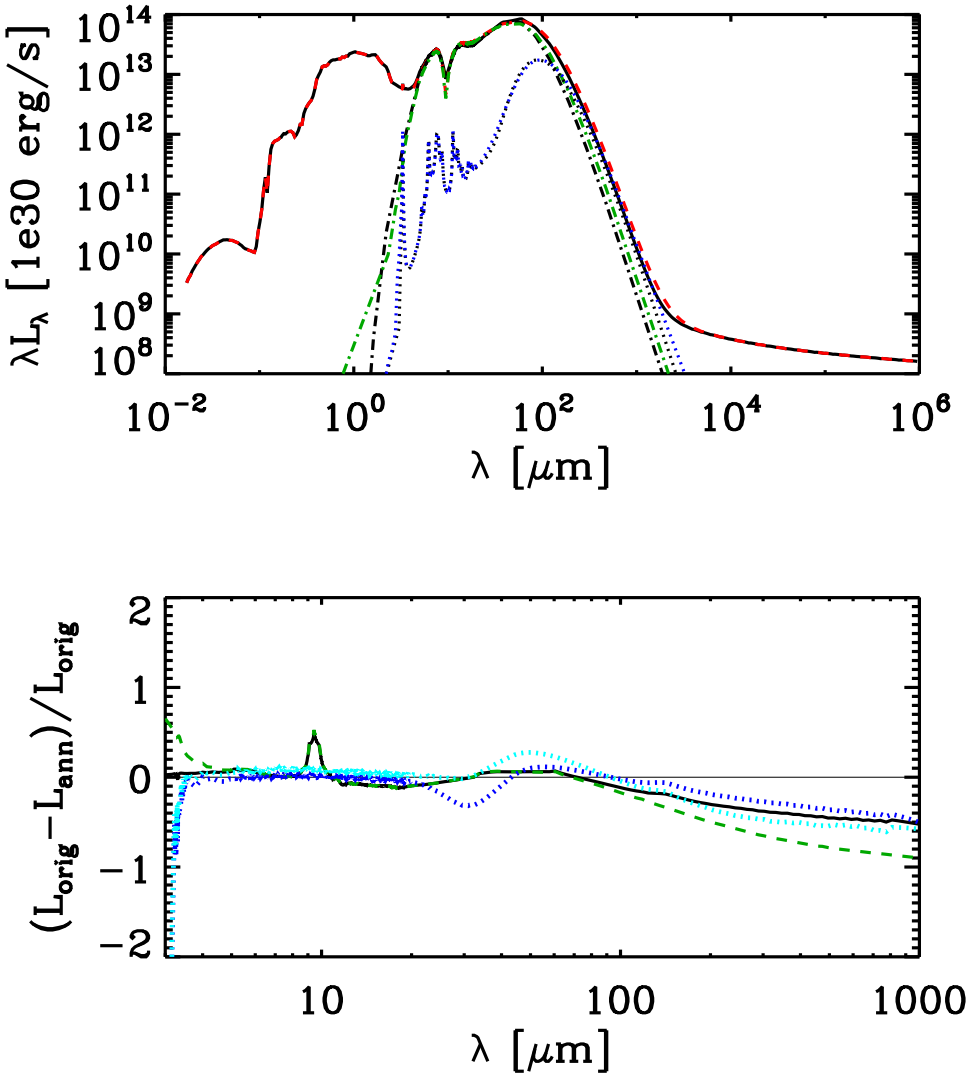

Figure 3.6: M82: Original vs ANN and residuals

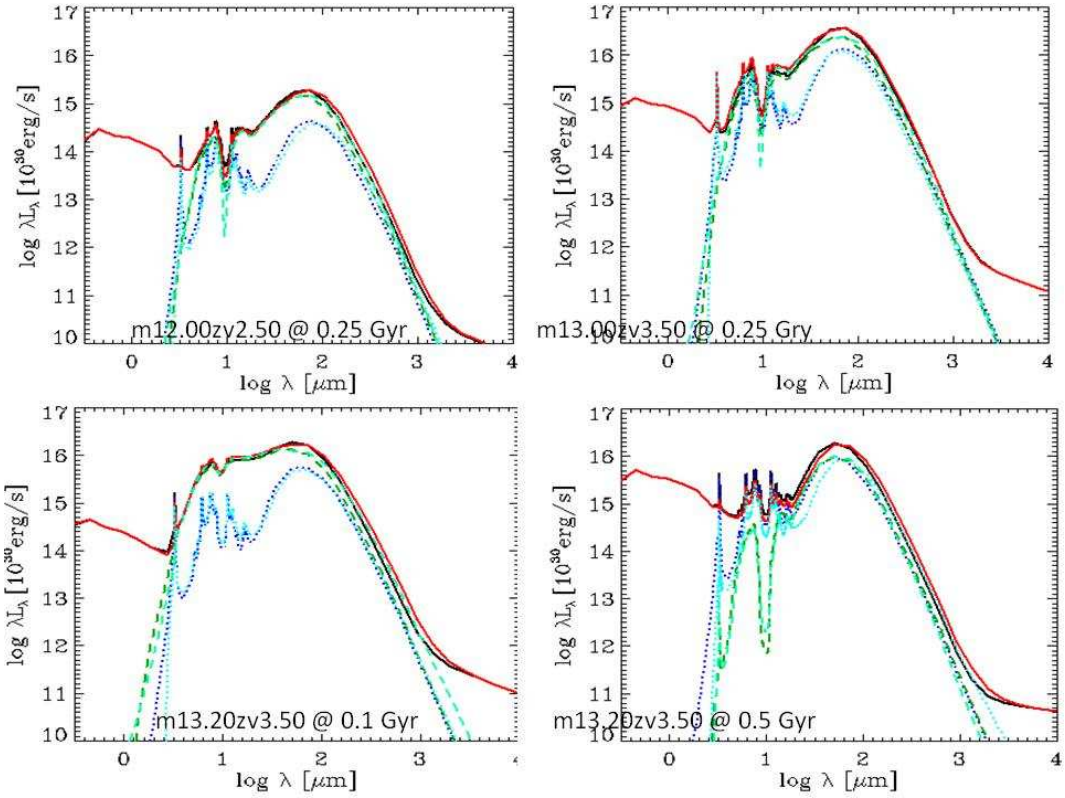

Figure 3.7: Examples of randomly extracted galaxy models from the ABC SAM. The SEDs obtained either with the full GRASIL or the ANN reconstruction are almost superimposed.

3.4.3 Statical samples

We have applied the ANN to the ABC SAM, to check the reconstructed SEDs and ensuing luminosity functions and galaxy counts. In Fig. 3.7 we show 4 examples of randomly extracted SEDs from the ABC model, with the original and ANN SED almost superimposed.

A more statistical comparison is shown in Fig. 3.8, which shows the residuals between the original and ANN SEDs vs wavelength for $\sim$ 1000 objects extracted from a GALFORM galaxy catalogue at $z = 0$ (Baugh et al. 2005). We show the median and the $0.1 - 0.9$ percentiles.

Finally in Fig. 3.9 we show as an example, the galaxy counts at 24 and 850 μm for the ABC model obtained either with the full computed SEDs and with the ANN reconstruction. Integrated quantities such as luminosity functions and counts are easier to

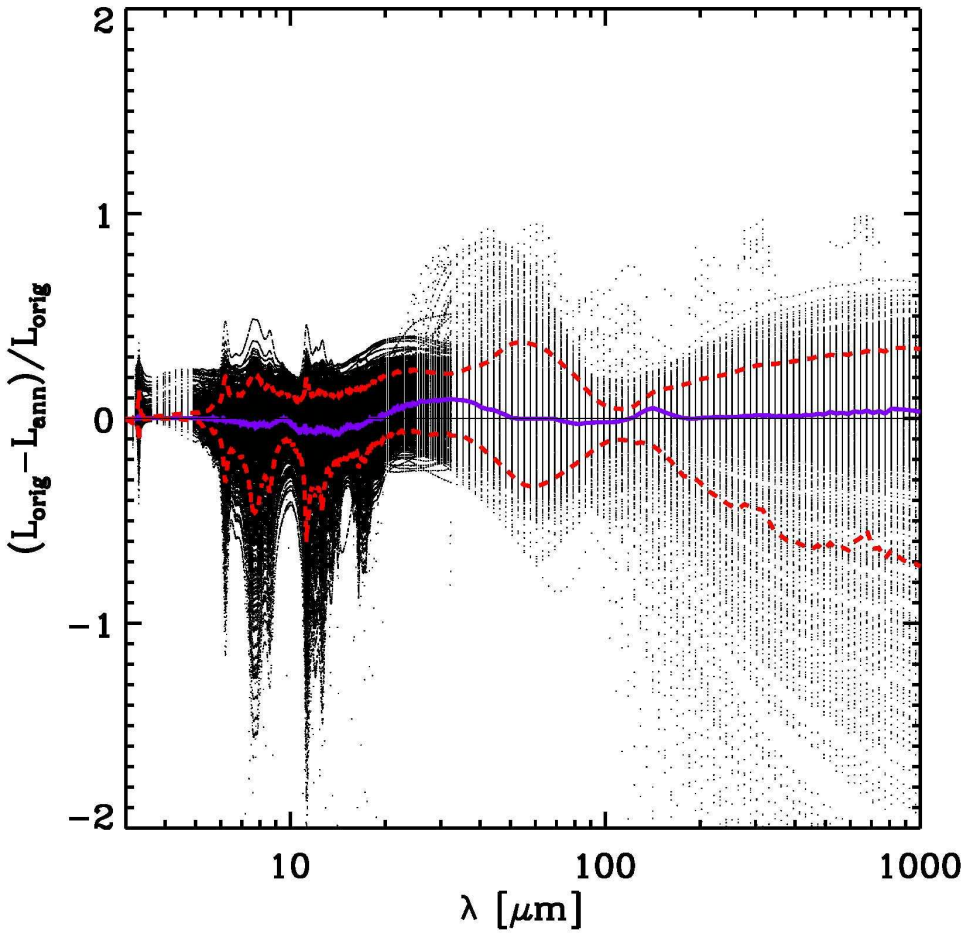

Figure 3.8: Residuals vs wavelength for $\sim$ 1000 galaxies from a z=0 simulated catalogue of GALFORM (Baugh et al. 2005). Purple continuous line: median; Red dashed lines: 10-90% percentiles.

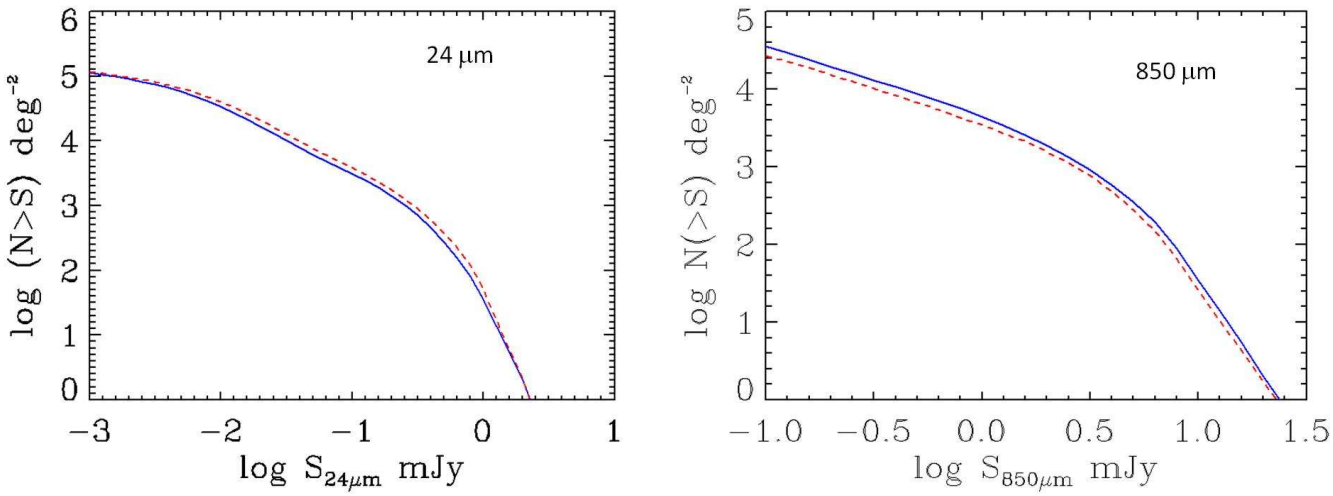

Figure 3.9: Galaxy counts at 24 and 850μm for the ABC SAM: comparison between counts obtained with the full computation for the SED (dashed line), and the ANN reconstruction (continuous line).

be reproduced than SEDs, since small differences in the SEDs tend to smoothed out. We found similar results for these quantities in other bands

3.4.4 Computing performance

The implementation of the ANN into the GRASIL model dramatically reduces the CPU time required to run the code. For a single galaxy, as recalled from before, the GRASIL code for a ~ 2 GHz CPU could take anywhere up to ~ 10 minutes to calculate a SED, depending on the geometry. With the use of an ANN the time taken to calculate a SED for a single galaxy is reduced to only a few seconds with the main CPU time taken up by the processes which are not calculated by the ANN; a CPU gain of more than 2 orders of magnitude. Such a remarkable reduction in computing costs should make possible an efficient comparison of the SEDs of SAMs, which include a proper dust treatment, to large observational galaxy surveys

3.5 Summary

We have implemented an FF-BP ANN into the GRASIL code, identified factors which control the shape of a galactic SED and chosen these as the input neurons. The network has been thoroughly trained and the resultant network tested. We conclude that the computation of SEDs with the ANN method appears robust and computationally advantageous to analyse and test galaxy formation models in cosmological volumes.

Chapter 4

A galaxy dust model for hydrodynamical galaxy simulations

In this chapter we introduce a new photometric SED code, GRASIL-3D, which includes a careful modelling of the dust component of the ISM. GRASIL-3D is an entirely new model based on the formulism of an existing spectrophotometric SED model, GRASIL but specifically designed to be applied to galaxies with any arbitrarily given geometry, such as galaxies calculated by theoretical hydrodynamical galaxy formation codes. The new model has been interfaced with a smoothed-particle hydrodynamics (SPH) code, P-DEVA, and has been used to calculate the SED for a simulated galaxy, and 2D images of the galaxy at several different wavelengths and at several angles. The possible applications of this code in addition to future work needed, is discussed. The work presented in this chapter will form the basis for a paper, Schurer et al (2009), in prep.

4.1 Introduction

As discussed in § 1.5 the dust model GRASIL has been used highly successfully for many years since the initial paper in 1998, for a wide variety of different applications. Perhaps most notably it has been used extensively in combination with semi analytical models of galaxy formation; using outputs from the galaxy formation codes in order to

produce reliable and accurate SEDs, relatively quickly, (Granato et al. 2000, Baugh 2005 et al., Lacey et al 2008, Cook et al. 2009 and see also Almeida 2009) and in chapter 3 a substantially faster version of the code was presented, which will lead to improved usability in this area.

However, despite the many strengths of the GRASIL model, it is not suitable for all applications. The code specifies a profile for the distribution of stars and gas, see figure 1.9, with several degrees of symmetry. While this is highly suitable for one or two zone galaxy formation models which do not calculate the spatial distribution of stars and gas explicitly, there are other forms of galaxy formation codes which do. For such models the use of GRASIL with an artificially specified galactic profile would constitute the loss of a large quantity of useful information.

Hydrodynamical simulations fall into this category, self-consistently forming spatially resolved galaxies within a cosmological framework. To do this the codes employ one of two techniques: smoothed-particle hydrodynamics (SPH) or adaptive-mesh techniques. These codes however only trace the evolution of mass, while observations trace light. Therefore to test the simulations against observations, interfacing the outputs with galactic models which can predict a multi-wavelength SED, including a careful treatment of the radiation transfer through the dust, is essential. In order to take advantage of the spatial information produced by these models a free choice of the galaxies geometry is necessary.

Several dust models already exist for this purpose, for example: SUNRISE (Jonsonn 2004; Jonsonn et al 2006; Jonsonn et al 2009); RADISHE (Chakrabarti et al 2008; Chakrabarti & Whitney 2009); Art^2 (Li et al 2007; Li et al 2008), all using Monte Carlo techniques to follow the radiation of photons through the diffuse ISM and to calculate a global radiation field, and hence the dust re-emission. In addition SUNRISE now includes the treatment of star-forming regions using the dust and photo-ionization code MAPPINGSIII (Groves et al 2008), more details can be found in § 1.4.

This chapter will discuss a new model based on the GRASIL formulism which has been designed to be applied to any hydrodynamic simulation, GRASIL-3D. The motivation for this new model comes from adapting the GRASIL code, which has already proved so successful in describing galaxies of many different types, adopting the main concepts

of the model in our new code, thereby building on the strengths of this established code while avoiding the computationally expensive Monte Carlo techniques used in other models. GRASIL-3D is still in the development stage and has so far only been applied to one SPH code, P-DEVA (Martinez-Serrano et al., 2008).

The plan of this chapter is as follows: In § 4.2 the P-DEVA SPH code which the GRASIL-3D code has been implemented on is explained, in § 4.3 the GRASIL-3D code itself is described, in § 4.4 the results of the combined codes are presented, the implications of these results are discussed in § 4.5 with ideas for further improvements. Some concluding remarks are given in § 4.6.

4.2 The SPH galaxy formation code

P-DEVA (Martinez-Serrano et al., 2008) is an OPEN-MP parallel version of the DEVA code (Serna, Dominguez-Tenrerio & Saiz, 2003), that incorporates a chemical algorithm including gas restitution, as well as a metal-dependent cooling function. All details of the code can be found in the two papers and references within. Only a brief overview, particularly highlighting the points necessary for the calculation of the SED, will be given here.

P-DEVA follows the formation and evolution of galaxies from primordial fluctuations to the objects we observe today, in a self-consistent manner, providing at each time step the structural and dynamic properties of all the galaxies constituents (dark matter, stars and gas). The gravity equations are solved using a Lagrangian AP3M-like technique and hydrodynamics with a SPH technique with individual time steps. Special attention has been paid to conservation laws, including angular momentum conservation.

The basic idea of the SPH method (Lucy 1977; Gingold & Monaghan 1977) lies in representing the fluid elements by particles which can be used in order to solve the hydrodynamical equations. At any time step the particles act as interpolation centres so that the local values of any macroscopic variable can be determined. In order to smooth out local statistical fluctuations, this interpolation is performed by convolving with a smoothing (or kernel) function.

In order to achieve high resolution galactic outputs within a cosmological framework it is necessary to run the code twice. As a first step, high-resolution initial conditions are generated in a cosmological box, for the virtual galaxy analysed in this thesis this was a box of 10 Mpc. These conditions are then degraded and a full simulation is performed at this lower resolution within a concordance cosmological model. At the end of the simulation several galaxy like objects can be identified and a suitable galaxy can then be selected for a more detailed study, the choice depending on the desired criteria. The particles inside the virial radius are then traced back until the initial redshift z_{init}. The complex hull (Barber et al. 1996) is calculated and any particles inside this hull are replaced by their high resolution counterparts. Gas particles outside the complex hull are eliminated and their mass added to the low-resolution dark matter component. In such a way initial conditions are obtained which allow for a high resolution simulation for a galaxy that has a full history of mergers and accretion in a cosmological context, without any assumptions made for their initial conditions beyond the cosmology and initial conditions generator used (Prunet et al. 2008).

Within this framework the content of the galaxy is sampled by a discrete number of particles both of dark matter and baryons. Each baryonic particle can be either in the form of gas or a stellar particle. A chemical evolution model is then implemented to compute the evolution of the nature of the baryonic particles at any time step. Namely i) when and how gas particles are turned into stars, ii) when and how stellar particles are turned into gas, iii) the metal production of each stellar particle over a time step Δt and iv) how these metals are released and mixed through the gas component of the galaxy. Details of all these processes are given in Martinez-Serrano et al., (2008).

4.3 Implementation of dust effects

The simulation specifies the position and velocity of all the particles of dark matter, gas and stars. In addition for each of the gas particles a metallicity z_g and a temperature T_g is known and for each of the stellar particles a metallicity z_* and an age t_* is known. The new code, GRASIL-3D, is then required to take these outputs and use them to calculate

SEDs at different positions within the galaxy and at different viewing angles which can then be compared to observations.

4.3.1 Charging the grid

GRASIL-3D works using a grid formulism. Specifically the whole galaxy is divided into a user specified number of equally sized grid cells, in the form of cubes. Each grid cell is assumed to have a constant density of gas, dust and stars throughout the cell. These densities can be derived from the particle positions calculated by the P-DEVA code. The GRASIL-3D code only requires knowledge about the cold baryonic particles, that is, stars and cold gas, so these are the only densities calculated.

Following the GRASIL formulism (§ 1.5) the gas needs to be divided up into either diffuse cirrus gas or dense molecular gas associated with molecular clouds. While the stellar component is divided into young stars, located in molecular clouds y_* and older, "free" stars f_*.

Stellar component

Each stellar particle is labeled as representing either young stars or free stars depending on if the stellar particle is older than the escape timescale t_{esc}. This quantity has a similar meaning to the GRASIL parameter of the same name, and is a free parameter of the model, the choice of this parameter is discussed in more detail in § 4.3.5. After each stellar particle has been identified as either young or free, the densities of y_* and f_* in each grid cell can be calculated for both using the SPH technique (see appendix A.1).

In addition the intrinsic SED in each cell due to both young stars and free stars is determined. Each particle is treated as an SSP and since the metallicity and age of every particle is known its SED can be calculated using the population synthesis method, in this case the Bruzal & Charlot (2003) stellar libraries are used (apart from the SSPs themselves the method for this is identical to that described in § 1.5.1, equation 1.1). The relative contribution of each of the stellar particles to the surrounding cells can be calculated using the SPH technique and the total SEDs of all the stars in each of the grid cells for both young and free cells can be obtained by summing over all the particles.

Gas Component

In order to calculate the mass of the cirrus and molecular cloud components in each grid cell, first the contribution to the two different gas phases at the location of each of the gas particles is ascertained. To do this it is necessary to calculate the ratio of molecular gas to total gas, f_{mc} for each particle, where:

$$f_{mc}(\vec{r},t) = \rho_{mc}(\vec{r},t)/\rho_{gas}(\vec{r},t) \tag{4.1}$$

where: $\rho_{mc}(\vec{r},t)$ is the density of just the molecular gas component at the position of the gas particle, and $\rho_{gas}(\vec{r},t)$ is the density of all the gas at the position of the gas particle.

This ratio can be calculated from a theoretical probability distribution function (PDF) assuming that cold gas with a density greater than $\rho_{mc,thres}$ is in the form of molecular gas. This is done following the work of Elmegreen 2002 and Wada & Norman 2007, details of which can be found in Appendix A.2. This method for the calculation of $f_{mc}(\vec{r},t)$ contains three free parameters: $\rho_{mc,thres}$, and two parameters which specify the PDF σ and ρ_0. More details of these parameters can be found in § 4.3.5.

The mass contribution of each particle to the cirrus phase can then be calculated simply by:

$$M_{cirrus} = M_{gas\ particle}\ (1 - f_{mc}) \tag{4.2}$$

The SPH technique described in appendix A.1 can then be used to calculate the density of cirrus gas in each grid cell, as well as its metallicity.

The density of molecular gas in each grid cell could be calculated in a similar way, by applying the SPH technique to the molecular gas contribution of each gas particle. This however could result in un-physical grid cells which have young stars but no molecular gas. As a result we decided to share the molecular gas in such a way that it is proportional to the density of young stars. First the total mass in molecular gas, M_{mc}, in the whole galaxy is calculated:

$$M_{mc} = \sum_{i=1}^{N} f_{mc,i} \times M_{gas,i} \tag{4.3}$$

where N is the total number of gas particles, $f_{mc,i}$ is the molecular gas fraction of the i-th particle and $M_{gas,i}$ is the particles mass.

Then for grid cell, $\vec{k}$, the molecular gas mass inside is:

$$m_{mc,\vec{k}} = V_{\vec{k}} \times \alpha \times \rho_{y*,\vec{k}} \tag{4.4}$$

where:

$$\alpha = M_{mc}/M_{y*} \tag{4.5}$$

where $V_{\vec{k}}$ is the volume of the grid cell and M_{mc} and M_{y*} are the total mass of molecular gas and young stars respectively summed over the whole galaxy.

Dust Component

Once the gas density in each cell has been determined it is possible to calculate the density of dust in each cell by assuming a dust-to-gas ratio, δ.

One possible approach would be to assume a constant dust-to-gas ratio equal to that of the Milky Way, $\delta = 1/110$. This may be a reasonable approximation for Milky Way type galaxies in the local universe but it is has been found that the dust-to-gas ratio in galaxies of different type and at different evolutionary stages varies, with a strong dependence on the chemistry of the ISM (e.g. Draine et al 2007).

A simple way to incorporate this, is to assume a linear dependence of the dust-to-gas ratio in each cell with the metallicity of the gas in that cell, i.e. $\delta \propto Z$ normalised so that $\delta = 1/110$ for $z = z_{\odot}$ as first suggested by Dwek 1998. Since the density of cirrus gas and its metallicity has been calculated in each grid cell, this is straight forward to calculate for the cirrus phase. Due to how the molecular gas has been allocated to the individual cells, however, each cell has no unique value for the molecular gas metallicity. Instead the average metallicity of the young stars in the cell can be used, since these will represent the metallicity of the gas at the time in which the molecular clouds form.

The assumption that δ scales with metallicity, although an improvement on a constant δ, is still an over simplification of a complex scenario and could lead to possible errors. This topic has been explored in some depth in chapter 2, with the use of detailed chemical evolution models.

Placing the young stars in the molecular clouds

The techniques described above provide for a grid cell $\vec{k}$, a density of molecular gas $\rho_{mc,\vec{k}}$ with an associated density of dust and a combined SED for all of the young stars $j_{\lambda,y*,\vec{k}}$. To convert these densities into a number of physically realistic molecular clouds, we split the gas into a number of molecular clouds N_{mc}, with the assumption that all the molecular clouds will have an identical mass M_{mc} with a radius R_{mc} (the choice of these parameters is discussed in § 4.3.5), where:

$$N_{mc} = \frac{V_{\vec{k}} \times \rho_{mc,\vec{k}}}{M_{mc}} \tag{4.6}$$

The SED of young stars inside each molecular cloud is then:

$$j_{y*,mc} = \frac{j_{y*,\vec{k}}}{N_{mc}} \tag{4.7}$$

The radiation transfer through each molecular cloud can then be calculated and the total emissivity recovered by multiplying by N_{mc}. In such a way even if there is not enough gas to form a molecular cloud, the radiative transfer of the intrinsic young stars SED is still calculated through a physically realistic cloud, and the final SED re-scaled appropriately.

4.3.2 Dust Composition and properties

The dust mixture used for the diffuse ISM is that proposed by Weingartner & Draine (2001) , (described in § 1.1.5, size distribution shown in figure 1.6), in which the dust is in the form of silicates and graphite grains, when the graphite grains are small they take the form of PAH molecules. The optical properties of the grains have been computed using Mie theory, the Rayleigh-Gans approximation and geometric optics as described in Laor & Draine (1993). Specifically we used the absorption and scattering efficiencies of graphite and silicate grains computed by B.T. Draine for 81 grain sizes from 0.001 to $10\mu m$ in logarithmic steps $\Delta loga = 0.05$, and made available via anonymous ftp at *astro.princeton.edu*. When the graphite grains are smaller then $0.01\mu m$ the tabulated cross sections for the PAH-graphite mix found at the same link is used instead. The PAHs in the diffuse cirrus will consist of a mixture of neutral and ionized particles, the ionization fraction will depend on the gas

temperature, the electron density and the ultraviolet field (Weingartner & Draine 2001b). In this work the ionization fraction suggested by Li & Draine 2001 is followed (the solid line, figure 7 p.26) which was estimated to be an average balance for the diffuse ISM of the Milky Way.

For the size distribution of the dust grains within the dense molecular clouds we have decided to use the same composition as that used by the GRASIL code originally described in S98 and § 1.5 of this work. The molecular clouds within the GRASIL code have been shown to give good fits to large star forming regions (S98), and the GRASIL code has been used successfully to fit actively star-forming galaxies and ultra-luminous infrared galaxies (ULIRGS), which are thought to be dominated by molecular clouds, (S98 and in particular Vega 2005). It is also important to note that the abundance of PAHs of molecular clouds have been specifically tuned by Vega et al (2005) to agree with the MIR properties of a sample of local actively star-forming galaxies. Due to the extensive testing which the molecular clouds within GRASIL have received, the adoption of the dust composition used should therefore represent an excellent choice for inclusion in this work.

Dust Extinction: absorption and scattering

Once the dust composition and optical properties for the dust mixture have been decided it is then possible to calculate its absorbtion and scattering optical depths. This can be done by first calculating the dust mixture cross-section:

$$\sigma_\lambda = \int_{a_{min}}^{a_{max}} a^2 Q(a,\lambda) \frac{1}{n_H} \frac{dn}{da} da \ \ cm^2 \tag{4.8}$$

where $n_H[cm^{-3}]$ is the hydrogen number density and Q is either Q_{abs} the absorption efficiency, or Q_{sca} the scattering efficiency.

In practice to calculate the extinction from the specified mixture of dust-grains the grain size distribution has been discretised into N=30 logarithmic bins. The total absorption or scattering cross-section can then be calculated by summing together the contributions of all the different grain sizes with suitable weighting w_i applied, where, following Draine & Malhorta (1993):

$$\sigma_\lambda = \sum_{i=1}^{N} w_i Q(a_i,\lambda) \ \ cm^2 \tag{4.9}$$

$$w_i = \pi a_i^{-1} \int_{b_{i-1}}^{b_i} a^3 \frac{1}{n_H} \frac{dn}{da} da \ \ cm^2 \tag{4.10}$$

where $b_i = \sqrt{a_i a_{i+1}}$

It then follows that the optical depth of the dust mixture for absorption and scattering is:

$$\begin{aligned} \tau_{abs,\lambda} &= \sigma_{abs,\lambda} \int_l n_H dl \\ \tau_{sca,\lambda} &= \sigma_{sca,\lambda} \int_l n_H dl \end{aligned} \tag{4.11}$$

where l is the distance traveled along the light beam and n_H is the hydrogen density along the light beam. Specifically in this model the path of the light l is split up into a sum of contributions from each of the cells the light travels through. So that:

$$\begin{aligned} \tau_{abs,\lambda} &= \sum_{k=1}^{N_{cell}} \sigma_{abs,\lambda} \times n_{H,k} \times r(k) \\ \tau_{sca,\lambda} &= \sum_{k=1}^{N_{cell}} \sigma_{sca,\lambda} \times n_{H,k} \times r(k) \end{aligned} \tag{4.12}$$

where N_{cell} is the number of cells the light beam passes through, $n_{H,k}$ is the hydrogen density of cell k and r(k) is the distance traveled through the k-th cell.

Dust Emission model

The dust emission is calculated using the same discretised dust mixture as for the extinction. The total emission can be calculated by summing over all the dust bins and applying the weighting calculated by equation 4.10. The exact method used to calculate the emission of a single grain i is dependent on its radius, a_i.

If $a_i > a_{flu}$ the emission is computed assuming that the grains achieve thermal equilibrium, so that all grains of a given composition and radius emit as gray bodies at a single temperature:

$$\begin{aligned} j_\lambda^{big} &= \int_{a_{flu}}^{a_{max}} \pi a^2 Q_{abs}(a,\lambda) B_\lambda(T(a)) \frac{dn}{da} da \\ &= \sum_{i, a_i > a_{flu}} w_i Q_{abs}(a_i,\lambda) B_\lambda(T(a_i)) n_H \quad \frac{erg}{cm^3 s \ st \ \mathring{A}} \end{aligned} \tag{4.13}$$

Where $Q_{abs}(a,\lambda)$ is the absorption cross-section of a grain of radius a at a wavelength λ, w_i is the weighting for the contribution of a grain of radius a_i to the total, where, w_i is given by equation 4.10 and $B_\lambda(T(a))$ is a black body spectrum at temperature $T(a)$, where $T(A)$, is the equilibrium temperature. This can be calculated from the energy balance between absorption from the radiation field J_λ heating the grains and the emission;

$$\int Q_{abs}(a,\lambda)J_\lambda d\lambda = \int Q_{abs}(a,\lambda)B_\lambda(T(a))d\lambda \tag{4.14}$$

For smaller grains a single gray body spectrum has been found to be insufficient to model the emission. As first noted by Greenberg (1968) the small grains can be stochastically heated to temperatures much higher than the temperature that they would be expected to reach if they were in temperature equilibrium. Thus a more detailed calculation for the smaller grains is required. The specific treatment of small grains adopted in this model is the thermal-continuous method as described by Guhathakurta & Draine (1989), (for details see appendix A.3). This method was compared to the more precise thermal-discrete model and the exact-statistical model in Draine & Li (2001). Despite being substantially quicker, the thermal-continuous approach proved to give a good approximation to the calculated emission spectra, a finding supported by Piovan et al. (2006). As suggested by Li & Draine (2001) a_{flu} will be set to $250\mathring{A}$, since it has been found that only emission from grains above this radii can be approximated by a black body. Below a_{flu} for each size bin and composition a temperature distribution P(T) is computed following the thermal-continuous approach and then the emissivity is obtained by integrating over this distribution:

$$\begin{aligned} j_\lambda^{small} &= \int_{a_{min}}^{a_{flu}} \pi a^2 Q_{abs}(a,\lambda)\left(\int_{T_{min}}^{T_{max}} B_\lambda(T(a))P(T(a))dT\right)\frac{dn}{da}da \\ &= \sum_{i,a_i>a_{flu}} w_i Q_{abs}(a_i,\lambda)n_H \int_{T_{min}}^{T_{max}} B_\lambda(T(a))P(T(a))dT \ \frac{erg}{cm^3 s\ st\ \mathring{A}} \end{aligned} \tag{4.15}$$

The emission from PAHs for the diffuse cirrus component is calculated using the thermal-continuous method in the same way as for the small carbon and silicon grains. In the molecular clouds, the treatment of the absorption and emission processes for the PAH bands are calculated following a slightly different procedure, that described in S98 and Vega et al. (2005) but updated with the most up-to-date cross-sections outlined in Draine & Li (2007)

calculated using new laboratory data and spectroscopic data observed by the *spitzer space telescope*. This method is used for the molecular phase in order to keep the treatment of the molecular clouds identical to that which has already been used with considerable success in the GRASIL model.

4.3.3 Radiation transfer in molecular clouds and emerging spectrum

In our Galaxy virtually all the star-formation activity resides in dense molecular clouds, with the vast majority of the escaping light being emitted in the IR due to the high extinction by the dense dust present. In order to recreate this physically observed phenomenon, stars younger than a free parameter t_{esc} will all be located inside dense clouds of molecular gas and dust, as first proposed by S98. The radiation transfer through the molecular clouds within GRASIL-3D will be calculated using the same technique as that used for the molecular clouds in the original GRASIL code.

The starlight emitted from within the molecular cloud is approximated as a central source, the radiative transfer through the cloud is based on the radiative transfer code described by Granato & Danese (1994) and details of this treatment can be found in S99. We therefore summarise here only the main features, particularly those important to the implementation in the new code.

The radiation transfer is solved using the lambda-iteration method, a method which at each successive iteration calculates the local temperature of the dust grains from the radiation field of the previous iteration. In such a way the code converges on a value for the radiation field at all radii of the molecular cloud which will give the correct temperature for thermal equilibrium. The convergence is speeded up by following the prescriptions of Collison & Fix (1991) and by adopting spherical symmetry.

The considerably simplified geometry due to a single central power and spherical symmetry result in considerable decreases in computational time, however such a geometry is insufficient to match the complex system of randomly distributed hot spots and cooler regions observed in real molecular clouds and could lead to unrealistically hot dust spots in the centre of our clouds. A maximum inner edge temperature was introduced in S98 to compensate for this potentially higher temperature and the resulting scheme was shown to

be sufficient for the modelling of molecular clouds giving good fits to observed data.

The optical depth for molecular clouds in this scheme has been found to depend on only the mass, radius and dust-to-gas ratio of the clouds (S99), as given by:

$$\tau_{mc} \propto \delta \frac{M_{mc}}{R_{mc}^2} \tag{4.16}$$

Resulting in only one real free parameter for the whole molecular cloud scheme, given by M_{mc}/R_{mc}^2.

4.3.4 Radiation transfer through the diffuse cirrus

Before escaping the galaxy the light from free stars and from molecular clouds must first travel through the diffuse cirrus component. As in GRASIL two assumptions are introduced to simplify the radiative transfer through the diffuse dust, namely:

- The effect of dust self-absorption is ignored.
- The effect of UV-optical scattering is approximated by means of an effective optical depth, given by the geometrical mean of the absorption and extinction efficiencies, $\tau_{eff}^2 = \tau_a(\tau_a + \tau_s)$ (Rybicky & Lightman 1979, p.36).
- To simplify the radiative transfer through the diffuse dust a third assumption, namely that the heating of the molecular clouds by the ambient radiation field in the diffuse medium has been ignored.

Approximations that have been shown to give similar results when compared to the more rigorous monte carlo techniques of Witt et al (1992) and Ferrara et al (1999) in the majority of cases tested, see S99.

The galaxy is subdivided into N_{side}^3 small grid cells of volume V_i. Using the two assumptions stated above the local (angle averaged) radiation field in the i-th grid cell due to the extinguished emissions of the free stars and molecular clouds from all the other cells can be calculated:

$$J_{\lambda,i} = \sum_k \frac{V_k \ (j_{\lambda,k}^{mc} + j_{\lambda,k}^{*}) \ exp \ (-\tau_{eff}, \lambda(i,k))}{4\pi \ r^2(i,k)} \ \frac{erg}{cm^2 \ s \ st \ \mathring{A}} \tag{4.17}$$

where: ($j^{mc}_{\lambda,k}$ is the volume emissivity of molecular clouds in the k-th grid cell (see § 4.3.4) and $j^{*}_{\lambda,k}$) is the volume emissivity of free stars in the k-th grid cell calculated using stellar population synthesis models; $\tau_{eff}, \lambda(i,k))$ is the effective optical depth between the i-th and k-th grid cell, calculated using the approximation $\tau^2_{eff} = \tau_a(\tau_a + \tau_s)$ and the dust properties described in § 4.3.2; $r(i,k)$ is the effective distance between the i-th and k-th grid cell, this is normally taken as the distance between the centre of grid cell i to the centre of grid cell k, however for nearest neighbour cells this has proved to be an inadequate treatment and a more precise method is employed (see appendix A.4).

Once the local radiation field has been specified in the i-th cell, the emissivity of the cirrus dust within the cell, ($j^{c}_{\lambda,i}$, can be calculated following § 4.3.2. The volume emissivity of the i-th grid cell can then be written:

$$j_{\lambda,i} = j^{c}_{\lambda,i} + j^{mc}_{\lambda,i} + j^{*}_{\lambda,i} \quad \frac{erg}{cm^3\ s\ st\ \mathring{A}} \tag{4.18}$$

Finally the specific flux measured by an external observer in a given direction θ is derived a sum over all the grid cells of the galaxy of the extinguished emissivity of free stars, molecular clouds and diffuse cirrus dust:

$$F_\theta = 4\pi \sum_k V_k j_{\lambda,k}\ exp\ (-\tau_{eff,\lambda}(k,\theta)) \quad \frac{erg}{s\ \mathring{A}} \tag{4.19}$$

where $\tau_{eff,\lambda}(k,\lambda)$ is the optical thickness from the element k to the edge of the galaxy along the direction λ, calculated following § 4.3.2.

4.3.5 Free parameters of the model

The GRASIL-3D code contains several free parameters, dealing both with the transposing of the particle positions in the P-DEVA SPH code onto the grid, and the treatment of the dust properties. The meaning of the parameters, and the possible range of values each can take, will be discussed in turn.

Threshold density for molecular cloud formation: $\rho_{mc,thres}$

This parameter governs the formation of the molecular clouds, gas with densities above this value are said to form molecular clouds. It is taken to be fixed for any environment

and at every point in the galaxies evolution.

A threshold value is commonly used by numerical simulations of molecular clouds in order to determine what gas in the simulations forms into the clouds, these values are backed up by a large number observations of molecular clouds both from our own galaxy and also nearby galaxies. Values for this parameter used in recent simulations vary, for example $\rho_{mc,thres} = 100\ H\ cm^{-3}$ in Tasker & Tan (2009) and $\rho_{mc,thres} = 35\ H\ cm^{-3}$ in Ballesteros-Paredes, Hartmann & Vázquez-Semadeni (1999). An adequate range for this parameter is therefore taken to be $\rho_{mc,thres} \approx 10 - 100\ H\ cm^{-3}$

Parameters governing the log-normal pdf function: ρ_0 and σ

These two parameters are linked to the density of gas, which can be calculated using the SPH technique, via *equation A.6* and *equation A.12*. Hence it is convenient to fix one of the parameters, and then using the equations, calculate the value of the other. We decide to fix σ, treating it as a free parameter while determining ρ_0 from the gas density. Values for σ have been calculated to range from 2.36 to 3.012 in Wada & Norman 2007 and Tasker & Tan (2009) give $\sigma = 2.0$.

Between them, $\rho_{mc,thres}$,ρ_0 and σ control the calculation of f_{mc}, the proportion of the total gas in the galaxy in the form of molecular gas. A useful check for the choice of these parameters can be made by comparing the final calculated value for the galaxy with observed values. For example Obreschkow & Rawlings 2009, give the ratio as a function of the galaxy morphological type and gas mass (figures 4 & 5 in that paper).

The time young stars remain enshrouded in molecular clouds: t_{esc}

To simulate the dense conditions of the clouds in which the stars are born, stars younger than t_{esc} are placed inside molecular clouds. This parameter represents the time taken for stars, modelled in our scheme by an SSP to escape the molecular clouds. t_{esc} is likely to be of a similar timescale to that of the lifetime of the most massive stars, stars with masses equal to 100 $m_\odot$ to 10 $m_\odot$ with corresponding lifetimes 3 to 100 $Myrs$. In practice the timescale is likely to vary with the density of the surrounding ISM. For low-density environments like spiral galaxies, with low star formation rates, the lifetime is likely to be

nearer the lower end of the range, corresponding to that of the most massive supernovae in the SSP. While it is likely to be much closer to the longest value for a high-density environment like the star-forming central regions of starburst galaxies (Piovan et al. 2006).

The escape timescale was found to be a very important parameter of the GRASIL model. Typical values for this parameter were found by comparison to local observations in S98, yielding values between 2.5 and 8 $Myrs$ for normal spiral galaxies and between 18 and 53 $Myrs$ for starbursting galaxies. Although it should be noted that these values have a slightly different meaning than our t_{esc} in this model. In GRASIL the fraction of young stars located in molecular clouds is given by *equation 1.2*, where t_{esc} is a timescale controlling the gradual escape of the young stars from their birth clouds, whereas for simplicity in GRASIL-3D, t_{esc} is taken to be a straight cut-off where all stars older than t_{esc} are said to have escaped. The parameter t_{esc} in the GRASIL model should therefore correspond to values approximately 1.5 times larger than the value of t_{esc} in GRASIL-3D.

Parameters setting the geometry of the molecular clouds: R_{mc} and M_{mc}

These two parameters set the geometry of the molecular clouds and combine set the optical depth through *equation 4.16*. Taken in combination these two parameters only represent one free parameter M_{mc}/R_{mc}^2. Observational estimates from our Galaxy suggest typical values for these parameters of $M_{mc} \sim 10^5 - 10^6\ m_\odot$ and $R_{mc} \sim 10 - 50\ pc$. In order to match observed SEDs of local galaxies S98 set $M_{mc} = 10^6\ m_\odot$ and derived values of R_{mc} between 10.6 pc and 17 pc.

4.4 Testing the models with a galaxy generated by P-DEVA

4.4.1 Object Properties

GRASIL-3D has been applied to a galaxy calculated by the P-DEVA code, a large galaxy with a prominent gas disc with no clear morphological disruption, galaxy 6795 in Martinez-Serrano et al (2009). The position of the particles at a redshift of zero, as calculated by the P-DEVA code for this galaxy are shown in figure 4.1. Young stars are defined as those with $t/t_u > 0.66$ where t is the age of the galaxy when the stellar particle

Type of particle	Number of Particles	Total mass ($m_\odot$)
Cold Gas	3046	8.91e9
All stars	13341	3.90e10
Young stars	1610	4.71e9
Intermediate stars	3474	1.02e10
Old stars	8257	2.41e10

Table 4.1: Particle numbers and masses of the outputs of the P-DEVA SPH code at z=0.

was born and t_u is the age of the universe; intermediate aged stars are defined as those with $0.33 < t/t_u < 0.66$; old stars are defined as those with $t/t_u < 0.33$. This figure shows that the gas and young stars are concentrated along the disc whereas the older stars are more spread out. The details of the masses of the particles at a redshift of zero are found in table 4.1. The mass of one particle is 2924074 $m_\odot$ and there are 15,804 particles in the simulation. The star formation history of the galaxy is shown in figure 4.2

4.4.2 Choice for free parameters

$\rho_{mc,thres}$, ρ_0 and σ

Between them, these parameters control the fraction of gas which forms molecular clouds. As discussed in § 4.3.5, in total, the parameters ρ_0 and σ only constitute one real free parameter since only one has to be set, σ in this case, while the other can be calculated from the gas density of the system. Typical values for these parameters have been found to be $\sigma \sim 2.0 - 3.0$ and $\rho_{mc,thres} \sim 10 - 100\ H\ cm^{-3}$. From initial tests it became clear that using values in the middle of these ranges resulted in too much overall extinction in the galaxy, with the amount of reprocessing far greater than 50%, too high for a normal large spiral galaxy. Consequently values near the edges of these ranges were chosen: $\sigma = 3.0$ and $\rho_{mc,thres} = 10\ H\ cm^{-3}$. This choice of parameter yielded a value of $f_{mc} = 0.57$ which although higher than the average values reported by Obreschkow & Rawlings 2009, is still compatible with their observations. It is also a typical value as used in the GRASIL code. It is possible that the value of f_{mc} required by the code could be higher than is physically realistic in order to represent not just the amount of gas in molecular clouds but also a

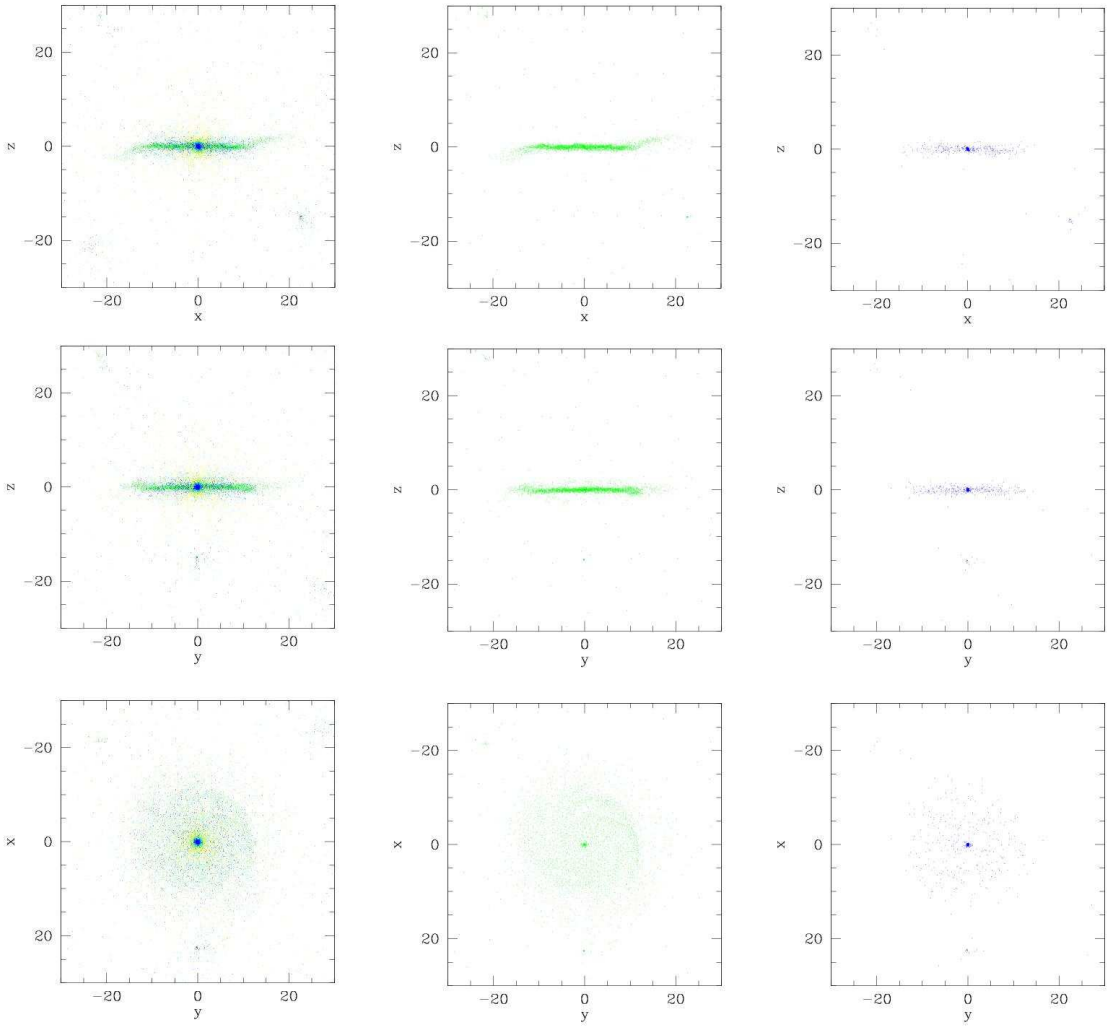

Figure 4.1: Plot showing the position of the particles calculated by the SPH code for three angles. All dimensions are in kpc. Colour code :: Green - gas particles; Yellow - young star particles; cyan - intermediate age stellar particles; Blue - young stellar particles. Left column shows all particles, central column shows only gas particles and right column only young stellar particles.

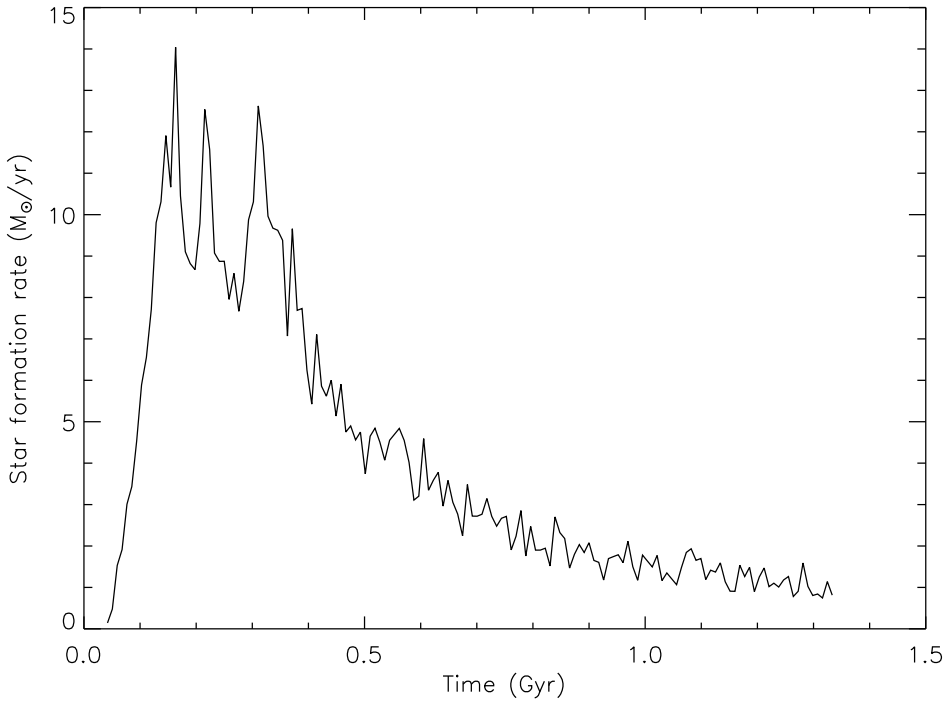

Figure 4.2: The Star formation history of the galaxy calculated by the SPH code

clumpiness in the rest of the ISM. A parameter that is commonly added by dust models in order to model the diffuse ISM, (see § 1.4).

t_{esc}, R_{mc} and M_{mc}

Since the part of the code which calculates the spectra for the molecular clouds is deliberately identical to that already used successfully in the GRASIL model, it is good idea to set these parameters to values currently used in the implementation of the GRASIL model. As discussed in § 4.3.5 typical values are $M_{mc} \sim 10^5 - 10^6\ m_\odot$ and $R_{mc} \sim 10 - 50$ *pc*. Following Granato et al. (2000) values of $M_{mc} = 10^6 M_\odot$ and R_{mc}=16 pc have been chosen.

As discussed in § 4.3.5 the value of t_{esc} in our model is likely to be 1.5 times larger than the parameter of the same name in the original GRASIL model. In Granato et al. (2000) a value of 2 $Myrs$ was chosen, accordingly a value of 3 $Myrs$ will be used for our model at a redshift of zero.

4.4.3 Results

The GRASIL-3D model as described in § 4.3 was applied to the galaxy generated by the P-DEVA code (§ 4.4.1), with free parameters given by § 4.4.2. The results of the code at a redshift of zero are shown in figure 4.3. For a grid with $55^3 = 166,375$ cells. The nearest neighbour factor, NN (see § A.4), is set to 0.475.

Figure 4.3 shows the overall SED of all the integrated light from the galaxy as viewed from two angles, face-on and edge-on. Also shown in this figure are SEDs showing the total light emitted by the stellar sources as would be viewed if there was no dust present, the emission spectrum of the molecular clouds and the emission spectrum of the diffuse cirrus.

The figure also shows the same SEDs of M51 generated in S98 in order to match observations. The SEDs are relatively similar. The main difference is that the cirrus spectrum in the GRASIL-3D models are stronger at $\sim 2 \times 10^5 \mathring{A}$, which probably indicates a stronger radiation field, maybe because of a more concentrated stellar and dust profile. Slightly more extinction is also observed in the GRASIL-3D models, probably due to the

larger ISM content relative to the stellar content (M_{gas}/M_{gas}=0.22 in the P-DEVA galaxy and M_{gas}/M_{gas}=0.12 in the GRASIL model of M51). Despite the differences though, the SEDs are similar enough to suggest that our SED is typical to that which one would expect for a large star-forming normal spiral galaxy, as expected.

Figure 4.4 and figure 4.5 show the resolved SED for our galaxy shown both edge-on and face-on. From the face-on SED it is clear that there are several distinct star forming regions within our galaxy, shown very clearly in the UV, these sources are concentrated into a narrow disc as can be seen in the edge-on plot, which is heavily extincted, due to the large quantity of dust concentrated in a thin disc. This is consistent with the position of the young stellar particles shown in figure 4.1. The optical and NIR spectral regions are believed to trace the intermediate and older stars and as expected in our model the strength of this emission is indeed consistent with the position of the older stars, as shown in figure 4.1. There is also a hint of a dust lane present particularly in the edge-on optical image, with the very centre of the disc less bright than its immediate surroundings, due to the higher extinction in the central plane. The MIR emission shows a similar distribution to that of the UV in both the face-on and edge-on visualisations, although without the extinction. This is a reflection of the fact the MIR emission follows closely the recent star formation, because the emission in this regime requires a strong radiation field only found near young stars. Two areas show up very brightly in the FIR/sub-mm and these show the location of the most recent star-formation which take the form of large molecular cloud complexes. It should be noted that because the radiation in molecular clouds in the GRASIL-3D model is highly extincted these two very bright areas are not especially bright in the UV as would otherwise be expected. The remainder of the FIR/sub-mm emission follows the location of the cold gas as can be seen between a comparison with both the edge-on and face-on visualisations and figure 4.1 hence the clear spiral arm pattern, most visible in the FIR, which can also be seen in the location of the gas particles.

A comparison can be made to observed images of M51 shown in figure 4.6, a nearby, face-on spiral galaxy. The images show some correlation; the UV observed image of M51 is concentrated on a few main star-forming regions in the centre of the galaxy and along the spiral arms, a similar pattern can be observed in the theoretical galaxy

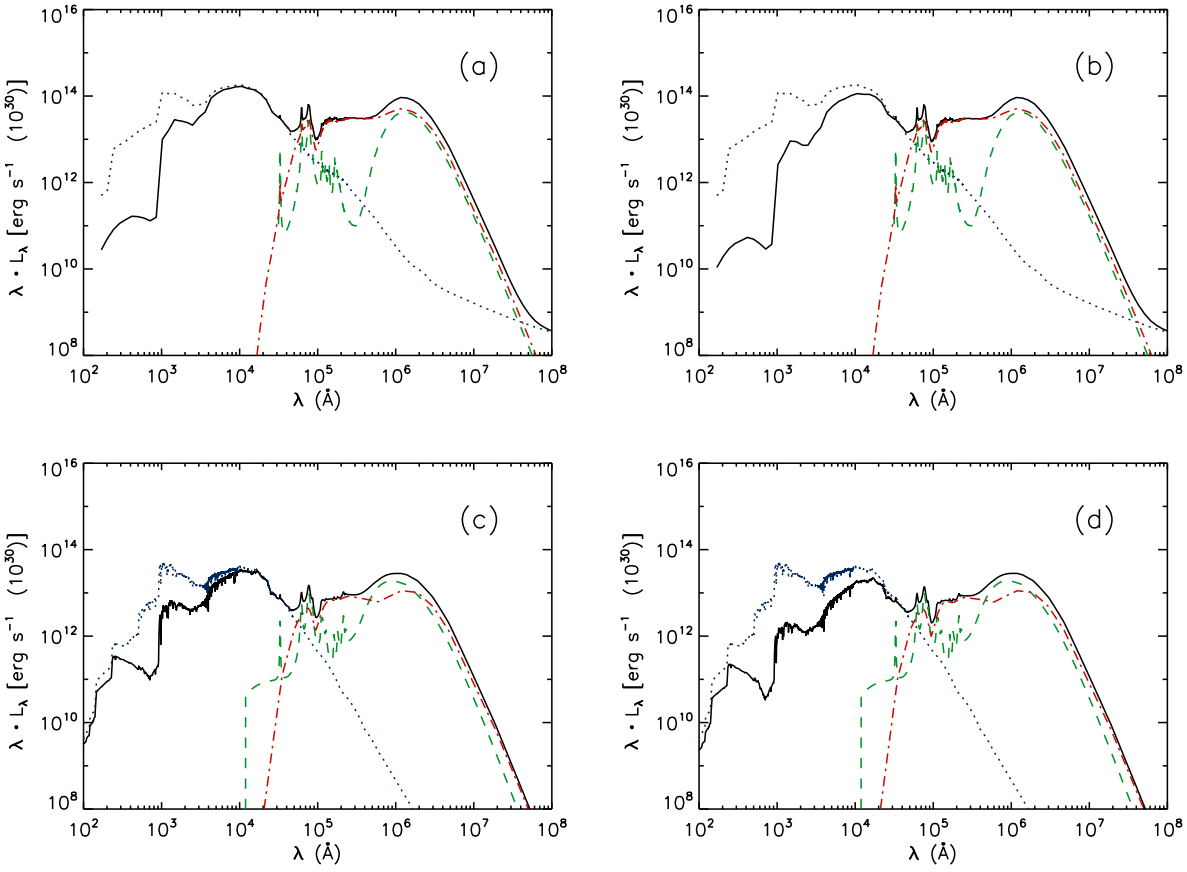

Figure 4.3: A comparison between the SEDs generated by GRASIL-3D to plots of a galaxy calculated by GRASIL. (a) face-on plot of M51 calculated by GRASIL (from S98); (b) edge-on plot of M51 calculated by GRASIL (from S98); (c) face-on plot of P-DEVA generated galaxy calculated by GRASIL-3D; (d) edge-on plot of P-DEVA generated galaxy calculated by GRASIL-3D. For all plots: Blue dotted light - un-attenuated stellar population (intrinsic SED); Green dashed line - emission from diffuse cirrus; Red dot-dashed line - emission for molecular clouds; Black solid line - Full SED.

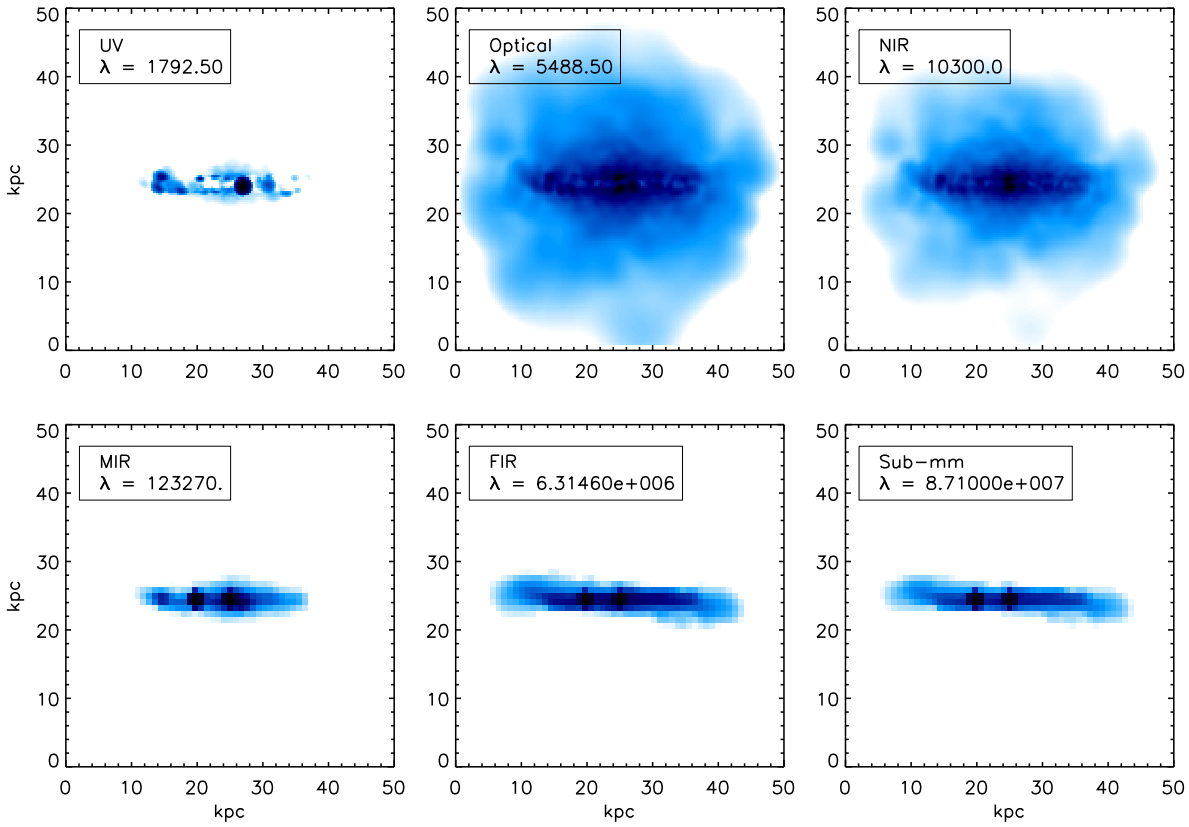

Figure 4.4: Face on images of the galaxy shown at different wavelengths. The colour is related to the intensity of the flux in the particular wavelength, with the scale going from white to dark blue. The colour scheme is logarithmic, with a range [maximum flux / 1e4 : maximum flux].

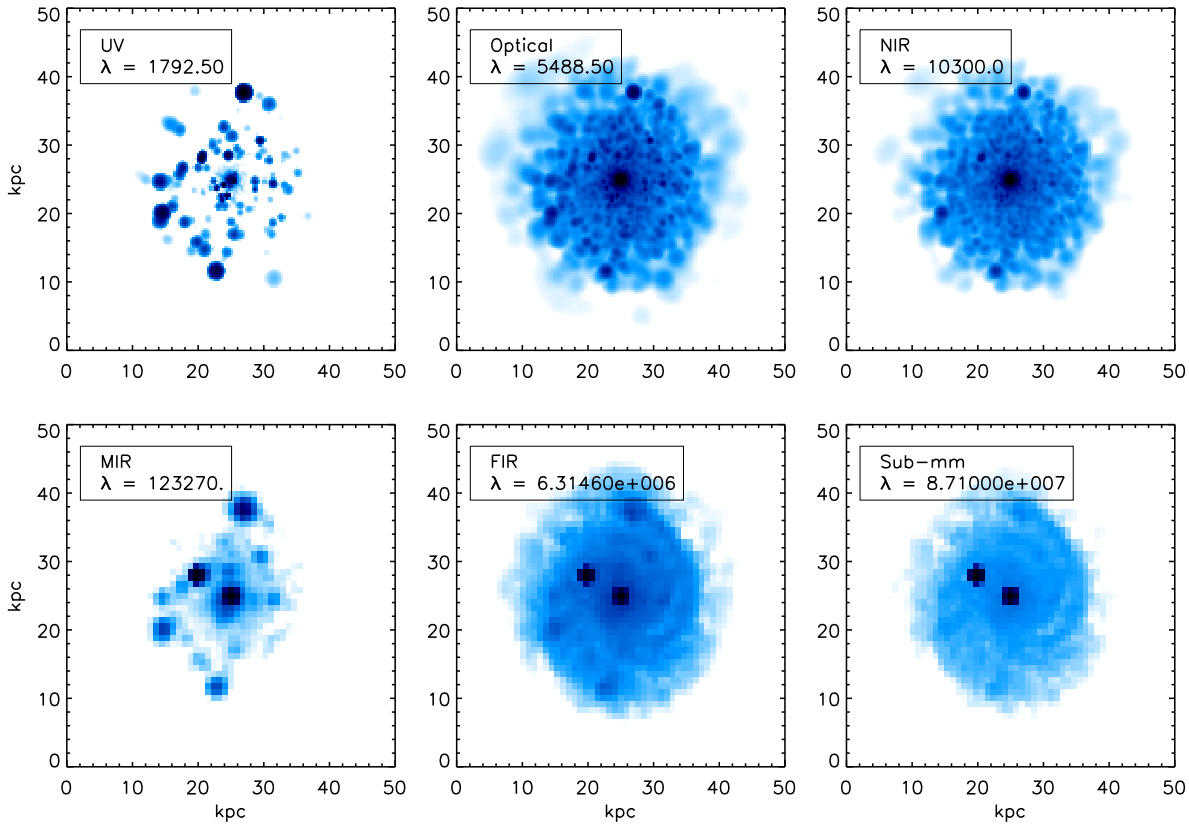

Figure 4.5: Face on images of the galaxy shown at different wavelengths. The colour is related to the intensity of the flux in the particular wavelength, with the scale going from white to dark blue. The colour scheme is logarithmic, with a range [maximum flux / 1e4 : maximum flux].

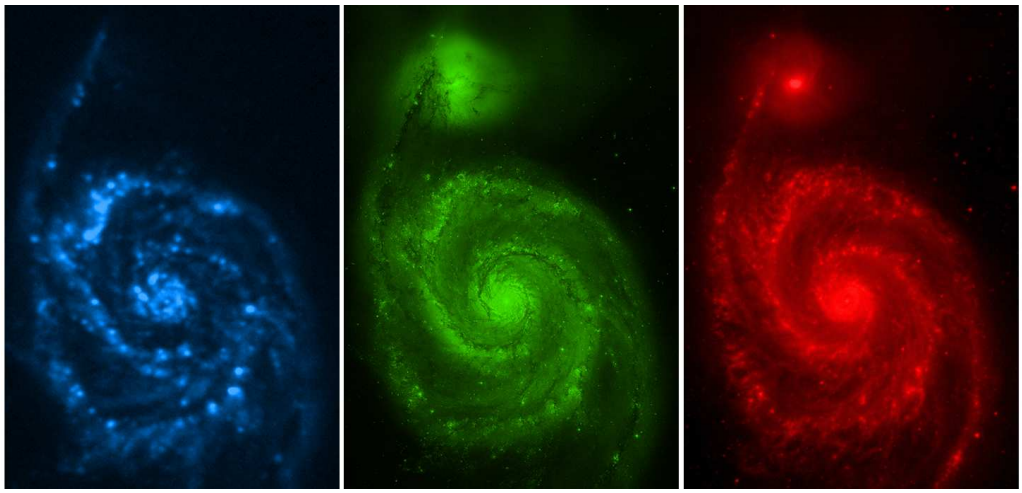

Figure 4.6: Images of the galaxy M51 (NGC 5194). a) FUV image taken by GALEX at 1530 $\mathring{A}$. b) optical image by Hubble space telescope. c) MIR image taken by spitzer at 8μm

image. The light from the observed optical image is more diffuse, while the MIR image is slightly more concentrated with several brighter regions, showing the location of star-formation complexes, in agreement with our theoretical image. For all three wavelengths our theoretical images are more patchy than the actual observed galaxy, but this is probably due to a lack of resolution in the SPH simulation, rather than a problem in the GRASIL-3D code.

SEDs have also been calculated at a redshift of 3.5 and a redshift of 2 and these are shown in figure 4.7. Both of these redshifts correspond to a peak of star formation, see figure 4.2, so at these times the escape timescale t_{esc} has been increased to 20 Myrs, in agreement with S98. As can be seen from figure 4.7 the amount of reprocessing at these times has increased, as can clearly be seen from the increased emission in the IR. To check that these SEDs are representative of galaxies observed at high redshift our theoretical galaxy SED at z=2 was compared to observed SCUBA galaxies from the SHADES sample (Clements et al 2008) with comparable redshifts, using the same technique as that described in § 2.3.4 and § 2.4.3. Good fits for four of the galaxies are shown in figure 4.8.

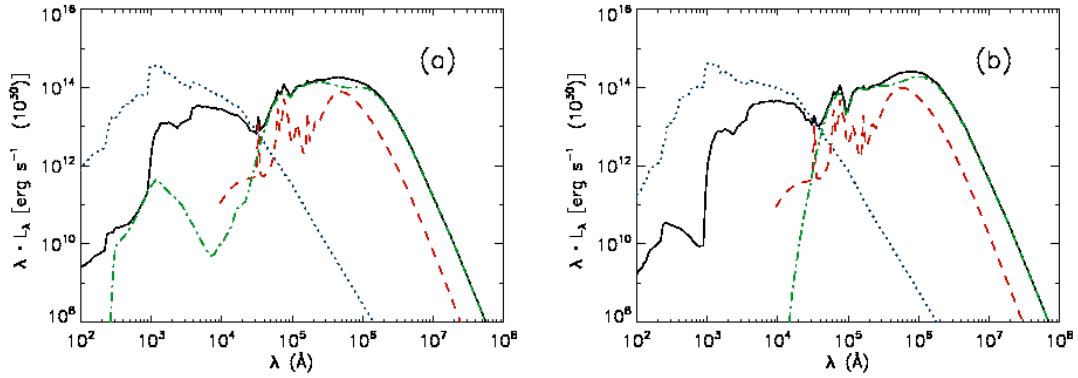

Figure 4.7: The angle-averaged SEDs generated by GRASIL-3D for the galaxy at a) a redshift of 3.5 and b) a redshift of 2: Blue dotted light - un-attenuated stellar population (intrinsic SED); Green dashed line - emission from diffuse cirrus; Red dot-dashed line - emission for molecular clouds; Black solid line - Full SED.

4.5 Discussion and future work

As has been show the model has produced some encouraging initial results when applied to one galaxy, generated by the P-DEVA code. The z=0 SED generated looks similar to that of M51 and the face-on image although lacking resolution, compares favorably to observations of the same galaxy. In addition SEDs produced for the galaxy at a redshift of 2 also compare favorably to observed SEDs of galaxies from the SHADES sample with a corresponding redshift.

This code is still however in the development stage and more work is needed in several areas, before a rigorous testing can be carried out.

4.5.1 Improvements needed for the model

Nearest neighbours

Perhaps the biggest problem with the model at the moment is the very imprecise method used to calculate the 26 other nearest neighbours. At the present time this is done by adjusting a factor NN in order to conserve the energy balance of the entire system. This method is slow since the factor must be manually tuned to the an appropriate value,

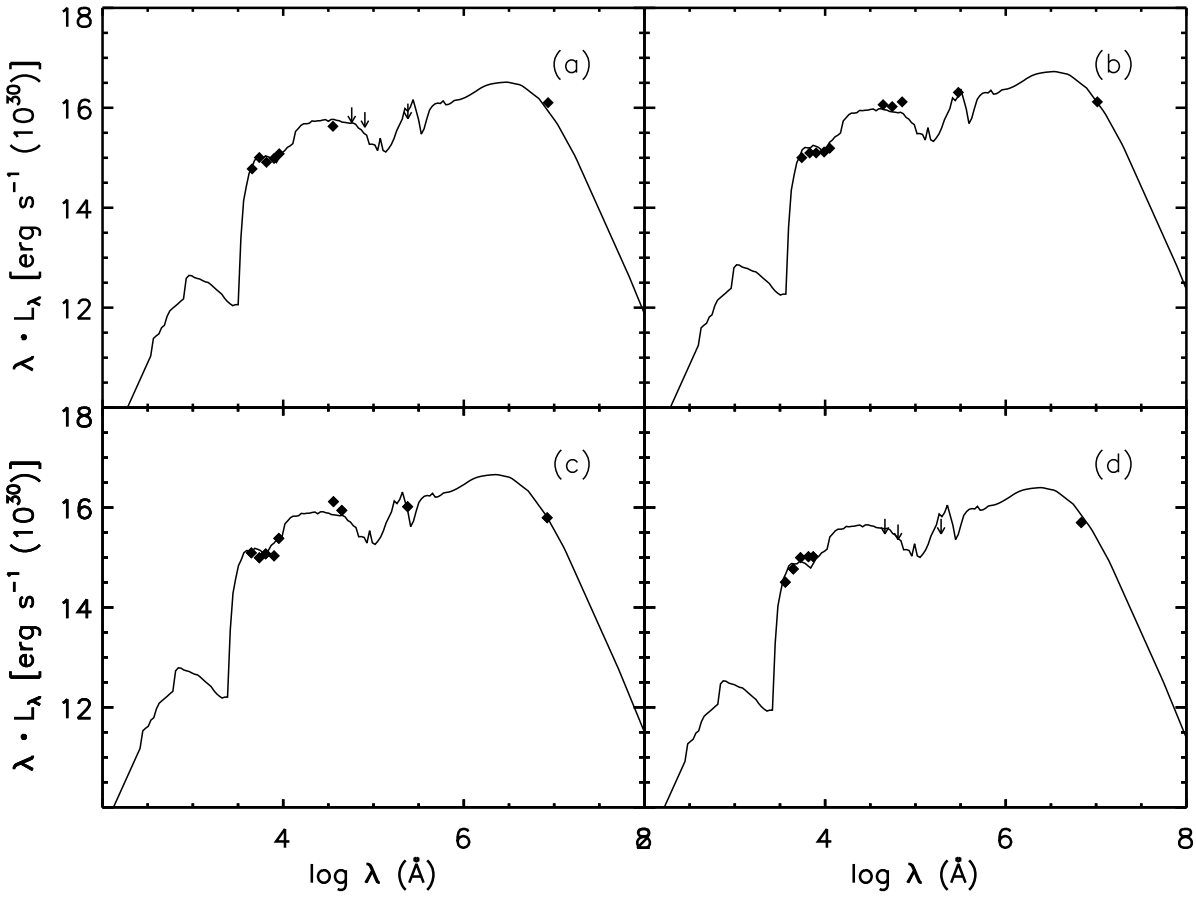

Figure 4.8: Comparison of the SED calculated for the galaxy at a redshift at z=2 with four SCUBA galaxies of the SHADES sample (Clements et al 2008). a) SHADES-SXDF 10, b) SHADES-SXDF 7, c) SHADES-SXDF 71, d) SHADES-SXDF 12

with the whole code having to be run with a different value of NN every time until the correct value is found. It is not even clear that this method is actually giving the correct answer any way. As a result in order for the code to be run on large samples of galaxies this method needs to be improved.

One possible approach would be to implement a similar method to that already used to calculate $R(i,i)$. It should be possible to develop a code which can calculate the amount of starlight absorbed by the central cell due to the radiation from each of the 26 nearest neighbour cells, possibly using a monte carlo technique. When the amount of energy absorbed from each of the cells is known it should then be possible to solve for $R(i,k)$, (where k is the position of the 26 nearest neighbours) by calculating an energy balance, in a similar way to that which has already been used to calculate $r(i,i)$.

This proposed method will be very computationally intensive and as it stands would be unsuitable for use in our code. However it is hoped that a dependence will be found between $R(i,k)$ and $\tau(i,k)$, where $\tau(i,k)$ is the optical depth between the central cell i and the nearest neighbour k, hence, removing the need for running the computation every time. Clearly much testing is required on all aspects of the nearest neighbour problem in order to develop a quick and robust method.

Adaptive resolution

As can be seen from figure A.3 in appendix A.5 the part of the code which takes the most time, after the full calculation of the nearest neighbours function, is the section of the code that calculates the radiation field. This is particularly true if the emission from fluctuating grains is not calculated (figure A.3b). The figure shows that the time required for this calculation increases rapidly with the number of cells in the grid. This is because the amount of calculations goes with $\sim N_{cell}^3$, because to calculate the radiation field for every grid cell requires knowledge of every other grid cell. As a result using this method restricts the possible number of grid cells with the time getting prohibitively larger as the grid spacing decreases. Presenting a real problem for our code for the calculation of the cirrus emission.

It is common in a galaxy model of this kind to use an adaptive grid technique,

where the density of the gas and stars increases the cells get finer and where the density is lower the resolution is larger. In such a way it could be possible to reduce the number of calculations needed and hence the time required to calculate the radiation field, while allowing for a higher resolution in the important parts of the galaxy. Due to nature of our code and the way in which the optical depth between cells is calculated however, such an approach is not possible.

Instead two different grids, one fine and one coarse could be adopted. Due to the $r(i,j)^2$ term in the denominator of *equation 4.17* it is known that the radiation field will be dominated by nearby sources. Therefore when calculating the radiation field it should be possible to use a finer grid to calculate the radiation for the nearer cells and a courser grid to calculate the emission from the rest of the cells. Such a method would allow for our code to reach higher resolutions without the need for calculating the radiation field on huge grids, thereby reducing the computation time significantly. In addition by only using the finer grid for cells with densities of cirrus gas above an appropriate threshold the time could be reduced further.

To illustrate the possible time saved by such a scheme, one could consider a galaxy in which two grids were used to calculate the radiation field, one with a resolution of 30 grid cells per side and one with a resolution of 100 grid cells per side. The course grid of 30 cells per side could be used to calculate the background radiation for all the cells and for roughly a third of these cells (those with the highest density of cirrus gas) the radiation field from their 8000 neighbouring cells could be calculated using the finer grid. Using times taken from figure A.3 the time needed for such a scheme would be ~ 1.25 CPU hours.

Improved SSPs

The SSPs we are currently using are those calculated by Bruzal & Charlot (2003). The stellar libraries used by this code are now slightly out of date, particularly the treatment of the AGB stars, (see e.g. Bruzual 2007; Marigo et al 2008). A more advanced set of SSPs should therefore be incorporated into our model, possibly either the updated treatment now being used in the GRASIL code (which also contain radio emission) or the updated Bruzual & Charlot code (Charlot & Bruzual in preparation). Such an improvement is likely to have

a small but noticeable effect in the intrinsic SED of the starlight, particularly in the NIR.

Improved PAH treatment

The PAH treatment currently incorporated within the GRASIL-3D code is that described in Li & Draine 2001. Since then, recent observations from the *spitzer* space telescope have substantially increased our knowledge of the various PAH bands (see Draine & Li (2007). The changes made to the optical properties of the PAH molecules described in this paper should be incorporated in our model. Such an update is only likely to have a noticeable effect in the emission bands observed in the MIR and will not change the overall shape of the SED.

Dust evolution

One potential source of error and an area for future work is in how the evolution of the dust grain population is modelled in our code. As described in § 4.3.3 the mass of dust in each cell is given by: $M_{dust} \propto M_{coldgas} \times z$, where z is the metallicity and the composition of the dust is always the same (based on Galactic observations, see § 4.3.2). The effect of introducing these assumptions was studied in depth in chapter 2, using less complex galaxy formation models, and the errors were found to be potentially large, particularly in galaxies of type different from the Milky Way and in young galaxies. By extending the chemical evolution calculations of the P-DEVA code to include the dust component, (using similar treatments, as described in § 2.2.2) it should be possible to improve the accuracy of the model. In addition the spatial resolution of the SPH code should represent an ideal test-bed for an improved study of dust evolution in different regions of a galaxy. Allowing for the study of the evolution of the dust grain population in different environments within the same galaxy.

4.5.2 Testing

So far our model has been used to calculate an SED for one galaxy generated by the P-DEVA code with encouraging results. The next step, after the introduction of the improvements outlined in the previous section, is a rigorous testing of our model. This

should largely focus on two main areas: the comparison of our model to the results of other codes, and the calculation of the SEDs for more galaxies with comparisons to observations.

A first step towards testing the code would be a comparison with a galaxy SED calculated by GRASIL, with the same galactic inputs for both models. The GRASIL code, has been well tested itself, and is known to reliably reproduce the SED of all but the most extreme galaxies, therefore if our code can reproduce the SED of a GRASIL galaxy, it would be a good step to proving the reliability of our code. Due to the similarities between the two codes, in addition to our possession and understanding of both source codes, such a test should be relatively simple and any differences found easily comprehensible. A typical benchmark study undertaken by other galactic SED codes, (e.g. Bianchi 2008; Jonsson et al 2009) is a comparison to the 2D radiative transfer problem of Pascucci et al. (2004), which represents a radiative transfer from a point like source in the middle of an axially symmetric disc. The radiative transfer is calculated for four optical depths and at three viewing angles. A comparison of results calculated with GRASIL-3D with the results published in this work should represent an additional important test for our code.

Our model should also be applied to other objects generated by the P-DEVA code. Running the code on a variety of different galaxies should allow for a meaningful comparison with observations. Of particular interest would be objects with very different properties to the galaxy currently studied. An example of this would be a large galaxy forming at a high-redshift. Such a galaxy is likely to have very different properties: higher star-formation rates and therefore more stars in molecular clouds, higher densities of gas and dust with a more irregular geometry. Such a galaxy would represent a challenge for our code and it is important to be able to demonstrate that our model can cope with such scenarios. It is also important in order to gain an improved insight into the values of the free parameters of our model. It is vital that before tackling large samples of galaxies these parameters can be fixed to typical values. It is certainly an advantage that all the parameters of the model have a physical meaning and are therefore not truly 'free', so that the parameters are restricted to a small range of physically realistic values. Only by running the model with different galactic inputs with a careful comparison to observations can typical values within these ranges be chosen.

The goal is to develop a code which can be used with the outputs of any hydrodynamical code so ultimately once the code has been run successfully for many different galaxies generated by the P-DEVA it would be good if the GRASIL-3D code could be made accessible to be run on other group's hydrodynamical simulations. Such a situation would require the improvement of the codes interface so that it is easy and clear for other people to use.

4.5.3 Properties of the model

For wavelengths less than about $5\mu m$, the emission from dust will be negligible, hence to calculate a SED for these wavelengths it is not necessary to take into account dust emission, allowing for lower CPU times. From figure A.3c it can be seen that our code can calculate the UV to NIR spectrum of galaxies in very short timescales, allowing a SED to be calculated for this region in $\sim$ an hour using a single CPU. This quick time is also due to the scattering approximation used in the code, which allows the radiative transfer equations to be solved very quickly. As such our code should be very useful when a fast solution for this region is required. There will be some inaccuracies introduced by the scattering approximation, particularly in high optical depth environments, however it should be noted that for the highest optical depth regions, the molecular clouds, the full radiative transfer is performed.

At wavelengths greater than about $5\mu m$ the emission from dust grains starts becoming important and as a result the CPU times required by the code increase substantially, see figure A.3a,b, due almost entirely to the calculation of the cirrus emission. These timings for this calculation are dominated by two different tasks: the calculation of the radiation field; and the calculation of the dust emission, given this radiation field. The time taken for the second task, the calculation of the emission, differs greatly depending on whether the emission of fluctuating grains is calculated, as can be seen by a comparison between figures A.3a and b. The emission by thermally fluctuating grains (see § 4.3.2), affects the SED mainly in the MIR range of the spectra. This is shown in figure 4.9, which displays a comparison between an SED calculated by GRASIL-3D for the P-DEVA galaxy with and without the calculation of fluctuating grains in the cirrus component, the FIR spectra for

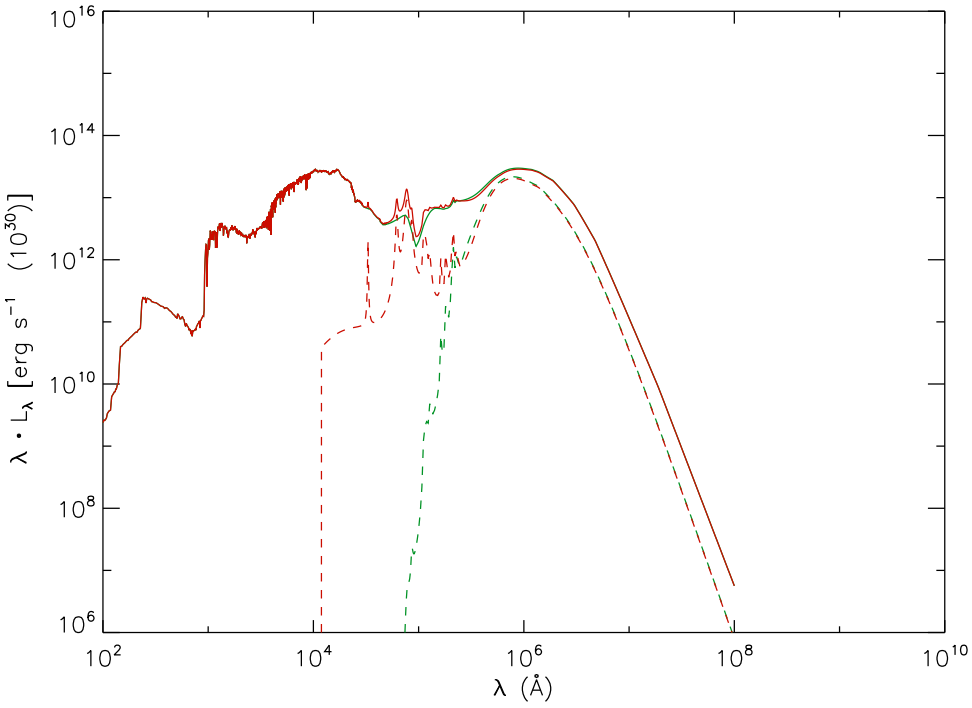

Figure 4.9: Graph showing the effect plots with fluctuating grains in the cirrus in red, and without fluctuating grains in the cirrus in green. Dashed lines: just cirrus emission. Solid lines: Total SED.

both SEDs is predominately unchanged, the cirrus SED in the MIR however is underproduced if no fluctuating grain is followed. In this example, as in many star-forming galaxies, the MIR is dominated by emission by molecular clouds, which still include the calculation from fluctuating grains, so consequently the effect of ignoring the fluctuating grains in the cirrus is greatly reduced. Other authors (e.g. Jonsson et al 2009) have used a template approach for the calculation of the fluctuating grains and this can be used to approximate the MIR wavelength region without the expensive computation.

As can be seen from figure A.3a and b, at high resolutions, regardless of the method used to calculate the dust emission, the calculation of the radiation field will be the computational bottleneck. This means that at present, aside from the important role of testing the code, our model will not be that efficient at calculating SEDs in the MIR to sub-mm wavelength region, particularly since the time taken to calculate the SEDs will

be comparable or worse than existing Monte Carlo codes which perform a more accurate computation. When, however, the adaptive grid improvement described in the previous section is implemented, the situation should change. This is particularly true for the no-fluctuating grain case, where our code should be capable of producing a full wavelength SED at a reasonable resolution, in about 1-2 CPU hours, making it a useful choice as a quick alternative to the more computationally expensive Monte Carlo codes.

4.6 Summary

Based on the main concepts already used in the GRASIL model, we have written an entirely new model, GRASIL-3D, which unlike the original GRASIL model, allows for an arbitrary choice for the 3D geometry of the stars and dust. The model also improves on several other areas, most notably using an updated dust grain size distribution for the cirrus, the "Draine" bare silicate-graphite model, described in § 1.1.5.

This model has been interfaced with a SPH code, P-DEVA, with the SPH particles used to calculate densities of the stars and dust in all the grid cells. The intrinsic SED for each of these stellar particles is calculated using a stellar population synthesis library. Following the GRASIL formulism, the stars are either said to be "young" stars, which are still radiating inside their dense molecular birth clouds, or "free" stars, which have escaped their molecular clouds. The gas particles are divided into diffuse cirrus gas and molecular gas, with the ratio being calculated from a theoretical probability distribution function (PDF). The total mass in molecular gas is divided between cells which contain "young" stars and split up into molecular clouds, with masses and radii governed by free parameters. The radiative transfer through the molecular clouds and diffuse cirrus is then calculated following a similar treatment to that already used in the GRASIL model. Areas still needed for improvement of the code have been identified, in particular, implementing an adaptive grid and a better treatment of the nearest neighbour problem.

SEDs have been calculated for a large gaseous spiral galaxy generated by the P-DEVA code and SEDs for two directions as well as the corresponding 2D images at several wavelengths have been presented for a redshift of 0. In addition SEDs have also been

calculated for the galaxy at a redshift of 2 and 3.5. Since the galaxy was not calculated to correspond to any one actual galaxy a direct comparison to observations is not possible, however it has been noted that the z=0 SED looks remarkably similar to an SED calculated by S98 to match observations of M51 and the 2D face-on image shows similarities to actual observed images of M51. In addition the z=2 SED has been shown to provide good fits to SCUBA galaxies at corresponding redshifts. These tests, although relatively weak, suggest that our code is performing reasonably. The next step, after the improvements have been implemented, is a more rigorous testing of the model both against existing codes, in addition to a comparison of SEDs calculated for a number of theoretical galaxies, against observed galaxies.

At present the code performs very quickly in calculating an SED from the UV to the NIR. The dust emission part of the code however is very computationally expensive but it is hoped that with the improvements the performance of this part of the code can be substantially improved, resulting in a quick galaxy-dust model which can calculate an SED from the UV to the radio.

Chapter 5

Concluding Remarks

The GRASIL code, developed over ten years ago, has proved to be a very useful tool into the study of galaxies. Both to disentangle the large quantity of useful information in the observed SED of galaxies, and to allow galaxy formation models to compare their predictions to real observations. Like all tools however GRASIL has it limitations. This thesis has examined these limitations and has proposed improvements and extensions to the code. A separate conclusion has been included at the end of every chapter, so only a brief summary of the whole thesis will be presented here.

5.1 Summary of Results

In the GRASIL model, as in all models which compute the SED of galaxies, the evolution of the dust component has not previously been followed, due to the complexities that this would introduce into the code. Usually the chemical properties of the dust grain population are assumed to be identical to that observed in the Milky Way, in all times and in all environments. Additionally the dust mass is typically approximated by assuming a dust-to-gas ratio proportional to the metallicity. In **chapter 2** the use of these assumptions is investigated.

In this section a chemical evolution model which includes a detailed calculation of the evolution of the dust grain population has been combined with the GRASIL code in order to calculate the SEDs for galaxies of three different morphological type: spiral, irregular

and elliptical. Both the information provided by the chemical evolution code for the stellar evolution of the galaxy e.g. the star-formation history and IMF, as well as the calculated dust properties for the galaxies are used. The SEDs have been compared to observations both in the local universe and at high-redshift and the theoretical galaxies have been shown to be representative of real galaxies of corresponding morphological type. In order to ascertain the importance of following the dust evolution and the potential errors which could be introduced in the normal usage of GRASIL, SEDs were also generated of the same galaxies but using the normal dust assumptions typically used. A comparison of the SEDs calculated using the two methods has been presented and it has been concluded that by using the typical dust assumptions for Milky Way type spiral galaxies the likely errors introduced are small, although they could increase with redshift. Introducing the approximations (which have been tuned on spiral galaxies), into galaxies of different morphological type (in this work irregular and elliptical galaxies) has been shown to be potentially dangerous with large possible errors. Of the two assumptions it has been found that the largest errors are likely to come from assuming that the dust-to-gas ratio scales with the metallicity. Although not explicitly calculated by the dust evolution model, the dust size distribution has also been shown to be an important factor, particularly at high redshift. In this work the implementation of the evolving dust grain population has been introduced only into one galaxy model, GRASIL, the results presented here, though, should be equally applicable to any other model.

Due to its unique properties the GRASIL model has been combined with several SAM galaxy formation codes in order to calculate multi-wavelength SEDs which can be compared to observations. Despite being a relatively quick spectrophotometric model the computation of the SED in these combined codes has often been found to be the computational bottleneck, preventing the calculation of the millions of SEDs needed to compare to large observational surveys. In **chapter 3** we discussed the implementation of an artificial neural network (ANN) into the GRASIL code, which is designed to significantly reduce the computational time required to calculate the SED of one galaxy. We have presented encouraging results obtained by the application of the ANN both for single galaxies and for large statistical samples, and conclude that the computation of SEDs with the ANN

method appears robust and computationally advantageous, with CPU gains of more than 2 orders of magnitude, and should therefore be ideal to analyse and test galaxy formation models.

One of the main strengths of the GRASIL model is the choice of galactic profile, either a bulge, a disc, or both, which has introduced the flexibility necessary to be able to model a wide variety of galactic types, while the axisymmetry of the profile allows the computation to be performed quickly. There are however occasions when it would be beneficial to be able to specify an arbitrary geometry for the stars and gas, such as when interfacing the code with hydrodynamic galaxy simulations. In **Chapter 4** we described an entirely new galaxy SED model. GRASIL-3D which adopts the main formulism of the GRASIL code but allows for the specification of an arbitrary geometry for the stars and dust. This new model has been combined with an SPH code, P-DEVA, and initial results for a gas-rich spiral galaxy have been presented.

5.2 Future Work

The field of dust modelling is indeed a "trendy" subject and there are many possibilities which exist for further work in this area. New observations in the IR allow for unprecedented sensitivity in this region of the electromagnetic spectrum, and provide much information as to the properties and location of dust in galaxies. In particular the recent launch of the European Space Agencys (ESA) Herschel Space Observatory will soon be opening up an entirely new window into the dusty universe, particularly at high-redshift. In addition, the realisation that dust reprocessing is a very important, complex process has increased the demand for accurate and quick dust models which can be interfaced to galaxy formation codes: - it is certainly an exciting time to be working in this field.

More specifically, future opportunities exist for all three of the projects covered in this thesis:

- The work described in chapter 2, would be highly useful as the basis for the study of the high redshift universe, where dust reprocessing and the evolution of dust are likely to be important factors. Models have been presented which gives good fits to SCUBA

galaxies as well as post-starburst galaxies, which shows that our combined model is producing reliable results. Building on this work it should be possible to create a library of high redshift galactic SEDs which could be used to determine information from high redshift observational surveys determining an objects redshift, as well as other properties such as mass starformation rate and starformation history. It should also be possible to use the models to do a careful analysis of interesting single objects, such as the quasar SDSS J1148+5251 (see e.g. Dwek 2007).

Another interesting topic for further study would be the study of the evolution of the dust grain size distribution in addition to the already calculated chemical composition. As shown in this work the size distribution could have a potentially large effect on the SED of galaxies and therefore represents an important area for future work.

This study can also be thought of as a first step toward a more careful comparison between galaxy formation scenarios and observed data particularly in the spectral regions affected by dust emission. The robustness of such a comparison has clearly been shown to be affected by a proper treatment of dust evolution and reprocessing, in a wavelength dependent way. Developing a more rigorous dust treatment which can be applied to galaxy formation models will form the basis for future work.

- The FF-BP ANN has been implemented successfully into the GRASIL code and the network has been thoroughly trained and tested. The next step is to apply it to galaxy formation codes in order to exploit large cosmological simulations, such as the Millennium Simulation (Springel et al. 2005) generating millions of SEDs, which can then be compared to large observational surveys in order to constrain galaxy formation theories.

- GRASIL-3D has been combined with a SPH-hydrodynamic galaxy formation code and the initial results are encouraging, however, there are still several areas which require more work. There are two main improvements needed for the code: a better treatment of the nearest neighbours, and the implementation of an adaptive grid, these will improve the codes accuracy as well as computational performance. Once these improvements have been included, the code then requires rigorous testing, both

by comparisons to other codes, and comparisons to observations. When complete the code should be able to calculate, quickly, a SED from the UV to radio for a galaxy with any geometry. It should therefore be attractive for use with any hydrodynamical code and will be made publicly available.

The SPH galaxy formation code, should also be an ideal test-bed for an improved study of dust evolution in different regions of a galaxy. By adopting the ideas discussed in chapter 2 it would be possible to model the evolution of the dust grain population in different environments within the same galaxy. By a careful comparison to observations this could be used to constrain the various processes contributing to the dust grain population. By including dust evolution within GRASIL-3D it will also improve the accuracy of the model.

Chapter 6:

Bibliography

[1] Almeida, C.; Baugh, C. M.; Lacey, C. G.; Frenk, C. S.; Granato, G. L.; Silva, L.; Bressan, A., 2009, submitted to MNRAS, (arXiv0906.3522A)

[2] Adamson, A. J., Whittet, D. C. B., Chrysostomou, A., Hough, J. H., Aitken, D. K., Wright, G. S., & Roche, P. F. 1999, ApJ, 512, 224

[3] Ballesteros-Paredes, J., Hartmann, L., Vzquez-Semadeni, E., 1999, ApJ, 527, 285

[4] Barber, C. B., Dobkin, D. P., & Huhdanpaa, H. 1996, ACM Trans. Math. Softw., 22, 469

[5] Bauer, A. E., Drory, N., Hill, G. J., Feulner, G. 2005, ApJ, 621, L89

[6] Baugh C. M., Lacey C. G., Frenk C. S., Granato G. L., Silva L., Bressan A., Benson A. J., Cole S., 2005, MNRAS, 356, 1191

[7] Beelen, A., Cox, P., Benford, D.J., Dowell, C.D., Kovacs, A., Bertoldi, F., Omont, A., Carilli, C.L. 2006 ApJ, 642, 694

[8] Bell et al. 2005 ApJ 625 23

[9] Bertoldi, F. et al. 2003, 406, 55

[10] Bianchi, S. 2007, A&A, 471, 765

[11] Bianchi S., 2008, A&A, 490, 461

[12] Bianchi, S., Ferrara, A. & Giovanardi, C. 1996, ApJ 465, 127

[13] Bianchi, S., & Schneider, R. 2007, MNRAS, 378, 973

[14] Bianchi, S., Davies, J.I., Alton, P.B. 2000, A&A, 359, 65

[15] Blaizot, J., Guiderdoni, B., Devriendt, J. E. G., Bouchet, F. R., Hatton, S. J., & Stoehr, F. 2004, MNRAS, 352, 571

[16] Blanco, A., Borghesi, A., Fonti, S., & Orofino, V. 1998, A&A, 330, 505-514

[17] Bower R. G., Benson A. J., Malbon R., Helly J. C., Frenk C. S., Baugh C. M., Cole S., Lacey C. G., 2006, MNRAS, 370, 645

[18] Bradamante F., Matteucci F., D'Ercole A., 1998, A&A, 337, 338

[19] Brinchmann, J., & Ellis, R. S. 2000, ApJ, 536, L77

[20] Bressan, A., Chiosi, C., Fagotto, F. 1994, ApJS, 94, 63

[21] Bressan A., Granato G. L., Silva L., 1998, A&A, 332, 135

[22] Bruzual, G., 2007, ASPC, 374, 303

[23] Bruzual, G., & Charlot, S. 2003, MNRAS, 344, 1000

[24] Byun, Y. I., Freeman, K. C. & Kylafis, N. D. 1994, ApJ 432, 114

[25] Calura, F., Pipino, A., Matteucci, F. 2008, A&A, 479, 669

[26] Cardelli Jason A., Clayton Geoffrey C., & Mathis John S., 1989, ApJ, 345, 245

[27] Chakrabarti S., Fenner Y., Cox T. J., Hernquist L., Whitney B. A., 2008, ApJ, 688, 972

[28] Chakrabarti S., Whitney B. A., 2009, ApJ, 690, 1432

[29] Chary R., Elbaz D., 2001, ApJ, 556, 562

[30] Chiappini C., Matteucci F., Gratton R., 1997, ApJ, 477, 765

[31] Chiar, J. E. & Tielens, A. G. G. M. 2001, ApJ, 550, L207

[32] Chiappini C., Matteucci F., Romano D., 2001, ApJ, 554, 1044

[33] Clayton, D. D., & Nittler, L. R. 2004, ARA&A, 42, 39.

[34] Clayton, Geoffrey C., Green, J., Wolff, Michael J., Zellner, Nicolle E. B., Code, A. D., Davidsen, Arthur F., WUPPE Science Team, HUT Science Team, 1996, ApJ, 460 313

[35] Clements et al., 2008, MNRAS, 387, 247

[36] Cole S., Lacey C.G., Baugh C.M., Frenk C.S., 2000, MNRAS, 319, 168

[37] Collison A. J & Fix J. D., ApJ, 1991, 368, 545-557

[38] Cook, M., Lapi, A., Granato, GL., 2009, MNRAS accepted (arXiv:0903.2390) (C09a)

[39] Cowie, L. L., Songaila, A., Hu, E. M., & Cohen, J. G. 1996, AJ, 112, 839

[40] da Cunha E., Charlot S., Elbaz D., 2008, MNRAS, 388, 1595

[41] Dale, D. A., Helou, G. 2002, ApJ, 576, 159

[42] Dale, D.A., Helou, G., Contursi, A., Silbermann, N.A., Kolhatkar, S. 2001, ApJ, 549, 215

[43] Dale D.A., Gil de Paz A., Gordon K.D., et al. 2007 ApJ, 655, 863

[44] De Lucia, G., Kauffmann, G., & White, S. D. M. 2004, MNRAS, 349, 1101

[45] de Vaucouleurs G., de Vaucouleurs A., Corwin H. G., Jr, Buta R. J., Paturel G., Fouque P., 1991, Third Reference Catalogue of Bright Galaxies, Vols 13. Springer-Verlag, Berlin

[46] Demyk, K., Dartois, E., Wiesemeyer, H., Jones, A. P., & dHendecourt, L. 2000, A&A, 364, 170

[47] Desert, F.-X, Boulanger, F., Puget, J.L. 1990, A&A, 237, 215

[48] Devriendt, J. E. G., Guiderdoni, B., & Sadat, R. 1999, A&A, 350, 381

[49] Di Matteo, T., Springel, V., Hernquist, L. 2005, Nature, 433, 604

[50] Dopita, M.A., 2005, AIPCa, 761, 203D

[51] Dopita M. A. et al., 2005b, ApJ, 619, 755

[52] Dopita, M. A., et al. 2006a, ApJ, 647, 244 (SED2)

[53] Dopita, M. A., et al. 2006b, ApJS, 167, 177 (SED3)

[54] Draine B.T., 2004, in Origin and Evolution of the Elements, ed. A. Mc William & M. Rauch (Cambridge: Cambridge Univ. Press), p. 317

[55] Draine B.T., 2009, in Cosmic Dust, Near and Far, ed. T. Henning, E. Grün & J. Steinacker (San Francisco: Ast. Soc. Pacific), in press (also arXiv 0903.1658)

[56] Draine B.T., Lee., H.M., 1984, ApJ, 285, 89

[57] Draine, B. T., & Malhotra, S. 1993, ApJ, 414, 632

[58] Draine B.T., Li., A., 2001, ApJ, 551, 807

[59] Draine B.T., Li., A., 2007, ApJ, 657, 810

[60] Draine B. T. et al., 2007, ApJ, 663, 866

[61] Dwek, E. 1998, ApJ, 501, 643

[62] Dwek, E. Galliano, F., Jones, A.P. 2007, ApJ, 662, 927

[63] Eales S., Lilly S., Webb T., Dunne L., Gear W., Clements D., Yun M., 2000, AJ, 120, 2244

[64] Efstathiou A., Rowan-Robinson M., 2003, MNRAS, 343, 322

[65] Efstathiou A., Rowan-Robinson M., Siebenmorgan R., 2000, MNRAS, 313, 734

[66] Efstathiou A., & Siebenmorgan R., 2009, A&A, 502, 541

[67] Elmegreen, B., G., 2002, ApJ, 577, 206

[68] Engelbracht, C. W., et al. 2005, ApJ, 628, L29

[69] Ferrara, A., Bianchi, S., Cimatti, A., Giovanardi, C., 1999, ApJS, 123, 437

[70] Ferrarotti, A. S., & Gail, H.-P. 2006, A&A, 447, 553

[71] Flagey, N., Boulanger, F., Verstraete, L., et al. 2006, A&A, 453, 969

[72] Fontanot F.,Monaco P., Silva L., Grazian A., 2007, MNRAS, 382, 903

[73] Fontanot F., Somerville R. S., Silva L., Monaco P., Skibba R., 2009, MNRAS, 392, 553

[74] François, P., Matteucci F., Cayrel R., Spite M., Spite F., Chiappini C., 2004, A&A, 421, 613

[75] Gallego, J., Zamorano, J., Aragon-Salamanca, A., & Rego, M. 1995, ApJ, 455, L1

[76] Galliano, F., Madden, S. C., Jones, A. P., Wilson, C. D., Bernard, J.-P., Le Peintre, F. 2003, A&A, 407, 159

[77] Galliano, F., Madden, S. C., Jones, A. P., Wilson, C. D., Bernard, J.-P. 2005, A&A, 434, 867

[78] Galliano, F., Dwek, E., Chanial, P. 2008, ApJ, 672, 214

[79] Gingold, R. A., & Monaghan, J. J. 1977, MNRAS, 181, 375

[80] Gordon K. D., Misselt K. A., Witt A. N., Clayton G. C., 2001, ApJ, 551, 269

[81] Granato, G. L., & Danese, L. 1994, MNRAS, 268, 235

[82] Granato G. L. et al., 2000, ApJ, 542, 710

[83] Granato G. L., De Zotti G., Silva L., Bressan A., Danese L., 2004, ApJ, 600, 580

[84] Greenberg, J.M. 1968, in Stars and Stellar Systems, Vol. 7, ed. B.M. Middlehurst & L.H. Aller (Chicago: Univ. of Chicago Press), 221

[85] Groves B., Dopita M., Sutherland R., Kewley L., Fischera J., Leitherer C., Brandl B., van Breugal W., 2008, ApJ, 176, 438

[86] Guhathakurta, P., & Draine, B. T. 1989, ApJ, 345, 230

[87] Guiderdoni, B., Hivon, E., Bouchet, F. R., & Maffei, B. 1998, MNRAS, 295, 877

[88] Guzman, R., Gallego, J., Koo, D. C., Phillips, A. C., Lowenthal, J. D., Faber, S. M., Illingworth, G. D., & Vogt, N. P. 1997, ApJ, 489, 559

[89] Hall J. S., 1949, Sci, 109, 166

[90] Hammer, F., Flores, H., Elbaz, D., Zheng, X. Z., Liang, Y. C., Cesarsky, C. 2005, A&A, 430, 115

[91] Hatton, S. 2003, MNRAS, 343, 75

[92] Hauser, M. G., Dwek, E. 2001, ARA&A, 39, 249

[93] Heger, M. L. 1922, Lick Observatory Bulletin, 10, 141

[94] Hiltner W. A., 1949, Sci, 109, 165

[95] Holweger, H. 2001, in Joint SOHO/ACE workshop Solar and Galactic Composition, ed. R.F. Wimmer-Schweingruber, American Institute of Physics Conference proceedings, vol. 598, p.23

[96] Hopkins P. F., Strauss M. A., Hall P. B., Richards G. T., Cooper A S., Schneider D. P. et al. 2004, AJ, 128, 1112

[97] Hopkins F. P., & Hernquist L., 2008 arXiv:0809.3789v1

[98] Hunt, L., Bianchi, S., Maiolino, R. 2005, A&A, 434, 849

[99] Inglesias-Paramo et al. 2007, 2007, ApJ, 670, 279

[100] Itoh H., 1989, PASJ, 41, 853

[101] Jones, A. P., Duley, W. W., & Williams, D. A. 1990, QJRAS, 31, 567

[102] Jones, A. P., Tielens, A. G. G. M., & Hollenbach, D. J. 1996, ApJ, 469, 740

[103] Jonsson P., 2006, MNRAS, 372, 2

[104] Jonsson, P., Groves, B., Cox, T. J., 2009, MNRAS, submitted (ArXiv:0906.2156).

[105] Juneau, S., et al. 2005, ApJ, 619, L135

[106] Kauffmann, G., Colberg, J. M., Diaferio, A., & White, S. D. M. 1999, MNRAS, 303, 188

[107] Kaviraj S. et al., 2007, ApJS, 173, 619

[108] Kennicutt, R.C., 1989, ApJ, 344, 685

[109] Kennicutt, R. C. 1998, ApJ, 498, 541

[110] Kim, S. H., Martin, P. G., & Hendry, P. D. 1994, ApJ, 422, 164

[111] Kimura, H., Mann, I., & Jessberger, E. K. 2003, ApJ, 582, 846

[112] Kodama T., Yamada T., Akiyama M. et al., 2004, MNRAS, 350, 1005

[113] Krügel, E., & Siebenmorgen, R. 1994, A&A, 282, 407

[114] Kylafis N. D., Bahcall J.N., 1987, ApJ 317, 637

[115] Lacey C.G., Baugh C.M., Frenk C.S., Silva L., Granato G.L., Bressan A., 2008, MNRAS, 385, 1155

[116] Lagache G., Dole H., Puget J.-L., 2003, MNRAS, 338, 555

[117] Laor, A., Draine, B. T. 1993, ApJ, 402, 441

[118] Lacey C., Silk J., 1991, ApJ, 381, 14

[119] Lapi, A., et al.2006, ApJ, 650, 42

[120] Li, A. 2005, ApJ, 622, 965

[121] Li A., Draine B. T., 2001, ApJ, 554, 778

[122] Li, A., & Greenberg, J. M. 1997, A&A, 323, 566

[123] Li, A., & Greenberg, J. M. 2002, ApJ, 577, 789

[124] Li, Y., Hopkins, P. F., Hernquist, L., Finkbeiner, D. P., Cox, T. J., Springel, V., Jiang, L., Fan, X., Yoshida, N., 2008. ApJ 678, 41 63.

[125] Lilly, S. J., Le Fevre, O., Hammer, F., & Crampton, D. 1996, ApJ, 460, L1

[126] Lilly, S. J. et al. 1999, ApJ, 518, 641

[127] Lisenfeld U., Ferrara A., 1998, ApJ, 496, 145

[128] Lucy, L. B. 1977, AJ, 82, 1013

[129] Madau P., Ferguson H. C., Dickinson M. E., Giavalisco M., Steidel C. C., Fruchter A., 1996, MNRAS, 283, 1388

[130] Madden S.C., 2005, AIPC, 761, 223M

[131] Madden, S. C., Galliano, F., Jones, A. P., & Sauvage, M. 2006, A&A, 446, 877

[132] Maiolino, R., Schneider, R., Oliva, E., Bianchi S., Ferrara, A., Mannucci, F., Pedani, M., Roca Sogorb, M. 2004 Nature, 431, 553

[133] Maiolino, R., et al. 2006, Mem. Soc. Astron. Italiana, 77, 643

[134] Marigo P., Girardi L., Bressan A., Groenewegen M. A. T., Silva L., Granato G. L., 2008, A&A, 482, 883

[135] Marconi, A., Risaliti, G., Gilli, R., Hunt, L. K., Maiolino, R., & Salvati, M. 2004, MNRAS, 351, 169

[136] Martnez-Serrano, F. J., Serna, A., Domnguez-Tenreiro, R., & Mollá, M. 2008, MNRAS, 388, 39

[137] Martnez-Serrano, F. J., Serna, A., Domnech-Moral, M., Domnguez-Tenreiro, R., 2009 ApJ 705 L133-L137

[138] Mason, R. E., Wright, G. S., Adamson, A., & Pendleton, Y. 207, ApJ, 656, 798

[139] Mathis, J. S. 1996, ApJ, 472, 643

[140] Mathis, J.S. Rumple, W. Nordsieck K.H., 1977, ApJ, 217, 103

[141] Mathis, J. S., & Whiffen, G. 1989, ApJ, 341, 808

[142] Matteucci F., 1994, A&A, 288, 57

[143] Matteucci F., Tornambè A., 1987, A&A, 185, 51

[144] McCulloch, W. S. & Pitts, W. H. (1943), Bulletin of Mathematical Biophysics, 5:115-133.

[145] McKee C. F., 1989, in Allamandola L. J., Tielens A. G. G. M., eds, Interstellar Dust, Proc. IAU Symposium 135. Kluwer, Dordrecht, p. 431

[146] McLure R. J., Dunlop J. S., 2002, MNRAS, 331, 795

[147] Merrill, P. W. 1934, PASP, 46, 206

[148] Meurer, G.R. 2004 in: A.N. Witt et al. (eds.), Astrophysics of Dust, ASP Conf. Ser. 309, 195

[149] Misiriotis A., Popescu, C. C., Tuffs, R. J., & Kylafis, N. D. 2001, A&A, 372, 775

[150] Misiriotis, A.; Xilouris, E. M.; Papamastorakis, J.; Boumis, P.; Goudis, C. D. 2006, A&A, 459,113

[151] Misselt K. A., Gordon K. D., Clayton G. C.,Wolk M. J., 2001, ApJ, 551, 277

[152] Mobasher, B. et al. 2005, ApJ, 635, 832

[153] Möllenhoff, C., Popescu, C. C., & Tuffs, R. J. 2006, A&A, 456, 941

[154] Monaco, P., Fontanot, F., & Taffoni, G. 2007, MNRAS, 375, 1189

[155] Morgan H.L., Edmunds M.G., 2003, MNRAS, 343, 427

[156] Nagashima, M., Lacey, C. G., Okamoto, T., et al. 2005, MNRAS, 363L, 31

[157] Noeske K. G., et al., 2007, ApJL, 660, L43

[158] Nozawa, T., Kozasa, T., Habe, A., Dwek, E., Umeda, H., Tominaga, N., Maeda, K., & Nomoto, K. 2007, ApJ, 666, 955

[159] O'Halloran, B., Satyapal, S., & Dudik, R. P. 2006, ApJ, 641, 795

[160] Obreschkow, D., Rawlings, S., 2009, MNRAS, 394, 1857

[161] Panuzzo, P. et al. 2007, ApJ, 656, 206

[162] Panuzzo P., Granato G.L., Buat V., Inoue A.K., Silva L., Iglesias-Paramo J., Bressan A., 2007, MNRAS, 375, 640

[163] Pascucci, I., Wolf, S., Steinacker, J., Dullemond, C. P., Henning, Th., Niccolini, G., Woitke, P., Lopez, B., 2004, A&A, 417, 793

[164] Pilbratt G. L., 2005, in Wilson A., ed., ESA SP-577, Proc. Dusty and Molecular Universe. ESA, Noordwijk, p. 3

[165] Pipino A., Matteucci F., Borgani S., Biviano A., 2002, NewA, 7, 227

[166] Pipino A., Kawata D., Gibson B.k., Matteucci F., 2005, A&A, 434, 553

[167] Piovan, L., Tantalo, R., Chiosi, C., 2006, MNRAS, 370, 1454

[168] Popescu, C. C., Misiriotis A., Kylafis, N. D., Tuffs, R. J., Fischera, J., 2000, A&A, 362, 138

[169] Popescu, C.C., Tuffs, R.J., 2005 AIPC, 761, 155P

[170] Prunet, S., Pichon, C., Aubert, D., Pogosyan, D., Teyssier, R., & Gottloeber, S. 2008, ApJS, 178, 179

[171] Renzini A., 2006, ARA&A, 44, 141

[172] Rho J., Kozasa T., Reach W. T., Smith J. D., Rudnick L., DeLaney T., Ennis J. A., & Gomez H., 2008, ApJ, 673, 271

[173] Robbins, D., American Mathematical Monthly, 1978, 85, 278

[174] Robson, I., Priddey, R.S., Isaak, K.G., McMahon, R.G. 2004, MNRAS, 351, L29

[175] Rosenblatt, Frank (1958), The Perceptron: A Probabilistic Model for Information Storage and Organization in the Brain, Cornell Aeronautical Laboratory, Psychological Review, v65, No. 6, pp. 386-408.

[176] Rowan-Robinson M., & Crawford J., 1989, MNRAS, 238, 523.

[177] Rybicky, G. B., & Lightman, A. P. 1979, Radiative Processes in Astrophysics (New York: Wiley)

[178] Savage, B. D., & Sembach, K. R. 1996, ARA&A, 34, 279

[179] Scalo J. M., 1986, FCPh, 11, 1

[180] Schurer, A., Calura, F., Silva, L., Pipino, A., Granato GL., Matteucci, F., Maiolino, R., 2009, MNRAS, 394, 2001

[181] Schurer, A., Calura, F., Silva, L., Pipino, A., Granato GL., Matteucci, F., Maiolino, R., 2008, 2008, IAUS, 255, 147S

[182] Serna, A., Domnguez-Tenreiro, R., & Sáiz, A. 2003, ApJ, 597, 878

[183] Shankar, F., Salucci, P., Granato, G. L., de Zotti, G., & Danese, L. 2005, in Growing Black Holes: Accretion in a Cosmological Context, ed. A. Merloni, S. Nayakshin, & R. A. Sunyaev (Berlin: Springer), 470

[184] Siebenmorgen R., & Krügel E., 1992, AA, 259, 614.

[185] Siebenmorgen R., & Krügel E., 2007, A&A, 461, 445

[186] Silva L., Granato GL., Bressan A., Danese L., 1998, ApJ, 509, 103 [S98]

[187] Silva L., 1999, PhD thesis, SISSA, Trieste [S99]

[188] Silva, L., et al. 2005, MNRAS, 357, 1295

[189] Snow, T.P., & Witt, A.N. 1996, ApJ, 468, L65

[190] Sofia, U.J., & Meyer, D.M. 2001, ApJ, 554, L221

[191] Soifer B.T., Neugebauer G. 1991. Astron. J. 101:35461

[192] Somerville, R. S. 2004, in Multiwavelength Mapping of Galaxy Formation and Evolution, ed. R. Bender & A. Renzini (Berlin: Springer), 131

[193] Somerville R. S. & Primack J. R., 1999, MNRAS, 310, 1087

[194] Springel V., et al., 2005, Nature, 435, 629

[195] Steidel, C. C., Pettini, M., & Hamilton, D. 1995, AJ, 110, 2519

[196] Sugerman et al. 2006, Sci, 313, 196

[197] Swinbank et al. 2008, MNRAS in press, (arXiv:0809.0973)

[198] Takagi T., Arimoto N., Hanami H., 2003, MNRAS, 340, 813

[199] Tasker, E. J., Tan, Jonathan, C., 2009, ApJ, 700, 358

[200] Temi P., Brighenti F., Mathews W., 2007, ApJ, 666, 222

[201] Thomas, D., Maraston, C., Bender, R., Mendes de Oliveira, C. 2005, ApJ, 621, 673

[202] Trumpler, R. J. 1930, PASP, 42, 217

[203] Tuffs R. J., Popescu C. C., Volk H. J., Kylafis N. D., Dopita M. A., 2004, A&A, 419, 821

[204] van den Hoek L. B. Groenwegen M. A. T., 1997, A&AS, 123, 305

[205] Vega, O., Silva, L., Panuzzo, P., et al. 2005, MNRAS, 364, 1286 Evolution, ed. J. D. Lowenthal, D. H. Hughes (Singapore:World Scientific Publishing), 103

[206] Vega, O., Clemens, M. S., Bressan, A., Granato, G. L., Silva, L., Panuzzo, P., 2008, A&A, 484, 631

[207] Wada, K., Norman, C. A., 2007, ApJ, 660, 276

[208] Walter, F., et al. 2007, ApJ, 661, 102

[209] Weingartner, J. C., Draine, B. T. 2001a, ApJ, 548, 296

[210] Weingartner, J. C., Draine, B. T. 2001b, ApJS, 134, 263

[211] Wiklind, T., et al. 2008, ApJ, 676, 781

[212] Witt, A. N., Thronson Jr., H. A., & Capuano Jr., J. M. 1992, ApJ 393, 611

[213] White, S.D.M., & Rees, M.J. 1978, MNRAS, 183, 341

[214] White, S. D. M., & Frenk, C. S. 1991, ApJ, 379, 52

[215] Widrow, B., & Hoff, M. E., Jr., 1960, IRE WESCON convention Rec. 96-104

[216] Wu, Y., Charmandaris, V., Hao, L., Brandl, B. R., Bernard-Salas, J., Spoon, H. W. W., & Houck, J. R. 2006, ApJ, 639, 157

[217] Xilouris, E.M., Kylafis, N.D., Papamastorakis, J., Paleologou, E.V., Haerendel, G 1997, A&A, 325, 135

[218] Xilouris, E.M. et al., 1998, A&A, 344, 868

[219] Xilouris, E.M., Kylafis, N.D., Paleologou, E.V., Papamastorakis, J. 1999, A&A, 344, 868

[220] Zhukovska S., Gail H.P., Trieloff M., 2004, A&A in press

[221] Zubko, V., Dwek, E., Arendt R.G., 2004, ApJS, 152, 211

Appendix A

Computation Details for GRASIL-3D

A.1 The SPH grid charging technique

In a SPH code the macroscopic properties of a galaxy are sampled by a number of discrete particles of type t, where t can represent dark matter, gas or stars. To calculate the actual density in any grid cell it is necessary to interpolate over the particles of the desired type using a smoothing kernel. Specifically:

- consider only cold baryon particles, that is only stars (either young, y* or free f*) and cold gas.
- For each cold baryon particle j, assign a smoothing length h_j such that in the sphere $(\vec{r_k}, 2h_j)$ there are 40 cold baryon particles (referred to as its neighbours) where $\vec{r_j}$ is the particles position.
- The mass of the cold baryon particles is then distributed among the neighbouring cells. Specifically, the mass m_j^t of the j-th particle of type t is disributed among the N_j cells whose centre position $\vec{r}_{\vec{k}}$ satisfy:

$$| \vec{r}_{\vec{k}} - \vec{r}_{\vec{j}} | < 2h_j \tag{A.1}$$

with weights given by the SPH algorithm to get $m^t_{j,\vec{k}}$ (mass contributed by the j-th particle to the the t-type mass of the $\vec{k}$-th cell

- The mass of the t-type component at the $\vec{k}$-th grid cell is:

$$M^t_{\vec{k}} = \sum_{j=1}^{N_j} m^t_{j,\vec{k}} \tag{A.2}$$

- Hence the density in each cell is;

$$\rho^t_{\vec{k}} = M^t_{\vec{k}} / V_{\vec{k}} \tag{A.3}$$

- such that

$$M^t = \sum_{k=1}^{N} M^t_{\vec{k}} \tag{A.4}$$

For any component t, where M^t is the total mass in the whole galaxy of the t component, and N is the total number of grid cells.

A.2 Calculating f_{mc}

In the GRASIL-3D model, gas can be in one of two phases: dense molecular gas or diffuse cirrus gas. To calculate the contribution to each of the phases for all the gas particles it is necessary to calculate $f_{mc,i}(\vec{r}_i, t)$ for every particle individually. We know that:

$$f_{mc}(\vec{r}, t) = \rho_{mc}(\vec{r}, t) / \rho_{gas}(\vec{r}, t) \tag{A.5}$$

where: $\rho_{mc}(\vec{r}, t)$ is the density of just the molecular gas component at position $\vec{r}$ and $\rho_{gas}(\vec{r}, t)$ is the density of all the gas at position $\vec{r}$.

This ratio can be calculated from a theoretical probability distribution function (PDF) assuming that cold gas with a density greater than $\rho_{mc,thres}$ is in the form of molecular gas.

The PDF used is based on the work by Elmegreen 2002 and Wada & Norman 2007. Simulations at scales of approximately 1 Kpc indicate that either $f_{pd}(\rho)d\rho$ (i.e., the

number of cells with densities in the range $[\rho, \rho + d\rho]$) or $f_{pd,M}(\rho)d\rho$ (i.e., the mass fraction living within cells with densities in the range $[\rho, \rho + d\rho]$) can be fit by log-normal functions. In both cases this log-normal is characterized by two parameters; the first in both cases is the dispersion σ, the second is a density parameter, in the former case ρ_0, and in the other $\rho_0 e^{\sigma^2}$. The volume-averaged density $< \rho >_V$ and mass-averaged density $< \rho >_M$ are given respectively, by:

$$< \rho >_V = \rho_0 e^{\sigma^2/2} \tag{A.6}$$

and

$$< \rho >_M = \rho_0 e^{2\sigma^2} \tag{A.7}$$

Hence by using the PDF and setting a value for $\rho_{mc,thres}$, σ and ρ_0 we can calculate $f_{mc}(\vec{r}, t)$, where:

$$f_{mc}(\vec{r}, \rho_{mc,thres}, \rho_0, \sigma) = \frac{I(\rho_{mc,thres}, \rho_0, \sigma)}{I(0, \rho_0, \sigma)} \tag{A.8}$$

where:

$$I(A, \rho_0, \sigma)) = \int_{lnA}^{\inf} \rho f_{pd}(ln\rho; ln\rho_0; \sigma) dln\rho \tag{A.9}$$

Which can be rewritten as (Wada & Norman 2007, eq. 18 and 19):

$$f_{mc}(\vec{r}, \rho_{mc,thres}, \rho_0, \sigma) = 0.5(1 - Erf[z(\rho_{mc,thres}/\rho_0; \sigma)]) \tag{A.10}$$

where:

$$z(\rho_{mc,thres}/\rho_0; \sigma) = ln((\rho_{mc,thres}/\rho_0) - \sigma^2)/(\sigma\sqrt{(2)}) \tag{A.11}$$

and Erf is the error function.

It is only necessary to set one of the PDF parameters, either σ or ρ_0. The other can be calculated from *eq. A.6* and the SPH gas density at the position of the i-th particle. Specifically, we make the identification:

$$< \rho >_V = \rho_{gas}^{SPH}(\vec{r}_i) \tag{A.12}$$

A.3 Calculating $P(T)$ the temperature distribution for small grains

This section is taken from S99: section A.1.

We summarize the method adopted to compute the temperature distribution function $P(T)$ for small fluctuating grains, based on the papers by Guhathakurta & Draine (1989) and Siebenmorgen et al. (1992).

The time variable energy content of small grains is represented through a steady state temperature distribution function $P(T)$, with $\int P(T)dT = 1$, so that $P(T)dT$ is the probability that a grain is in the temperature interval T, $T + dT$. For large grains $P(T)$ approaches $\delta(T_{eq})$, the delta–function at the equilibrium temperature, while for small grains it can be very large.

$P(T)$ is computed as follows: when a grain absorbs or emits photons a transition from an intial state i to a finale f of the grain enthalpy $U(T)$ occurs. Let P_i be the probability to find a grain in the ith enthalpy (or temperature) bin and A_{fi} the transition probability per unit time from state i to $f \neq i$; the condition of statistical equilibrium yields:

$$\frac{dP_f}{dt} = \sum_{i \neq f} A_{fi} P_i - P_f \sum_{g \neq f} A_{gf} = \sum_i A_{fi} P_i = 0 \tag{A.13}$$

with the definition $A_{ff} \equiv -\sum_{g \neq f} A_{gf}$. The equilibrium distribution is thus obtained by solving the following linear system:

$$\begin{cases} \sum_i A_{fi} P_i = 0 \\ \sum_i P_i = 1 \end{cases} \tag{A.14}$$

for each f. The normalization condition of the probability is needed to univocally solve the system.

The matrix elements A_{fi} are computed as follows:

- $i < f$, absorption:

$$A_{fi} = \frac{4\pi J_{\nu_{fi}}}{\Delta U_{fi}} \pi a^2 Q_{abs}(\nu_{fi}, a) \frac{\Delta U_f}{h}$$

- $i > f$, emission:

$$A_{fi} = \frac{4\pi B_{\nu_{fi}}(T_i)}{\Delta U_{fi}} \pi a^2 Q_{abs}(\nu_{fi}, a) \frac{\Delta U_i}{h}$$

in this case when $f = i - 1$ the following term must be added to the above expression for A_{fi}:

$$-\left(\frac{dU}{dt}\right)_i \frac{1}{U_i - U_f}$$

that keeps into account the transitions implying emission (and absorption) of photons of frequency lower than the minimum one, ν_{fi}, allowed by the discretization of the energy states,

where:

$$\Delta U_{fi} = |U_f - U_i|$$
$$\nu_{fi} = \frac{\Delta U_{fi}}{h}$$
$$J_{\nu_{fi}}[erg/(cm^2\, s\, hz\, st)]$$
is the radiation field at frequency ν_{fi}
ΔU_k is the width of the kth energy state

and the net cooling rate is given by the following equation:

$$\left(\frac{dU}{dt}\right)_i = \left(-\int_{\nu_{min}}^{\frac{U_i - U_{i-1}}{h}} B_\nu(T_i) Q_{abs}(\nu, a) d\nu + \int_{\nu_{min}}^{\frac{U_{i+1} - U_i}{h}} J_\nu Q_{abs}(\nu, a) d\nu \right) 4\pi^2 a^2 \quad \text{(A.15)}$$

where the two terms on the rhs, respectively for cooling and heating, keep into account those transitions between neighbouring states implying photon energies lower than the minimum ones provided by the array of energy states. A net cooling rate is considered since the two terms are similar.

In case of emission, Guhathakurta & Draine (1989) introduced a numerical simplification to speed up the computation, setting $A_{fi} = 0$ for $i > f+1$, and $A_{f,f+1} = -(\frac{dU}{dt})_i \frac{1}{U_i - U_f}$ for $i = f + 1$, i.e. they assume emission occurs only between neghbouring states, but with a probability that is the sum over all possible downward transitions. Indeed in this case the upper limit of integration for the cooling term in $(dU/dt)_i$ (Eq. A.15) is fixed to a high value (in the UV). This considerably speeds the computation, since the A_{fi} matrix

elements above the main diagonal are all zero except those just above it. Siebenmorgen et al. (1992) find that with this approximation the sub–mm emission from small grains is underestimated. Anyway the sub–mm emission in a galaxy is dominated by normal grains, that reach much lower temperatures. Therefore we generally performed the computations according to this faster scheme.

A.4 Calculating $r(i,k)$ for nearest neighbours

In order to calculate the radiation field in the i-th cell, equation 4.17 an $r(i,k)$ term is required both in the denominator and also in the numerator through equation 4.11, (dl is equivalent to the $r(i,k)$ term). For most cases this can be approximated as the square of the centre of the i-th cell to the centre of the k-th cell. However for the nearest neighbour cells this relation breaks down.

This is particularly clear in the $i = k$ term. A natural choice for solution of r(i,k) in this cell could be the Robbins constant, 0.6617.. (robbins 1978), the average distance between two points selected at random within a cube with sides of length 1. This however has been found to be incorrect, particularly when the optical depth in the i-th cell is high. In this case a much smaller value for r(i,k) is required. This is because the term $exp\ (-\tau_{eff}, \lambda(i,k))$ in the numerator dominates the expression when $\tau_{eff,\lambda(i,i)}$ becomes large and as a result the radiation at each position in a cell is dominated by sources much closer to itself than the Robbins constant. Since the value of r(i,k) which will give a correct value for the radiation field will vary depending on the optical depth through the cell there is no single unique value for $r(i,i)$.

Instead an algorithm has been written in order to calculate an appropriate value for $r(i,i)$ separately for every cell. This will be the $r(i,i)$ which will give a correct result for $J_{\lambda,i}$ when inserted into the $i = k$ term of equation 4.17, such that the energy absorbed by the cell will be equal to the energy emitted by the cell.

For the i=k component this corresponds to the situation where the energy emitted by the cirrus dust grains within the cell due just to the sources internal to the cell is equal to the energy absorbed by the cell just from internal sources.

The energy absorbed by cell i due to dust within the cell itself, j_{abs} can be simply evaluated following:

$$j_{abs} = (1 - exp(-\tau_e ff)) \times (j^{mc}_{\lambda,i} + j^{*}_{\lambda,i}) \tag{A.16}$$

where $\tau_{eff} = \alpha \times \sigma$ and $\alpha = 0.640395$ is the average distance from the centre of a unit cube to a given face.

Hence, due to the conservation of energy, it is known that the dust from the cell i must be emitting this much energy only due to internal starlight from the cell itself. By treating the cell in isolation it is possible to solve equation 4.17 where $r(i, j)$ is treated as an unknown, in order to calculate the radiation field due to the i=k-th term required to emit this amount of energy.

Since such a method requires the energy balance equation (equation 4.14) to be solved a number of times until a correct value for $r(i, i)$ is found, using a bi-section algorithm, it will be computationally expensive. This can be seen from figure A.3, in §A.5. Hence, if we want to improve the performance of the code, it is vital to reduce this time. It is clear both from the outputs of the code and intuition that the value of $r(i, i)$ will be different for every cell with a distances depending on the optical depth of the i-th grid cell. As expected a graph of $r(i, i)$ vs τ_i does indeed show a clear trend, see figure A.1. By applying the series of power laws shown in this figure it completely removes the need to run nearest neighbour function and drastically reduces the overall running time of the code. The application of the analytical fit, as opposed to the full treatment produces negligible effects on the SED, although a more rigorous test with higher density environments is required, to check this analytical fit always holds.

Using similar arguments it is clear that the values of $r(i, k)$ to the 26 nearest neighbour cells have no unique solution either. For now these cells are treated by following the equation:

$$r(i, k) = NN \times r(i_{centre}, k_{centre}) \times r(i, i) \tag{A.17}$$

Where NN is a parameter which is fixed to give an overall cirrus energy balance

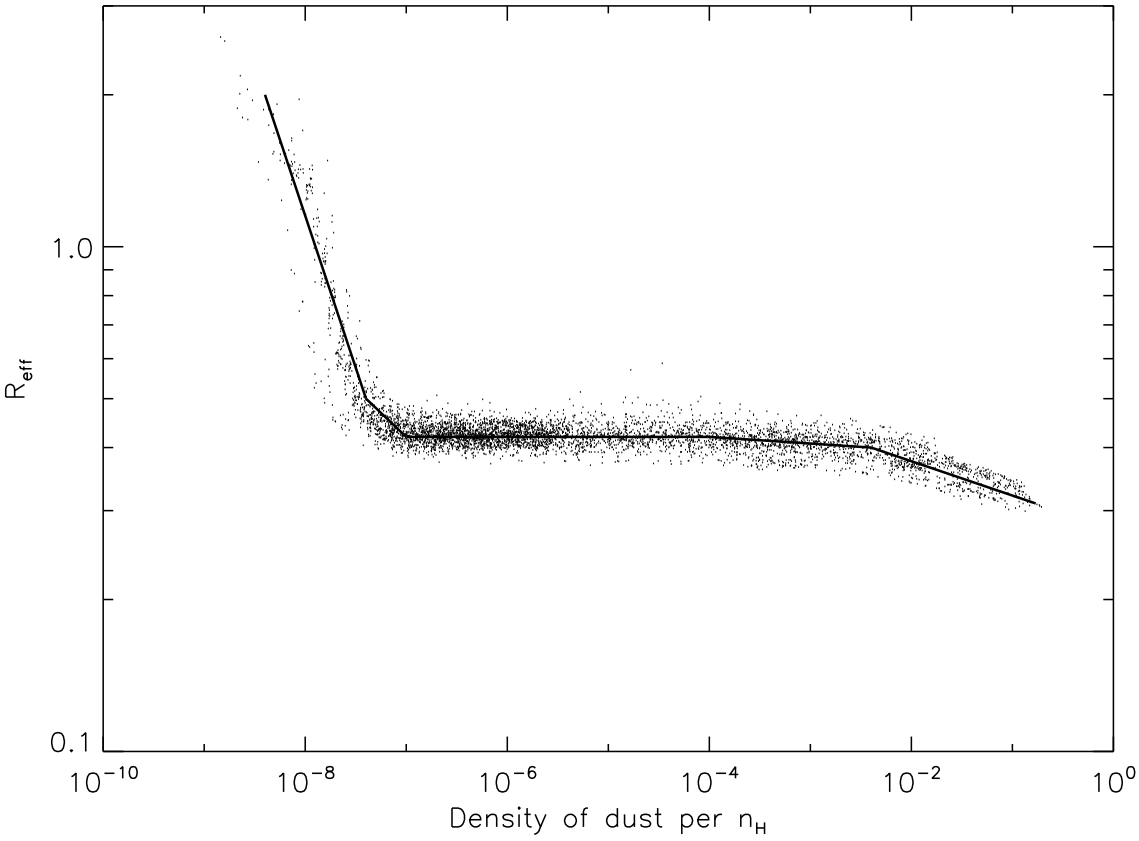

Figure A.1: Graph showing how the calculated effective radius, $r(i,i)$, varies with the density of the dust in the cell, and hence with the optical depth through the cell.

so that the total energy emitted by the cirrus dust in all the galaxy will be equal to the total starlight absorbed by the cirrus dust. The dependence on $r(i,i)$ ensures that the distance $r(i,k)$ will be related to the optical depth of the i=k-th cell, as expected. It is hoped that in future this treatment of the other 26 nearest neighbour cells will be improved.

Once $r(i,k)$ is known for the nearest neighbour cells case we can calculate the contribution from all the other cells to the radiation field by setting $r(i,k)$ to the distance between the centre of cell i to the centre of cell k. The radiation field can then be solved using equation 4.17.

A.5 Details of optimisations and computing time

The code has been written in a modular form, so that any section of can be easily changed, or alternative treatments used. The organisation of the code is shown in figure A.2. It has been parralised with open-mpi and has been successfully run on a cluster with almost 100% efficiency of parralization. The code can be compiled on both windows and linux machines.

The first task the code performs is to initialise all the arrays, calculate dust properties and to charge all the grid cells as discussed in § 4.3.1. This part of the code is in serial with every processor performing every task. Next the code calculates, for all the grid cells, low resolution SEDs for the free stars and molecular clouds, for use in equation 4.17.

The main loop then starts with all the cells with a non-zero gas or stellar component divided up between the CPUs. For each cell if there are free stars the code models them as a SSP and calculates a high resolution SED for them. If there are young stars the code models them as a molecular cloud and calculates a high resolution SED for this component. If there is gas the code calculates the radiation field from all non-zero grid cells using the low resolution SEDs for the young stars (in molecular clouds) and free stars calculated previously. Once this is calculated the cirrus emission is calculated. The thermal balance is calculated using low resolution arrays for the radiation field and a low resolution wavelength array for the emission. Once this balance has been calculated the emission is then calculated for a high resolution emission spectrum. Depending on the desired output

the SEDs can be summed together and stored in a number of different ways.

The code is set up in this way to minimise the memory storage and computation time.

The computing time required to run the different parts of the code is shown in figure A.3.

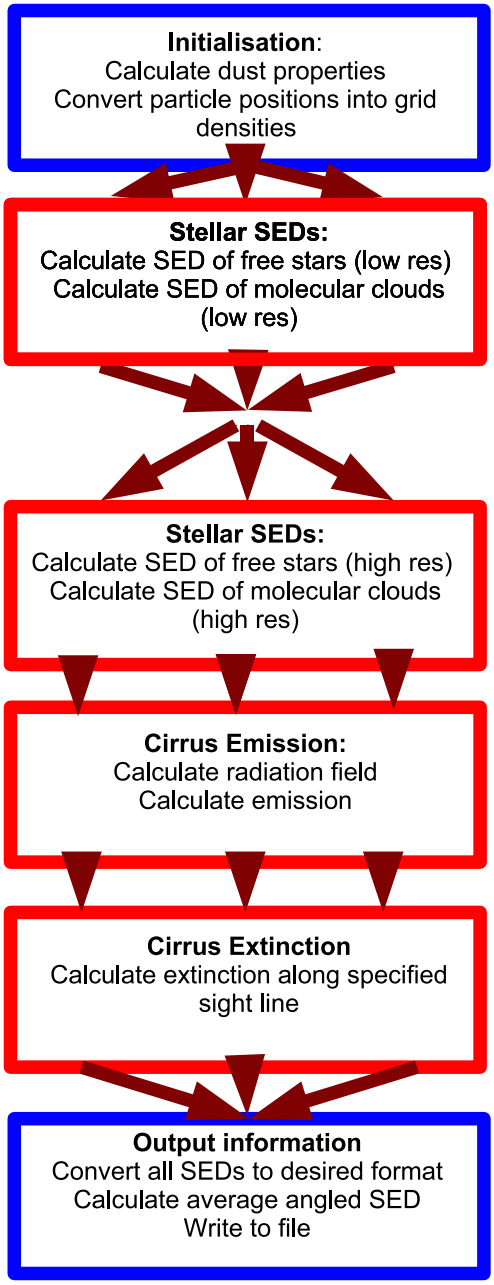

Figure A.2: A Schematic diagram showing how the code for GRASIL-3D is organised. Tasks bordered by red are parallelised, tasks bordered by blue are serial code.

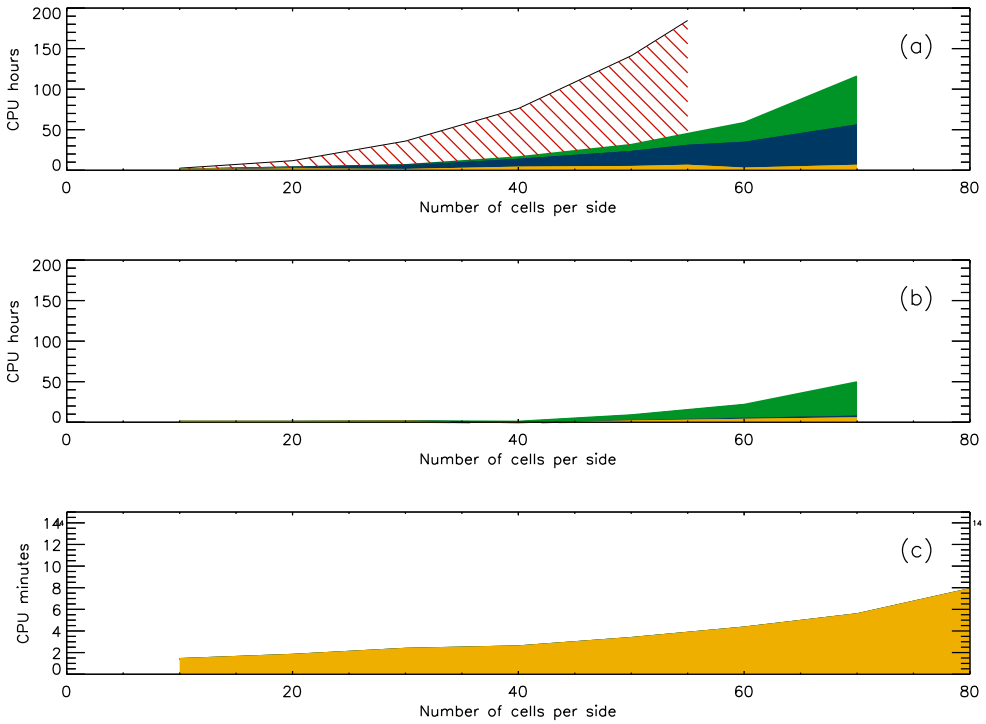

Figure A.3: A break down of the approximate times taken for each stage for, a) the full code, with fluctuating grains: b) no fluctuating grains: c) no emission. Colour scheme: Red - Time taken for nearest neighbours calculation. Green - Time taken for radiation field calculation. Blue - Time taken to calulate the emission. Yellow - Time taken by the rest of the code. All calculations have been performed on 2 GHz CPUs.

Acknowledgements

I am grateful to my supervisors and all my collaborators, who have made this work possible, in particular G.L. Granato, L. Silva, F. Calura, F. Matteucci, A. Pipino, R Dominguez-Tenreiro, A. Serna, R. Maiolino, as well as A. Bressan and A Boselli, who have all helped at various stages throughout my PhD. I would also like to express my thanks to MAGPOP, a Marie Curie Research and Training network network (contract number MRTN-CT-2004-503929.), which has allowed me to attend many international conferences and meet many interesting people. I also thank my many friends in Trieste and in SISSA, who have been a great help, in particular Michael Cook, for many useful discussions and Lorenzo Paulatto, whose technical computing knowledge has proved invaluable. Finally I would like to thank my parents for their continuing support which has allowed me to get to where I am today.